BODLEIAN LIBRARY OXFORD
DEPOSITED
THESIS
11·1·72

ASPECTS OF STEADY AND PULSATILE FLOW IN BRANCHED TUBES WITH PARTICULAR REFERENCE TO BLOOD FLOW.

BY

ROBERT BRECH

MAGDALEN COLLEGE

A thesis submitted for the degree of Doctor of Philosophy in the University of Oxford.

August, 1971.

ABSTRACT

The nature of the flow in branching blood vessels is of importance to physiologists, mainly on account of the formation of atheromatic deposits which occur frequently at sites of branching. The reasons for the occurrence of these deposits are not yet understood but it is generally agreed that the effects of fluid dynamics may well be important. There is, however, a lack of knowledge as to the detailed nature of the flow at and around branches and this study has been undertaken in order to provide such knowledge.

The flow in symmetrical branches, typical of the blood vessels in man, has been studied using rigid-walled models perfused with steady and pulsatile water flows. The streamline patterns have been studied using dye and hydrogen bubble tracers and the effects of pressure differences and obstructions have also been investigated. Detailed measurements of axial velocity distribution and wall shear stress have been made with heated element probes developed for these applications. The design of these probes and the development of a digital output system are described.

The following observations and conclusions have been made:

1. Contra-rotating, helical vortices are set up on the outside of each limb, their strength varying with the mean square of the input velocity. These vortices spread across the whole of the tube to give an approximately symmetrical velocity distribution within about six diameters downstream, this distance being independent of input velocity and profile.
2. There is markedly high shear stress on the inside wall of each limb and low shear stress on the outside wall. This differential is only maintained significantly, however, for 4 or 5 diameters downstream.
3. The mass flow distribution between the two limbs of a branch is very sensitive to small pressure differences between the limbs. This is not a flow switching (Coanda) effect, but a consequence of the relatively small pressure drop in each limb. Obstructions near the apex of the branch do not in general affect the mass flow distribution.

4. The stability of the downstream flow development depends on the input velocity, the stability increasing with decrease of velocity.
5. The interior geometry of the branch has only minimal effect on any downstream measurements.
6. The downstream flow patterns and velocity distributions in pulsatile flow show that there is little difference between the downstream effects in pulsatile and steady flow and that most pulsatile flows can be considered quasi-steady. Pulsatile flow tends to stabilise the downstream flow development.
7. Preliminary observations in a confluence show that there is no high shear stress at any position. In steady flow, vortices are shed from the apex causing pulse-shaped velocity and shear stress variations downstream. The frequency of the vortex shedding increases linearly with velocity.

ACKNOWLEDGEMENTS

I am indebted to my supervisor, Dr.B.J. Bellhouse, for his most valuable advice and encouragement and I wish to take this opportunity of expressing my thanks to him.

Valuable technical assistance has been received from Mr. F.H. Bellhouse and also from Messrs.C.M. Curl (electronics), J.C. Reaich (probes) and J. Carson and T.I. Macmillan (apparatus). Their contribution is gratefully acknowledged. My thanks are due also to my wife for her help in the presentation of the thesis and to Mrs. M. Miles for typing the manuscript.

I am grateful to Vickers Ltd. for the award of a Postgraduate Research Scholarship and to the Medical Research Council for their support of the work.

CONTENTS

		Page
Abstract		i
Acknowledgements		iii
Contents		iv
List of Figures		vii
Branch notation		ix
Symbols used		x
1.	Introduction	
	1.1 Review and objectives	1
	1.2 Experimental apparatus	6
2.	The shape of branching blood vessels	
	2.1 Theory	9
	2.2 Experimental observations	13
	2.3 The shape of model branches	15
3.	The effect of small pressure differences in branches	
	3.1 Introduction	16
	3.2 Calculation of the downstream pressure drop	17
	3.3 Experimental investigation	19
	3.4 Analysis of experimental data	21
	3.5 The effect of obstructions near the branch carina	24
4.	The streamline pattern within the branch	
	4.1 The formation of secondary flows	27
	4.2 Experimental studies	30
	4.3 Pulsatile flow	38
	4.4 The effect on the streamline pattern of total occlusion of one limb	39
5.	The design of a directionally-sensitive thin-film velocity probe	
	5.1 Introduction	43
	5.2 The directionally-sensitive probe	46

		Page
5.3	Experimental tests	48
5.4	Calibration and use of probe	49
5.5	Analysis of probe behaviour	55
5.6	Summary	59
6.	The velocity distribution downstream of branches in steady flow	
6.1	Introduction and apparatus	60
6.2	Measurement, computation and presentation of results	61
6.3	Errors	66
6.4	Description of velocity plots	68
6.5	Numerical analysis of velocity plots	
6.5.1	Centreline velocity	74
6.5.2	Distribution moments	77
6.5.3	Energy dissipation	80
6.6	Summary	83
7.	Design of a methodology for sampling and analysing pulsatile flow velocities	
7.1	The data logging system	86
7.2	The computer program	91
8.	The velocity distribution downstream of branches in pulsatile flow	
8.1	Experimental technique	95
8.2	Errors	98
8.3	The pulsatile flow velocity plots	99
8.4	Summary	104
9.	Distribution of wall shear stress in branches	
9.1	Introduction	105
9.2	Experimental observations	106
9.3	An estimate of shear stress in arterial branches	112
9.4	Shear stress and vortex shedding in a confluence	114

page

10. Discussion

10.1 The formation of early atheromatic deposits 119

10.2 Suggestions for further work 121

References 122

Appendices 1 and 1a. The pulsatile flow processing computer program. 126

Figures.

LIST OF FIGURES

Graphs and figures are presented at the end of the text except where marked otherwise. The letter T below indicates that the figure concerned is shown within the text.

1.1 Diagram of experimental layout.

2.1 T. Virtual work diagram for branch.
2.2 Graph: Relative radii of branch daughter tubes.
2.3 Graph: Angle of branching v. tube radius.
2.4 Drawing of branch 1.
2.5 Drawing of branch 2.

3.1 Graph: h_L/Q_i v. Q_i.
3.2 Photo of switched flow in branch.
3.3 Photo of equiflow in branch.
3.4 Graph: 1/Qf(Q) v. Q.
3.5 T. Position of obstruction near branch carina.

4.1 T. Parabolic input velocity.
4.2 T. Net forces on curving fluid.
4.3 T. Secondary flows in curving fluid.
4.4 T. Input profile to each limb.
4.5 T. Cross-sectional shape change through branch.
4.6 T. Fluid movement in branch.
4.7 Graph: Secondary velocity v. mean square velocity.
4.8 T. Diagram of streamlines in branch.
4.9 T. Photo of streamlines in branch.
4.10 T. Photo of streamlines in branch.
4.11 T. Straight branch with no curvature.
4.12 T. Curved branch with no shape change.
4.13 T. Streamlines in branch with occluded limb.
4.14 T. Streamlines in straight branch with occluded limb.

5.1 T. Anemometer feedback bridge.
5.2 T. The directionally-sensitive velocity probe.
5.3 Graph: Probe calibration v. angle.
5.4 Graph: Calibration velocity v. mean velocity.
5.5 Graph: Probe calibration v. velocity.
5.6 Probe calibration in pulsatile flow.
5.7 T. Probe analysis notation.
5.8 Graph: Probe calibration v. velocity in probe tube.
5.9 T. Position of measured velocity.

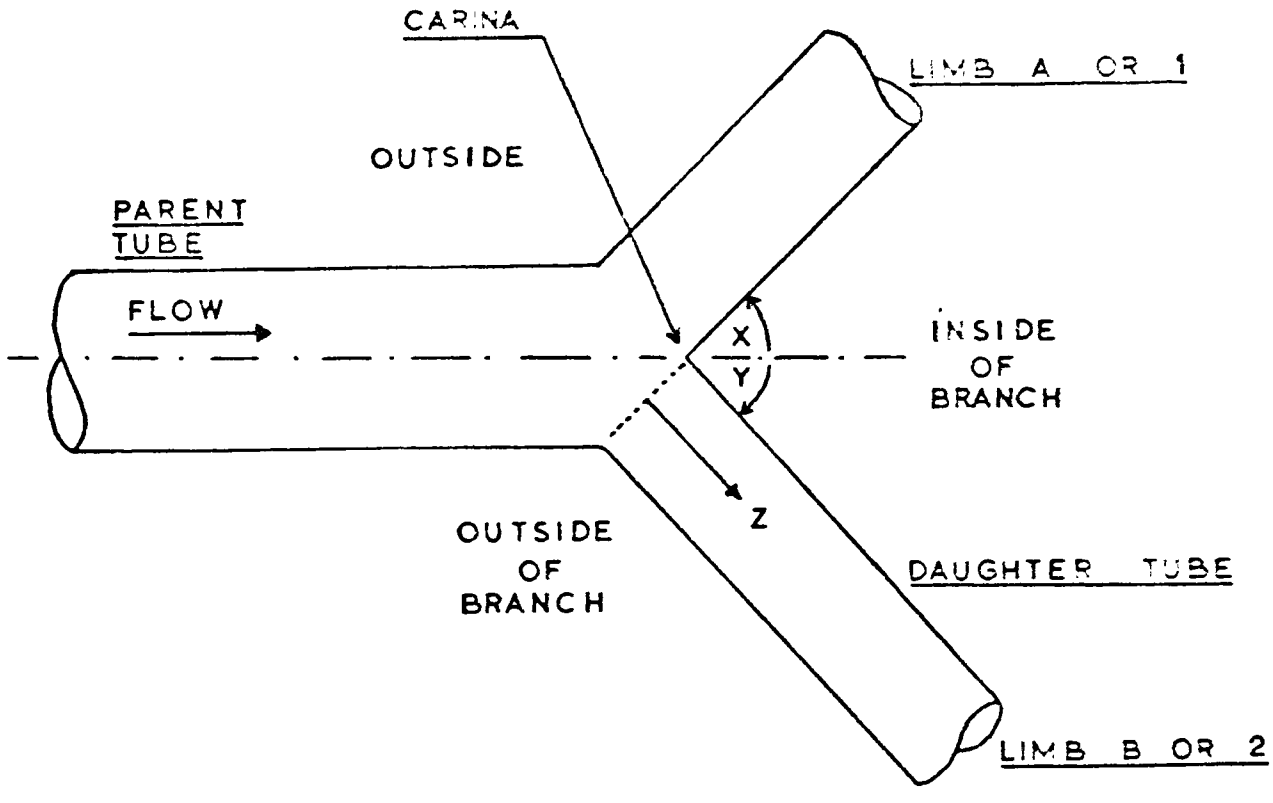
6.1 Probe traversing mechanism.
6.2 Typical velocity profiles against position.
6.3 Velocity plots 1L3, 1L7, 1L11 and 1L15.
6.4 Velocity plots 1L23, 1L31 and 1L47.
6.5 Velocity plots 2L7, 2L11 and 2L15.
6.6 Velocity plots 1H3, 1H7, 1H11 and 1H15.
6.7 Velocity plots 1H23, 1H31, 1H47 and 1H63.
6.8 Velocity plots 2H7, 2H11 and 2H15.
6.9 Graph: Centreline velocity v. distance downstream.

7.1 Block diagram of pulsatile flow methodology.
7.2 Pulsatile flow methodology diagrammatic output.
7.3 Photo of data logging system.

8.1 Inlet velocity pulse.
8.2. Velocity plot 1L3P.
8.3 Velocity plot 1L7P.
8.4. Velocity plot 1L11P.
8.5 Velocity plot 1L15P.
8.6 Velocity plot 1H3P.
8.7 Velocity plot 1H7P.
8.8 Velocity plot 1H11P.
8.9 Velocity plot 1H15P.
8.10 T. Position of backflow.

9.1 Graph: Probe calibration v. velocity.
9.2 Graph: Shear stress v. distance downstream.
9.3 Graph: Shear stress distribution around tube.
9.4 T. Velocity boundary layer.
9.5 Graph: Time-varying shear stress.
9.6 Graph: Shear stress distribution around tube in pulsatile flow.
9.7 Graph: Vortex shedding frequency v. velocity.
9.8 Variation of shear stress with time in a confluence.
9.9 Variation of velocity with time in a confluence.
9.10 T. Effect on velocity of a vortex shed in a confluence.

BRANCH NOTATION



The terminology used in referring to a branch can be described with reference to the figure above. The inlet tube is known as the parent tube and each of the diverging tubes or limbs is known as a daughter tube. The apex of the branch, where the two daughter tubes meet, is known as the carina. The area between the two daughter tubes is known as the inside of the branch, the remainder being the outside.

The two limbs of the experimental branches are referred to as A and B, limb A branching to the left as seen by the incoming flow. When subscripts a and b are added to branch variables, they indicate values in limbs A and B respectively. Subscript i refers to an unspecified daughter tube. i.e. either limb A or limb B. Subscript 0 refers to the parent tube. Subscripts 1 and 2, where they refer to branches, refer to the two limbs of any branch and not necessarily to the experimental branches.

SYMBOLS USED

A	Area
A_i	Area of the ith. annulus.
B	Constant
C	Constant
E	Heat in
F	Calibration constant
G	Calibration constant
H	Head of water
I_0, I_2	Modified Bessel functions of the first kind
K	Dean's K ($=2aRe^2/R$)
K, K_i	Constant
L	Development length
MO, Ml, M2, M3 }	Distribution moments
P	Pressure
Q	Volume flowrate
$\overline{Q}$	Mean Q
R	Radius of curvature
R	Generalised resistance
R_0	'Cold' resistance of thin film probe
R_s	Operating resistance of this film probe
ΔR	$R_s - R_0$
Re	Reynolds' number ($= ud/\nu$)
T	Temperature
V	Volume
V_b	Anemometer bridge-top voltage
V_0	The value of V_b at zero flow
V(j,k,ℓ)	The kth. sample of steady velocity in position j of traverse ℓ .
V(i,j,k)	(k>8) Sample of velocity at time i in pulse (k-8) at position j of any traverse
V(i,j,ℓ)	(ℓ≤8) Mean sampled velocity at time i in position j of traverse ℓ.
W	Work out
Y	Ratio of rate of energy dissipation to that in the same Poiseuille flow

a	Radius
b	Calibration constant
c	Calibration constant
d	Diameter
e	Energy transfer
f	Frequency
g	Gravitational constant
h	Head of water
h_L	Head loss
i	Current
k	Rate of heat transfer
k	Constant
ℓ	Length
m	Mass
n	Constant
p	Ratio of diameter of daughter tube 1 to parent tube
q	Ratio of diameter of daughter tube 2 to parent tube
r	Radius; radial position
r_0	Radius of branch parent tube
r_1, r_2	Radius of branch limbs
$\bar{r}$	Position of centre of mass flow
s	p/q
t	Time
u	Velocity
$\bar{u}$	Mean velocity
u_r	Radial velocity
v	Transverse velocity
w	Axial velocity
x	Angle between daughter tube 1 and parent tube
y	Angle between daughter tube 2 and parent tube
z	Distance downstream
α	Ratio of flow in daughter tube to flow in parent
β	Temperature coefficient of resistance
θ	Angle

μ	Viscosity
ν	Kinematic viscosity
ρ	Density
τ	Shear stress
$\phi(z)$	A function of z
Φ	Rate of dissipation of energy per unit volume

Subscripts (where not defined above)

a	Limb A of the experimental branches.
b	Limb B of the experimental branches.
b	Blood.
c	Centreline.
e	Within directional thin-film probe tube.
i	Either limb of a branch
i	The ith, value of the variable.
w	Water.

Definitions of some terms

Branch geometry	:	The inside variation of the branch vessel walls.
Branch shape	:	Determined by the diameters of the three tubes and the angles between them.
Equiflow	:	That state when the flow down each daughter tube is the same.
Occlusion	:	The closing down of a vessel.
Stenosis	:	The narrowing of a vessel.

1. INTRODUCTION

1.1 Review and objectives

The flow of blood in branching blood vessels has been of interest to physiologists on account of two important factors; the damage to blood cells that may result during their passage through a branch and the deposition of atherosclerotic plaques on the branch walls. Atherosclerosis is defined (Stedman, 1960) as a hardening and narrowing of the inside wall of a blood vessel caused by the deposition or degenerative accumulation of fatty material known as atheroma. This reduces the flow of blood in the vessels affected and the gradual occlusion of these vessels can lead to very detrimental effects in the organs and tissues supplied.

Most workers have agreed that the effects of fluid dynamics might well have an important bearing on the formation of atheromatic plaques and this is given support by evidence that deposits occur with great frequency at sites of curvature and branching. (Mitchell and Schwartz, 1965; Texon, 1963; Caro et al., 1971). The underlying fluid dynamic processes which may help deposits to form are not as yet understood, however. It has been suggested that the formation of plaques at branches is caused by turbulence (Mitchell and Schwartz, 1965), boundary layer separation (Fox and Hugh, 1966), low pressure sucking on the outside of the branch (Texon, 1963), low pressure sucking on the inside of the branch (Texon, 1960) and

high shear stress (French, 1970) and also that the positions of deposits occur in areas of low shear stress (Caro et al.,1971) and high shear stress (French, 1970). What is evident is that there is little scientific knowledge of what fluid dynamic effects actually occur within a branch and it is to provide some knowledge within this field that this study has been undertaken. Dr.M.G.Taylor, summing up the proceedings of the first international symposium on pulsatile blood flow in April, 1963, stated: "One thing that we will have to look at is the nature of flow at branches, what happens in the branches and the details of the fluid motion itself....This seems to be a very important topic".

The objective therefore was to make a detailed study of the flow in branches choosing the values of such parameters as branch shape and Reynolds' and Strouhal numbers so as to make the study applicable to blood flows. It was required to record the streamline patterns in the branches using flow visualisation techniques and to investigate the effects of pressure differences and obstructions on the flow. Detailed measurements of velocity and shear stress distributions downstream of the branches would also be necessary. Since blood flow is pulsatile in the arteries, becoming steadier in the peripheral circulation, measurements of both steady and pulsatile flows were required. Knowledge of the fluid dynamic effects within branches, particularly the distribution of shear stress, could lead to a better understanding of blood flow in branches and the selective deposition of atheroma. It is also to be hoped that the results will be of value not only in the field of blood flow but in any situation where fluid runs through similar branching systems.

Very little detailed study of the flow in branches has yet been made. Stehbens (1959) has investigated the critical Reynolds' number for transition from laminar to turbulent flow in varying branch shapes and Barnett and Cochrane (1956) have made a study of the spreading effects from large vessels to small tributaries. Knox (1962) has investigated the pressure downstream of side branches and has made some suggestions about developed flow recovery lengths. Schroter and Sudlow (1969) and Schreck and Mockros (1970) have both made studies of the flow patterns in air in branching networks together with some velocity profiles in order to gain an insight into the workings of

the lung. Most of the other investigations that have been made, however, have been undertaken by physiologists seeking clarification or confirmation of one or two detailed points. There is therefore much scope for a study of branched tube flow from a fluid dynamicist's point of view.

A detailed analysis of the flow in branches has been made using rigid-walled models perfused with water flows. Since the motivation for the work was biomedical, the shape of the branches was determined from physiological principles and observations and the inlet flow was always laminar as is usually the case with blood flow. (Schultz et al., 1969). When comparing the results of experiments in water flows with blood flows, however, two points must be borne in mind. Firstly, blood is a non-Newtonian fluid consisting of particles suspended in fluid plasma and care should therefore be taken when extrapolating the results of experiments in water. The radii of arterial blood vessels are very much greater than the radii of blood cells, however, and investigators have found (Whitmore, 1968) that flow resistance and secondary velocities are virtually unchanged by non-Newtonian flow properties. Secondly, all the experiments described herein were conducted in rigid tubes whereas blood vessels are slightly elastic. The radius of arterial blood vessels tends to vary at the most by 5% (McDonald, 1960), however, and Sandler and Bourne (1963) report that "The transient dilation (of the arterial wall) following systole is relatively small and its effect

on the stability of flow is negligible when compared with effects of the average peak velocity of flow." It was felt therefore that both these points could be neglected in the present study.

One of the difficulties of a study of flow in branches is the extremely complicated nature of the flow which makes detailed theoretical or mathematical analysis almost impossible, at least by present-day methods. Solution of the Navier-Stokes equations for the much simpler case of symmetrical flows in curved pipes of non-varying diameter has only been achieved under certain stringent conditions by Dean (1927) and more recently by McConalogue and Srivastava (1968) whereas the flow through one side of a branch is both non-symmetrical and through a curved pipe of varying diameter.

The shape of the branches to be used was determined by extending Murray's (1926) theory on the physiological principle of minimum work discussed in section 2. It was considered that a complete study of the flow in one shape of branch would be of greater value than only studying one or two aspects of the flow in many branches. This was supported by the preliminary findings of Schreck and Mockros (1970) in air flow which showed that there was little variation in the downstream velocity profile with branching angle, though they did in fact only investigate this at two positions downstream for angles of 21^{o} and 40^{o}. Hence, just the one symmetrical shape was chosen from the results given in section 2.2 and two branches

were made up in this shape, one with sharp-cornered inside geometry and the other with the corners smoothed out to a radius of 5.0cm. so that the effect of inside geometry could be considered in all experiments.

Difficulties in setting up specific flow conditions in the limbs of the branch coupled with the suggestions of Cutler and Burbank (1968) that the Coanda effect could be of significance in branching blood vessels led to the first detailed investigation, that of the relationship between the downstream pressures on each limb and their relative flow. This is described in section 3 which includes a short section on the effect of obstructions near the branch carina. Section 4 describes and explains the detailed flow patterns observed within the branch and includes a subsection on experiments conducted with one limb completely occluded. Section 5 describes the design, calibration and use of a directionally-sensitive, thin film velocity probe for the measurement of axial velocity and measurements and analysis of the velocity distributions downstream of the branches are presented in section 6. Before pulsatile flows could be studied in detail, it was required to formulate a methodology for the measurement and processing of pulsatile flow velocities and this is described in section 7. Section 8 is concerned with the pulsatile flow velocity distributions downstream of the branches and an investigation into the shear stress distribution in the branches is described in section 9. Finally, a short section is included on some of the physiological implications of the experimental results and some suggestions put forward for further work.

1.2 Experimental Apparatus

A diagrammatic view of the experimental layout is shown in figure 1.1. Steady water flow was supplied from a constant head tank through a control valve and settling chamber to a rigid, Perspex tube, 25.4 mm. in diameter and 3.5 metres long to ensure developed flow. The model branches were situated in a horizontal plane at the end of this rigid tube and each had a 25.4 mm. diameter inlet and two 19 mm. diameter daughter tubes. They are described more fully in section 2.3. The length of each 19 mm. diameter daughter tube was variable, depending on the experiment, and each was connected via a three metre length of 25.4 mm. diameter flexible tubing to one side of a head tank fitted with an adjustable weir. The position of the water surface in each tank could be measured by means of a micrometer head fitted with a pointer and mounted above each tank. From the exit side of the head tank, the water flowed down through a restricting nozzle, the pressure just upstream of the restriction being measured by the head of water standing in a calibrated tube. Bernouilli's equation gives $Q^2=f(h)$ where Q is the flowrate and h the head of water and by using differently sized restictors, flows of any magnitude could be read off directly with errors of the order of only 2%. Calibrations for reading the flowrates directly were made experimentally.

Pulsatile flow was obtained by means of a piston acting on the fluid in the settling chamber. The piston was operated by an electric motor through a cam and follower

arrangement, details of which can be found in Bellhouse and Bellhouse (1969a). By varying the three independent controls of flowrate, frequency and amplitude, a pulse of any desired mean flowrate, frequency and backflow ratio could be obtained.

Plane flow visualisation was obtained by using the technique of electrolysing the water as described by Clutter and Smith (1961). Two platinum wires, each 0.002 inches in diameter, were stretched across the tube 5 mm. apart and a voltage applied across them. Electrolysis of the water took place and hydrogen and oxygen bubbles were formed at the two wires and carried off downstream to form an effective planar flow tracer. One of the difficulties however was that the oxygen bubbles were much larger and therefore more buoyant than the hydrogen bubbles and had too fast a rise time. To counter this, the platinum wire anode was replaced by a 0.005 inch diameter copper wire which had the effect of absorbing the oxygen to form copper oxide. This was successful although the copper wire was short-lived and dissolved within minutes. In general, therefore, platinum wires were used and the oxygen bubbles ignored. A refinement which greatly improved the tracer was to replace the platinum wire cathode with a similar wire which had been bent into a triangular waveform of about 0.8 mm. pitch. Hydrogen tended to be released into the flow only at the points of the triangles and this gave a much clearer indication of the streamlines. The triangular waveform was obtained by running the wire between two gear

wheels from a watch mechanism. A further refinement was the triggering of the tracer from the piston of the pulsatile flow pump, causing bursts of bubbles to be produced in phase with the pulse.

2. THE SHAPE OF BRANCHING BLOOD VESSELS

2.1 Theory

Murray (1926a) has described a principle that since evolution will have tended to favour more efficient systems to the detriment and eventual extinction of less efficient ones, the present-day human and animal blood vessel systems will be so evolved as to present minimum effort to the body in maintaining life. This principle is termed the physiological principle of minimum work and it has been applied by Murray (1926b) to the problem of finding the optimum shape of branching blood vessels using the parameters of Poiseuille flow and a term involving the cost of maintenance of blood volume. This resulted in a set of equations relating the four variables r_1/r_0, r_2/r_0, x and y, these being respectively the ratios of the radii of the daughter tubes to the parent tube and their respective angles to the line of the parent tube. (See section in Notation). The shape of the branch was uniquely determined by the flowrate required in each limb.

It was considered that the energy transfer from the blood through the vessel walls was greater than the energy required to maintain the volume of blood itself and that therefore Murray's parameter of the cost of maintenance of blood volume should be replaced by a term dependent on the surface area of the blood vessel walls.

Consider unit mass of blood, occupying a volume V, passing down a section of artery, sufficiently small so

that the pulsating energy terms can be neglected. In time t it travels a distance ℓ. The total specific energy transfer is given by: $-de = dE - dW$ where dE is the heat and other energy forms in, dW is the work out and +de indicates a loss from the vessel.

$$\therefore \quad -\frac{de}{dt} = \frac{dE}{dt} - \frac{dW}{dt}$$

Now the heat transfer is through the vessel wall and depends on the surface area of that wall. i.e. $\frac{dE}{dt} = -k.2\pi r\ell$ where k is the rate of heat transfer per unit surface area and r is the vessel radius.

Also, $\frac{dW}{dt} = \frac{d}{dt}\int V\,dP = (P_1 - P_2)Q$ where Q is the volume flow-rate.

Hence, $-\frac{de}{dt} = -2\pi k\ell r - (P_1 - P_2)Q$

and hence the specific power supplied to the blood is

$$\frac{de}{dt} = 2\pi k\ell r + (P_1 - P_2)Q \qquad (2\text{-}1)$$

Now, Poiseuille's Law gives: $P_1 - P_2 = \frac{8\mu\ell Q}{\pi r^4}$ where μ is the viscosity.

Hence
$$\frac{de}{dt} = 2\pi k\ell r + \frac{8\mu\ell Q^2}{\pi r^4}$$

Evolution will dictate that the most efficient systems will be the most likely to survive and hence the principle of minimum specific power can be applied with respect to the vessel radius.

Thus, $\frac{d}{dr}\left(\frac{de}{dt}\right) = 2\pi k\ell - \frac{32\mu\ell Q^2}{\pi r^5}$

$= 0$ when $r^5 = \frac{16\mu}{k\pi^2}\,Q^2$

Also, $\frac{d^2}{dr^2}\left(\frac{de}{dt}\right) = \frac{160\mu\ell Q^2}{\pi r^6}$ which is greater than zero so this extremum is a minimum.

Therefore, if the power is minimal,

$$\underline{Q = K\, r^{2.5}} \qquad (2\text{-}2)$$

where $K^2 = \dfrac{k\pi^2}{16\mu}$

Therefore, $\left(\dfrac{de}{dt}\right)_{min.} = 2\pi k \ell r + \dfrac{8\mu\ell}{\pi r^4} \cdot \dfrac{k\pi^2 r^5}{16\mu}$

$$\Longrightarrow \left(\frac{de}{dt}\right)_{min.} = 2.5\ \pi k \ell r \qquad (2\text{-}3)$$

The configuration in a branching system will also be such as to present the minimum possible power loss and the principle of virtual work can be applied to the system in order to obtain an equation or equations connecting the variables concerned. There are three possible small deflections from the equilibrium position and these are shown below in figure 2.1.

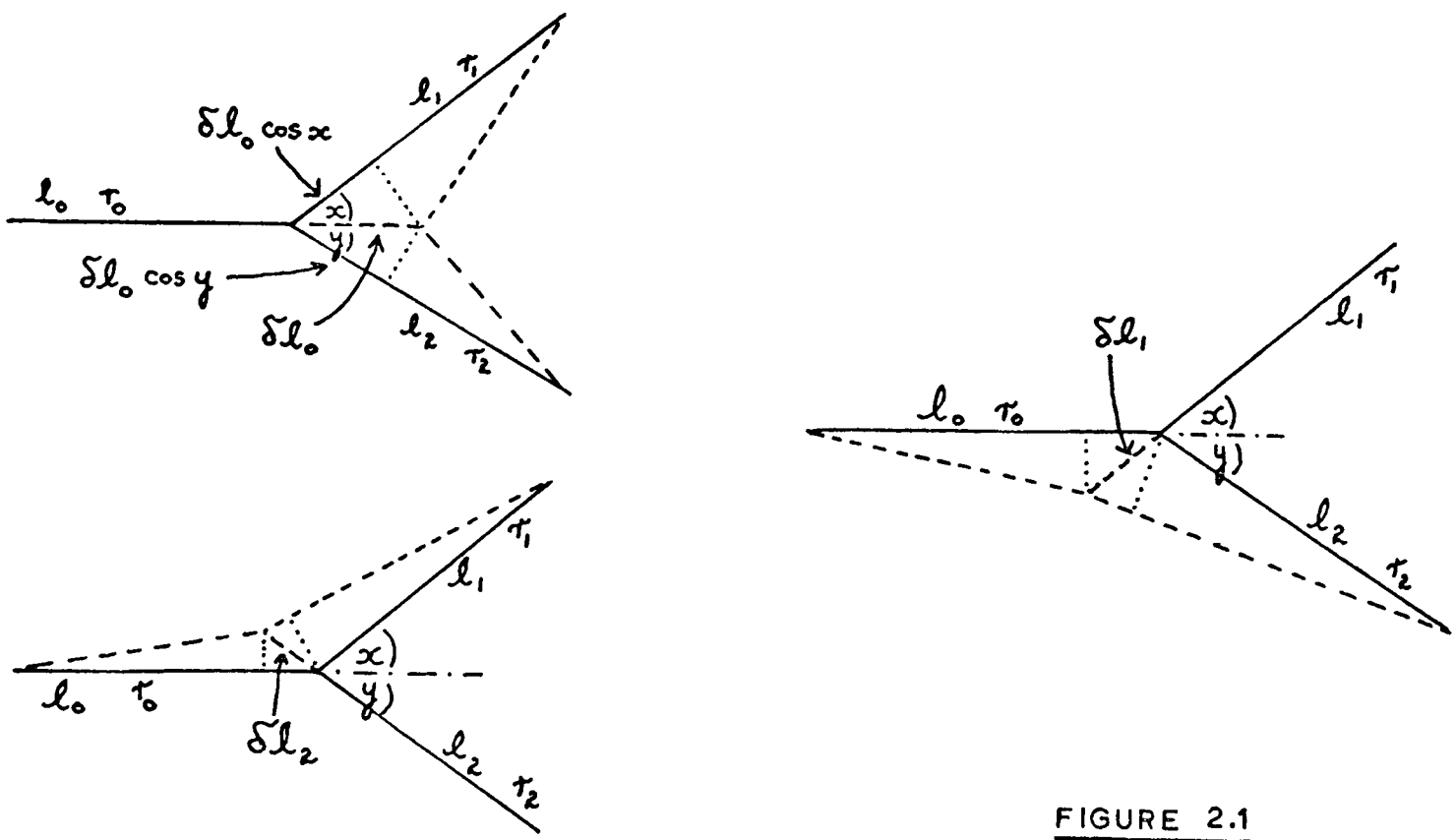


FIGURE 2.1

VIRTUAL WORK DIAGRAM

Since $\left(\frac{de}{dt}\right)_{min.}$ is proportional to ℓr, for each of the above deflections from the assumed minimum work configuration, $d(\ell r) = 0$.

i.e. $$r_0\delta\ell_0 - r_1\delta\ell_0 \cos x - r_2\delta\ell_0 \cos y = 0$$

$$- r_0\delta\ell_1 \cos x + r_1\delta\ell_1 + r_2\delta\ell_1 \cos (x+y) = 0$$

$$- r_0\delta\ell_2 \cos y + r_1\delta\ell_2 \cos (x+y) + r_2\delta\ell_2 = 0$$

Hence
$$r_1 \cos x + r_2 \cos y = r_0$$

$$r_0 \cos x - r_2 \cos (x+y) = r_1$$

$$r_0 \cos y - r_1 \cos (x+y) = r_2$$

Therefore, by Cranmer's rule :
$$\cos x = \frac{r_0^2 + r_1^2 - r_2^2}{2\, r_1 r_0}$$

$$\cos y = \frac{r_0^2 - r_1^2 + r_2^2}{2\, r_2 r_0}$$

$$\cos (x+y) = \frac{r_0^2 - r_1^2 - r_2^2}{2\, r_1 r_2}$$

Now since $Q_0 = Q_1 + Q_2$ (continuity), from equation (2-2),

$$r_0^{2.5} = r_1^{2.5} + r_2^{2.5} \qquad (2\text{-}4)$$

This compares with Murray's result of $r_0^3 = r_1^3 + r_2^3$ (2-5)

Hence, denoting r_1/r_0 by p, r_2/r_0 by q and r_1/r_2 by s, the equations can be written as follows:

$$\left.\begin{aligned} \cos x &= \frac{1 + p^2 - (1 - p^{2.5})\ 0.8}{2\ p} \\ \cos y &= \frac{1 + q^2 - (1 - q^{2.5})\ 0.8}{2\ q} \\ \cos (x+y) &= \frac{-1 - s^2 + (1 + s^{2.5})\ 0.8}{2\ s} \end{aligned}\right\} \qquad (2\text{-}6)$$

These compare with Murray's equations, taken from Murray (1926b) which are as follows:

$$\left.\begin{aligned} \cos x &= \frac{1 + p^4 - (1 - p^3)^{4/3}}{2\,p^2} \\ \cos y &= \frac{1 + q^4 - (1 - q^3)^{4/3}}{2\,q^2} \\ \cos (x+y) &= \frac{-1 - s^4 + (1 + s^3)^{4/3}}{2\,s^2} \end{aligned}\right\} \quad (2\text{-}7$$

A short computer program was written to solve both sets of equations and the values of r_2/r_0, r_1/r_2, x and y were computed for values of r_1/r_0 ranging from 0.02 in steps of 0.02 to 0.98. Graphical plots of r_2/r_0 and x and y against r_1/r_0 are shown in figures 2.2 and 2.3 respectively. It can be seen that there is no great distinction between the two sets of results, the main difference being in the variation of (x+y) with r_1/r_0 though in either case (x+y) does not vary from 90^o by more than 17% for any value of r_1/r_0. The basic result in both cases is that the smaller the diameter ratio of daughter tube to parent, the greater is the angle at which the daughter tube leaves the parent. e.g. a very small tributary leaving a main stream should branch off almost at right angles.

2.2 Experimental Observations

Groat (1948) performed experimental measurements on vessels between 24 and 3200 microns diameter and found that the volume flowrate, Q, varied with diameter, d, according to $Q = kd^n$ where n varied between 2.1 and 3.1

with a mean of 2.6. He therefore postulated that at a junction since $Q_o = Q_1 + Q_2$ (continuity) then:

$$d_o^{2.6} = d_1^{2.6} + d_2^{2.6} \qquad (2\text{-}8)$$

and further experiments showed that the greatest discrepancy between the diameters calculated from equation (2-8) and experimental measurements of diameter was only 3.2%. This would indicate that equation (2-4) is to be preferred to Murray's equation (2-5).

For a symmetrical branch, equation (2-4) gives d_1/d_o = 0.76 which gives an increase in cross-sectional area from the parent tube to the two limbs of 1.15. Murray's results give d_1/d_o = 0.79 with an associated cross-sectional area increase of 1.26. These both agree with Groat's results which give d_1/d_o = 0.77. Caro's (1971) measurements, however, suggest that there is little, if any, change in cross-sectional area at arterial branching sites which would imply that for a symmetrical branch, the ratio d_1/d_o= 0.71. Alexander (1954) estimated that after five branches, the area of the vascular bed in the region of the abdominal aorta had increased by a factor of 1.4 which would imply an increase of 1.07 per branch with an associated value of d_1/d_o of 0.73. At the bifurcation of the human aorta, Hess (1927) gives the area increase as 1.13 (d_1/d_o = 0.75) though this is contested by Caro (1971) who found a mean value of 0.75 (d_1/d_o = 0.61). In general therefore, the experimental observations indicate a value for d_1/d_o of around 0.73 which agrees well with the theoretical equation (2-4).

The measurement of the angles x and y presents considerable difficulty since vessels frequently curve sharply after branching, and no detailed work on this aspect appears to have been published.

2.3 The Shape of Model Branches

A symmetrical branch was required for the experimental work and it was decided from the observations in section 2.2 above to take a daughter to parent tube diameter ratio of 0.75. This gave an increase in cross-sectional area in passing through the branch of 1.125. The values of the angle between daughter and parent tube for a symmetrical branch were given by equations (2-6) as 49^{o} and by Murray's equations (2-7) as 38^{o}. A value of 45^{o}, giving a right angle between the limbs, was therefore chosen as a compromise.

Two model branches were made up in this shape, both with inlet tube diameters of 25.4 mm. and daughter tube diameters of 19 mm. One of the branches had sharp-cornered inside geometry and the other had the inside curve smoothed out to a radius of 5.0 cm. These branches were given the identifying numbers 1 and 2 respectively and they are drawn in detail in figures 2.4 and 2.5. In order to facilitate the use of velocity probes and flow visualisation devices within the branch, both models were made out of two halves of a Perspex block screwed together.

3. THE EFFECT OF SMALL PRESSURE DIFFERENCES IN BRANCHES.

3.1 Introduction

It was found that very small differences between the pressures in each limb led to pronounced switching of the flow to the limb with the lower pressure. On an inlet flow of 50 ml./sec. (3.0 litres/min.) a difference in pressure of only 7 mm. of water (0.5 mm. of mercury) could switch the flow completely down the lower pressure limb. Cutler and Burbank (1968) have suggested that the Coanda effect, where a jet of fluid tends to cling to one or other of the vessel walls, as in fluid logic devices, might have a significant effect in branching blood vessels. Although there is no initial jet within the branch, it is possible that a small jet could be formed from where the daughter tubes begin to leave the parent tube and some form of the Coanda effect then take place. In order to investigate whether or not the flow switching observed was due to the Coanda effect, a detailed investigation of the pressure-flow relationships within the branch was undertaken over a wide range of flowrates. A calculation of the downstream pressure drop was also undertaken in order that the experimental results could be referred to this.

Three branches were used in the investigation. In addition to branches 1 and 2 described in section 2.3, a third branch, branch 3, was used with the same sized parent and daughter tubes as in branches 1 and 2 but with both

daughter tubes being at right angles to the line of the parent tube.

3.2 Calculation of the Downstream Pressure Drop

In order to ascertain the downstream pressure drop in each limb, pressure tappings were made at three points, at inlet and exit of the branch and just before entry to the head tank. Pressure readings were taken for various flows in branch 1 where generally laminar flow was to be expected and also in branch 3 where generally turbulent flow was to be expected in the daughter tube. No pressure measurements were carried out in branch 2 as it was expected that these would be very similar to those in branch 1. The application of Bernouilli's equation to a streamline passing these three points gives:

$$P_j/\rho + \tfrac{1}{2} u_j^2 + gh_j = P_{j+1}/\rho + \tfrac{1}{2} u_{j+1}^2 + gh_{j+1} + gh_{Lj}$$

where subscript j refers to properties at tapping j, and h_{Lj} is the head loss between tappings j and j+1, measured in cm. of water. Computing u_j^2 in terms of Q_i^2 or Q^2, the following equations were obtained:

$$h_{L1} = H_1 - H_2 + (1.98Q^2 - 6.27Q_i^2) \times 10^{-5}$$

$$h_{L2} = H_2 - H_3 + 4.29 \times 10^{-5} Q_i^2$$

where H_j is the total static head at tapping j measured in cm. of water. Using these equations, the values of h_{L1} and h_{L2} were computed for each branch from the measurements of H_j, Q and Q_i, and graphs were drawn of h_{L1}/Q_i and

h_{L2}/Q_i against Q_i. These graphs are shown in figure 3.1. Straight lines resulted in all cases giving the following relationships:

Branch 1 : $h_{L1} = 1.6\text{x}10^{-3}\ Q_i$

$h_{L2} = 5.9\text{x}10^{-3}\ Q_i + 7.1\text{x}10^{-5}\ Q_i^2$

Branch 3 : $h_{L1} = 2.5\text{x}10^{-3}\ Q_i + 8.9\text{x}10^{-5}\ Q_i^2$

$h_{L2} = 5.9\text{x}10^{-3}\ Q_i + 7.1\text{x}10^{-5}\ Q_i^2$

In each case, h_{L1} is the head loss within the immediate vicinity of the branch and h_{L2} is the head loss through the rest of the downstream system, excluding the final head tank, which is the same for both branches. As expected, the loss of dynamic head in branch 3 is much greater than the similar loss in branch 1 and this is due to the 90° turn which the fluid makes in passing through branch 3.

Adding in the dynamic head loss into the head tank of $u^2/2g$ (which is $2.0\text{x}10^{-5}Q_i^2$), and transferring into units of pressure by multiplying through by ρg, the total pressure drop down each limb was found to be:

Branch 1 : $\Delta P = 7.3\ Q_i + 0.089\ Q_i^2$ (3-1)

Branch 3 : $\Delta P = 8.2\ Q_i + 0.176\ Q_i^2$ (3-2)

Putting i = a and b in turn into equations (3-1) and (3-2) and subtracting, the following equations were obtained:

Branch 1 : $P_b - P_a = 7.3(Q_a - Q_b) + 0.089(Q_a^2 - Q_b^2)$

Branch 3 : $P_b - P_a = 8.2(Q_a - Q_b) + 0.176(Q_a^2 - Q_b^2)$

and hence, since $Q_a + Q_b = Q$, the total flowrate, putting $\alpha = Q_a/Q$,

Branch 1 : $$P_b - P_a = (7.3Q + 0.089Q^2)(2\alpha - 1) \qquad (3\text{-}3)$$

Branch 3 : $$P_b - P_a = (8.2Q + 0.176Q^2)(2\alpha - 1) \qquad (3\text{-}4)$$

Thus, if no Coanda effect is present, the pressure - flow investigations should yield equations similar to equations (3-3) and (3-4) for all Q and α. If some form of flow switching is present that is not directly attributable to the interaction of the pressure drops in each limb, then the flow distribution will not be progressively adjustable and there will be a discontinuity in the equations.

3.3 Experimental Investigation

Branch 1

Measurements of the position of the water head surface in each limb, H_a and H_b, and the percentage flows down each limb were taken for total flows of approximately 25, 50, 75, 100, 125, 150, 175 and 200 ml./sec. The height of weir B was fixed and the height of weir A was varied until a state of equiflow was achieved. i.e. the flow down each limb was the same. Weir B was then raised by successive amounts and the flows either read off on the flowmeters or, when they were too low to be so read, measured by means of a measuring cylinder and stopwatch.

For each set of readings, a mean total flow was calculated and ΔH, the change in the head in B minus the

change in the head in A from the equiflow heads, was calculated from:

$$\Delta H = (H_b - (H_b)_O) - (H_a - (H_a)_O)$$

where H_i is the position of the head surface on limb i at any particular weir position and $(H_i)_O$ the position at the equiflow state. The flows in the limbs were recorded in a normalised state with respect to the mean total flow, this being achieved by the normalising equation:

$$\text{Normalised Flow} = \frac{\text{measured flow in limb}}{\text{measured total flow}} \times \text{mean total flow},$$

for each measured flow.

A set of low flow measurements was also taken for total flows of approximately 4, 9, 14 and 19 ml./sec. It was too difficult to adjust the weirs to obtain an equiflow position owing to the large changes occurring in flowrate for small changes in weir height so weir A was positioned so that the flow in B was greater than 50% of the total flow. Then on raising weir B, the flow in B becoming smaller, the equiflow position would at least be passed through. Graphs were drawn of percentage flow in A against $H_b - H_a$ and thus the value of $H_b - H_a$ at the equiflow position i.e. $((H_b)_O - (H_a)_O)$ could be read off from the graph. A summary table was drawn up showing mean total flow, percentage flows, normalised flows obtained as above, $H_b - H_a$ and ΔH, obtained by subtracting the value of $((H_b)_O - (H_a)_O)$ from $H_b - H_a$. These low-flow results were not as consistent as expected so a further set of measurements was taken for total flows

of approximately 5, 7.5 and 15 ml./sec., the head measurements being read four times and a mean taken to ensure accuracy. Figure 3.2 shows a typical flow distribution using the Hydrogen bubble tracer for a flowrate of 50 ml./sec. and a pressure difference of 5½ mm. of water between the daughter tubes which diverted 90% of the flow. This can be compared with figure 3.3 which shows the same flowrate diverted equally down each limb.

Branches 2 and 3

A similar procedure to the above was carried out for branch 2 for total flows of approximately 4.5, 6.5, 16.5, 25, 50, 75, 100, 125, 150, 175 and 200 ml./sec. and for branch 3 for total flows of approximately 17, 25, 50, 75, 100, 125, 150, 175 and 200 ml./sec.

3.4 Analysis of Experimental Data

For each branch a set of graphs was plotted of percentage flow in limb A against ΔH. For each value of Q a straight line resulted of the form

$$\alpha = f(Q). \quad \Delta H + 0.5 \qquad (3\text{-}5)$$

where α is the ratio of the flow in limb A to the total flow (i.e. 100 α is the percentage flow in limb A), the gradient, $f(Q)$, being a function of Q and the branch only. Examination of the variation of $f(Q)$ with Q for each branch showed that

$$\frac{1}{f(Q)} = k_1 Q + k_2 Q^2 \qquad (3\text{-}6)$$

where k_1 and k_2 were constants. To determine the values of k_1 and k_2, the function $1/Qf(Q)$ was plotted against Q and as shown in figure 3.4 straight lines resulted for each branch with almost negligible scatter though there was some slight curving off at very low flowrates. The values of k_1 and k_2 thus found are shown in Table 3.1.

Branch	k_1	k_2
1	0.157	2.03×10^{-3}
2	0.152	1.93×10^{-3}
3	0.157	2.86×10^{-3}

Table 3.1.

Combining equations (3-5) and (3-6),

$$\alpha = \frac{\Delta H}{k_1 Q + k_2 Q^2} + 0.5$$

which gives

$$\Delta H = \tfrac{1}{2}(k_1 Q + k_2 Q^2)(2\alpha - 1)$$

Transferring into units of pressure and using the values of k_1 and k_2 from table 3.1, the following equations were obtained:

Branch 1 : $P_b - P_a = (7.7\ Q + 0.10\ Q^2)(2\alpha - 1)$ (3-7)

Branch 2 : $P_b - P_a = (7.5\ Q + 0.095\ Q^2)(2\alpha - 1)$ (3-8)

Branch 3 : $P_b - P_a = (7.7\ Q + 0.14\ Q^2)(2\alpha - 1)$ (3-9)

These equations are of exactly the same form as the equations calculated from the interaction of the pressure drops down each limb, equations (3-3) and (3-4),

and there is good correlation between the experimental constants in equations (3-7) and (3-9) and the constants calculated from the pressure drops in equations (3-3) and (3-4), the mean absolute difference being 10%. No discontinuities were observed in the experimental investigation and the flow distribution could be varied progressively in all cases.

There was thus no evidence of any form of Coanda effect in the shapes of branch studied. It is possible, however, as Cutler and Burbank (1968) have suggested that a stenosis immediately prior to a branch could have an effect on the flow pattern, producing a jet which might well aid the establishment of a Coanda effect. This however has not been studied.

A further conclusion from the experiments described in this section is that the inside geometry of the branch has very little, if any, effect on the pressure drop through the branch. The differences in the constants in table 3.1 for branches 1 and 2 is minimal and well inside the limits of experimental error. On changing the shape of the branch, however, the pressure drop through the branch increases as the angle between parent and daughter tube increases as can be seen by comparing the constants for branches 1 and 3.

Preliminary studies in pulsatile flow showed that the amount of switching was consistent with the same mean steady flow. Flow visualisation observations using the electrolysing wires showed that the amount of switching

varied directly with the velocity pulse, beginning in a completely switched state, moving towards the equiflow position through the accelerating phase and returning toward a completely switched state as the velocity returned to zero. This was in accordance with equations (3-7) to (3-9) which show that for a given pressure difference the amount of flow switching varies inversely with velocity.

The small magnitudes of pressure difference required to switch the flow could have medical implications since they could possibly be a cause of blood vessel starvation in the circulation. If some form of occlusion or clot formation began to increase the pressure in one limb of an arterial branch, then less blood would flow down the limb according to the principles discussed in this section. This could possibly enable the growth or clot to form more quickly and thus lead through a positive feedback effect to complete blood starvation of the affected limb. Restrictions on blood vessels giving the same flow switching effects might also occur generally when limbs are moved or parts of the body compressed.

3.5 The Effect of Obstructions near the Branch Carina

To see if obstructions in the branch could switch the flow between the two limbs, the following experiment was conducted. Spherical balls of aluminium foil were made up and each was attached to two long pieces of thin thread. The ball was then introduced into the parent tube a long way upstream of the branch where it did not

affect the branch flow regime and the pieces of thread arranged so that it could be drawn into the position shown below in figure 3.5 without any disturbance of the branch itself.

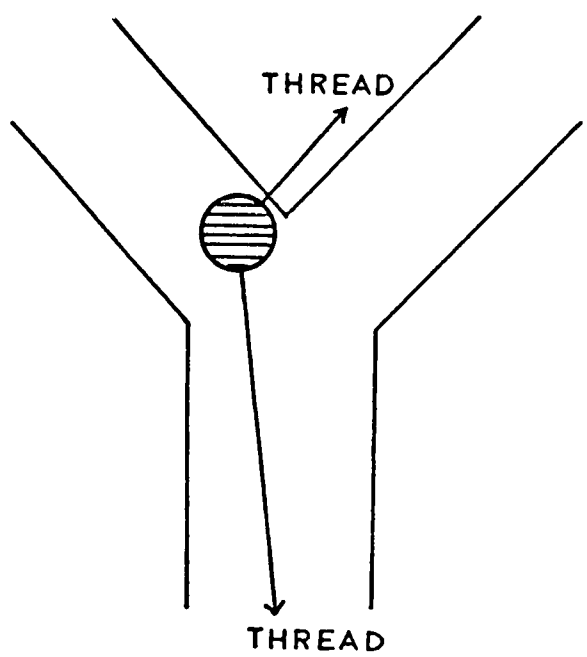


FIGURE 3.5

POSITION OF OBSTRUCTION IN BRANCH

The positioning of the ball was arranged so that it sat just on one side of the carina where it would have the greatest effect on the flow. The main observations were made at an inlet Reynolds' Number (ud/ν) of 1550 though the results were checked at other Reynolds' Numbers to see if any significant variation were apparent.

No change in the relative flowrates of the daughter tubes was observed when spherical balls of 0.9 cm. and 1.15 cm. diameter were drawn into position at the carina but for a ball of 1.75 cm. diameter which blocked 85% of the daughter tube, the flow was switched from the equiflow state to a state in which the flow distribution

was 23% in the obstructed tube and 77% in the unobstructed tube. From equation (3-7) this was equivalent to a pressure difference between the daughter tubes of 1.8 mm. of water. A ball of 1.77 cm. diameter in a tube of 1.90 cm. diameter with 23% of the inlet flow passing it, however, gives rise to an increase in dynamic head of 1.8 mm. of water, the same as the pressure difference required to switch the flows as observed, and this theoretical ball is the same size as the experimental ball to within 1.2%. Hence the switching effect of the obstructing ball was entirely accounted for by the pressure difference set up by the increase of dynamic head around the ball. This was confirmed by the lack of any switching of the flow when using the smaller balls since the dynamic head increase was negligible save when the ball was very nearly occluding the whole of the tube. Observations were also made with the obstructions on the other side of the carina and similar results were noted. Experiments at other flow-rates confirmed the findings.

Conclusion

The carina of the branch is not sensitive to obstructions placed against it until the size of the obstruction becomes such as to make a significant increase in the dynamic head whereupon the flow distribution will change according to the findings on small pressure differences expressed in equations (3-7) to (3-9) in section 3.4.

4. THE STREAMLINE PATTERN WITHIN THE BRANCH

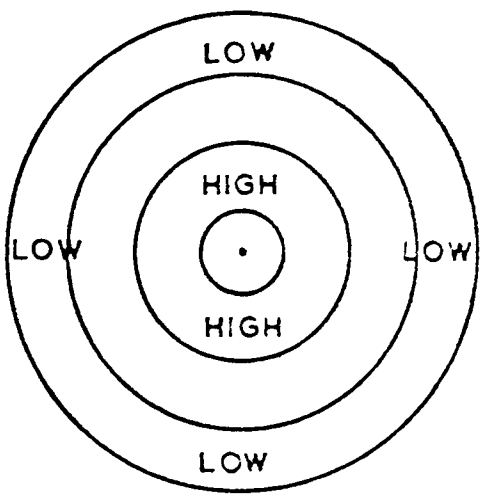
4.1 The Formation of Secondary Flows

When a fluid is flowing in a curved path, each element of fluid receives a centrifugal force of mu^2/R where m is the mass of the element, u the axial velocity of the element in the plane of the bend and R the radius of curvature of the bend. There is thus an overall outward force exerted by the fluid on the bend which is countered by a pressure gradient set up by the bend on the fluid. Assuming that m and R are approximately constant for all fluid elements, i.e. that the bend radius is large compared with the tube radius, those elements with the highest velocities will have centrifugal forces which are greater than the mean pressure gradient and will hence be under the influence of a net centrifugal force. Similarly, those elements with the lowest velocities will have centrifugal forces which are less than the mean pressure gradient and will hence be under the influence of a net centripetal force. There will therefore be a relative movement of the fluid elements within the cross-section and this constitutes what is known as a secondary flow.

In the case of a single sharp bend or elbow, where curved streamlines are not established, the change in momentum flux is a more meaningful concept than that of centrifugal forces. Those elements with the highest momentum flux will have the greatest inertia to the transverse forces turning the fluid and will hence continue as far as

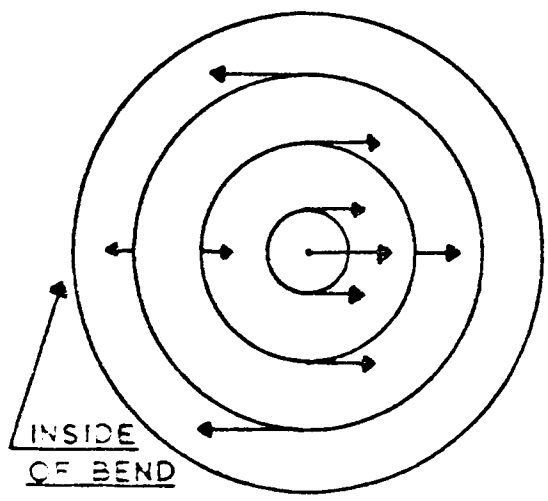
possible to the outside of the bend forcing elements with lower momentum flux to the inside. Since momentum flux is proportional to the square of velocity, as also is centrifugal force, the secondary flow effects are similar.

The exact nature of the secondary flow set up in a fluid moving in a curve or bend will depend on the input velocity profile to the bend. For a parabolic input velocity profile, the high velocities are in the centre of the tube and the low velocities on the outside. A secondary flow is thus set up in the form of two contra-rotating vortices as shown in figures 4.1 to 4.3 below and the combination of these secondary vortices with the axial velocity gives the flow a double helical motion as it moves downstream.



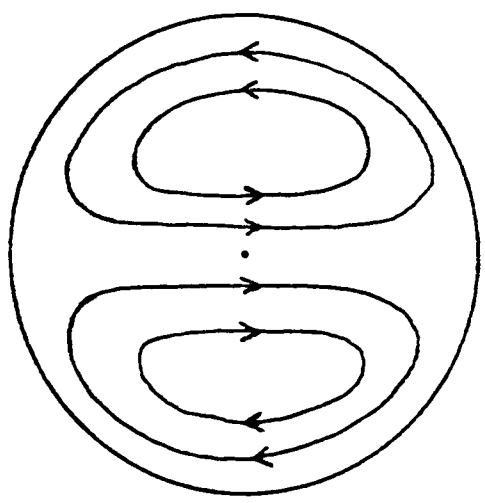
PARABOLIC INPUT

FIGURE 4.1



NET FORCES

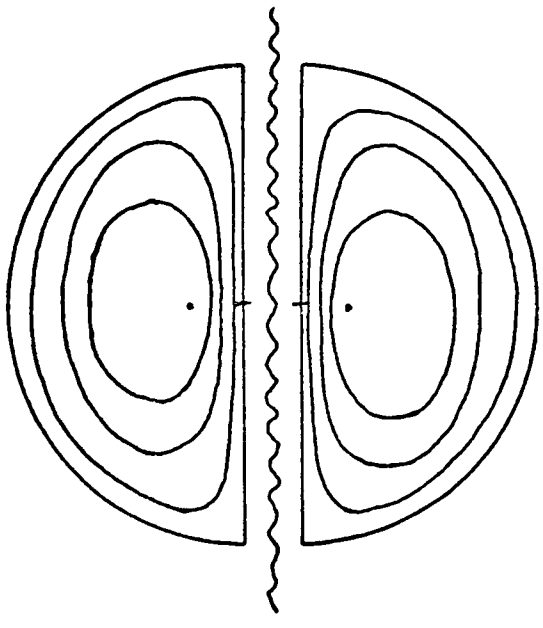
FIGURE 4.2



SECONDARY FLOW

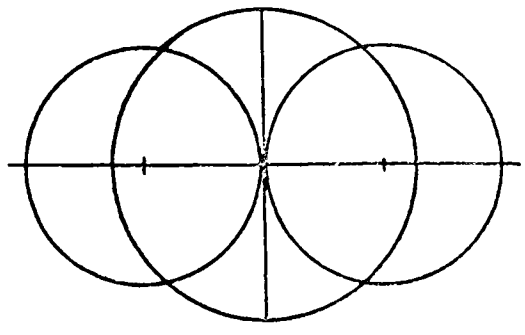
FIGURE 4.3

Each limb of the branch was a curved tube structure and so it was possible that secondary flows would be set up downstream in the same manner as above. Since half of the parent tube input was carried down each limb, however, the input velocity profile to each bend was in the form of a semi-parabola, as shown in figure 4.4 below, with the high velocities on the outside of the bend and the low velocities on the inside. Hence the high velocity elements would not be able to move significantly further towards the outside of the bend as was the case with a full parabolic input profile and this might well inhibit the formation of secondary flows. The branch, however, was not a simple curve even when only one half of the input was considered. As shown in figure 4.5 below,the fluid in each half of the parent tube had to move through a change in cross-sectional shape, from a 25 mm. diameter semicircle to a 19 mm. diameter circle, and this change in itself might well be expected to set up secondary flows of some form.



INPUT PROFILE TO LIMBS

FIGURE 4.4



CROSS SECTIONAL SHAPE CHANGE

FIGURE 4.5

4.2 Experimental Studies

It should be noted that the terminology in this section depends on whether reference is being made to the branch and its daughter tubes or to the bend. The inside wall of the branch is also the outside wall of the bend and vice versa.

Assuming the sharp-cornered branch 1 to be a 45^{o} elbow, and considering elemental thickness of fluid in the horizontal plane of symmetry of the bend, the total force on the bend caused by the change in momentum flux is:

$$\frac{\rho a u^2}{\sqrt{2}}$$

where a is the radius of the input tube. This acts over an area of the wall of the branch of $a\sqrt{2}$ and thus the excess pressure on the outside wall of the bend (inside wall of the branch) is $\frac{\rho u^2}{2}$. Taking ρ= 1 gm./c.c. and u = 7.0 cm./sec., the root mean square value of a parabolic profile of mean velocity 6.1 cm./sec., the excess pressure on the outside wall of the bend should be 25 dynes/sq.cm. (0.025 cm. of water).

An experimental investigation of the pressure difference across the daughter tubes was made 3 cm. downstream of the branch carina, which was as near as the carina could be approached, in a parabolic input flow of mean velocity 6.1 cm./sec. An S.E.1150 pressure transducer was used and it was confirmed that the pressure difference across the horizontal plane of symmetry at this position was close to 25 dynes/sq.cm. The extremely low pressures involved,

however, meant that the transducer was operating at the extreme end of its most sensitive scale which could possibly cast doubt on the numerical accuracy of the measurements. Nevertheless, the pressure difference measured was certainly of the correct order of magnitude. Further measurements showed that the pressures at top and bottom of the daughter tubes were equal and both were approximately 6 dynes/sq.cm. above the pressure on the inside wall of the bend.

To study the detailed flow patterns, dye was injected into the flow upstream of the branches at various points in the cross-section. Using a number of differently coloured dyes, careful note was taken of the passage of each streamline through the branch. Colour photographs were taken so that the streamline pattern could be recorded and studied.

Preliminary observations showed that a secondary flow was set up downstream of the branch in the form of two contra-rotating vortices, similar to those shown in figure 4.3 but confined at first mainly to the outside of the limb. This secondary flow was caused by the fluid from top and bottom of the inlet (areas 1 and 2 in figure 4.6 below) moving to the outside of the limb (areas 5 and 6 in figure 4.6) where it became strongly vortical, while the fluid near the centre of the inlet (areas 3 and 4 in figure 4.6) continued through to the inside of the limb with little interference, though some contra-rotating vorticity was apparent.

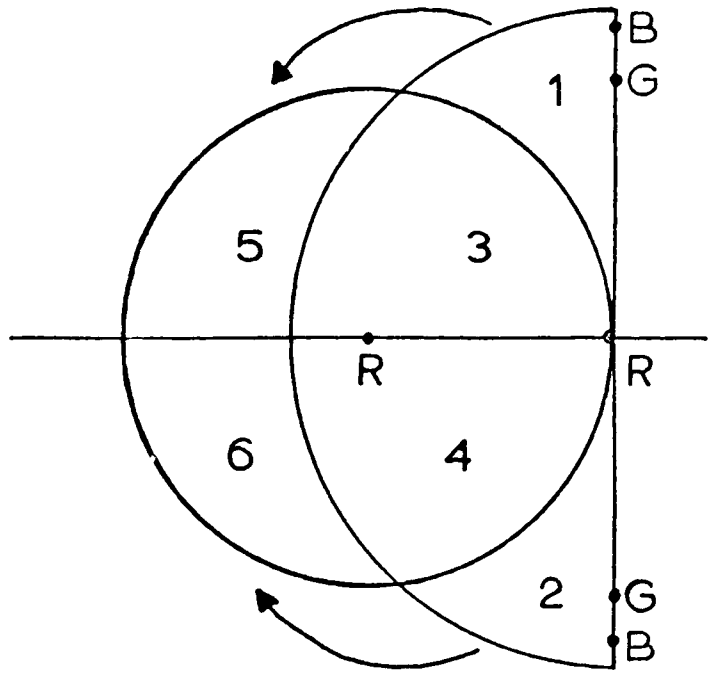


FIGURE 4.6

FLUID MOVEMENT

The vortices on the outside of the limb spread across the limb within about 9 cm. downstream and then gradually died out as they moved downstream.

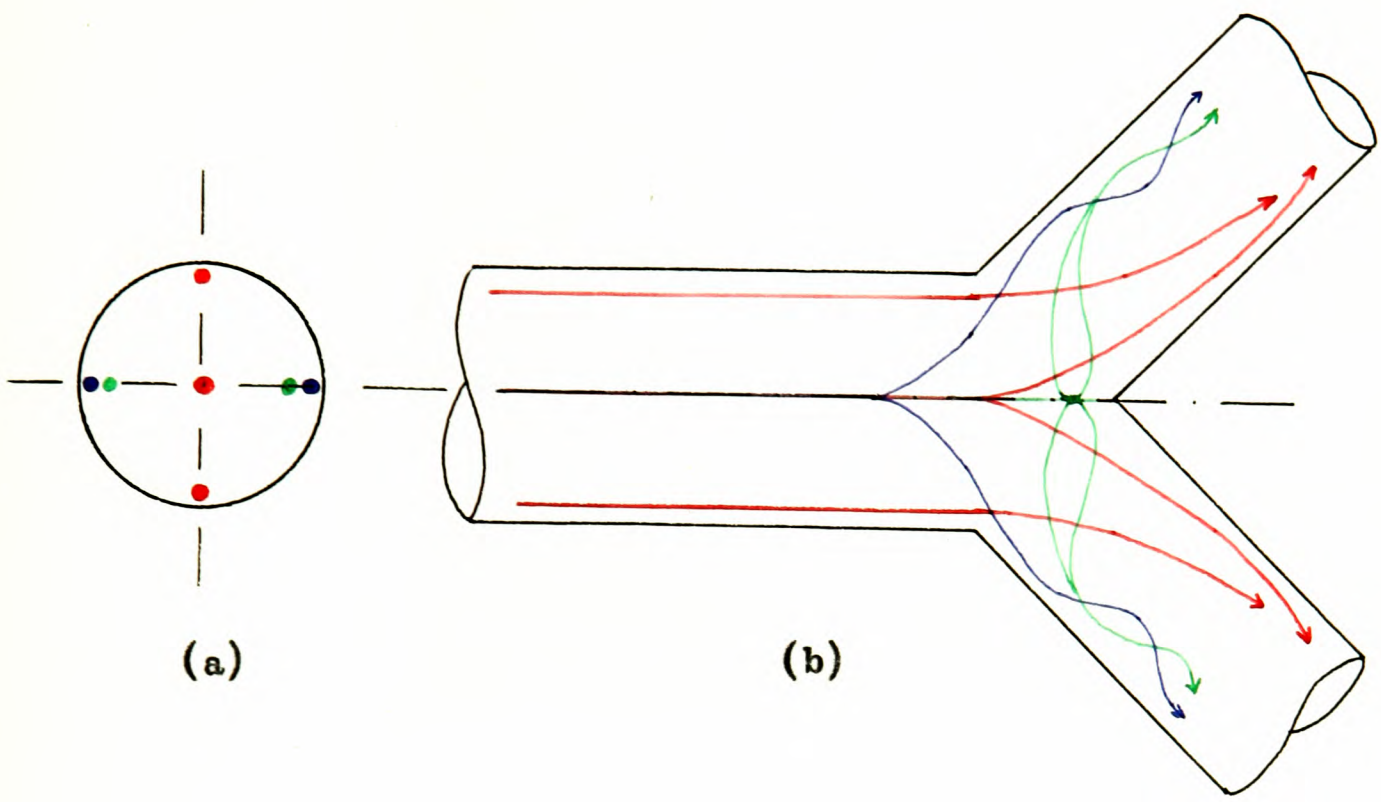
It was expected from the observations of section 4.1 that the initial secondary velocities should be proportional to the mean square velocity of the input. It was found that increasing the mean input velocity caused the formation of the initial vortex pattern on the outside of the branch to move nearer the branch carina and measurements were taken of this distance for each of several input flowrates. In the time taken for the axial flow to move this distance downstream, the secondary velocity had convected fluid across the diameter of the daughter tube. Thus an approximate measure of the relative magnitudes of secondary and axial velocities could be obtained. These values of secondary velocity were plotted against mean velocity squared, as shown in figure 4.7, and it was found

that they lay approximately on a straight line passing through the origin. This confirmed the dependence of secondary velocity on the mean square of inlet velocity.

It was further established that the overall features of the streamline pattern did not vary significantly with branch geometry and that the stability of the vortex pattern downstream decreased with increase of input velocity.

The detailed streamlines are shown diagrammatically in figure 4.8 overleaf and photographs of the streamlines in branch 2 are also shown in figures 4.9 and 4.10 following. It was found to be difficult to adjust the hypodermic needles to obtain dye streamlines exactly at the centre of the parent tube so that they would split, half going down each daughter tube. The photographs were therefore taken with the parent tube streamlines marginally off centre so that they would favour one limb. Thus all the streamlines could be photographed in one limb instead of some being in one limb and some in the other. The patterns were exactly the same in both limbs and the exact positions within the branch of the coloured streamlines shown in the photographs are indicated in the elevations. The descriptions and explanations which follow, however, refer to the diagram of the streamlines shown in figure 4.8.

With reference to figure 4.8, the central red line was the input centre streamline which divided as it approached the carina, was not affected by the cross-sectional shape change and continued down the inside wall of each limb until split up and convected round the tube



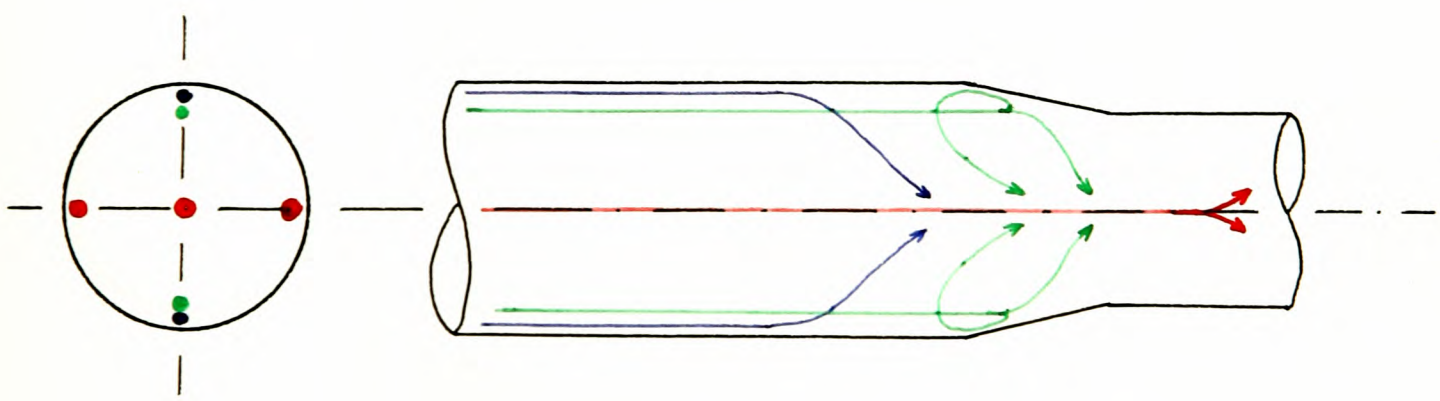
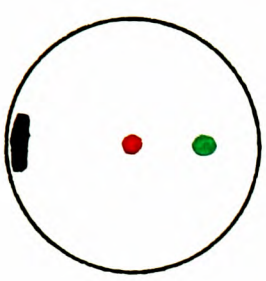
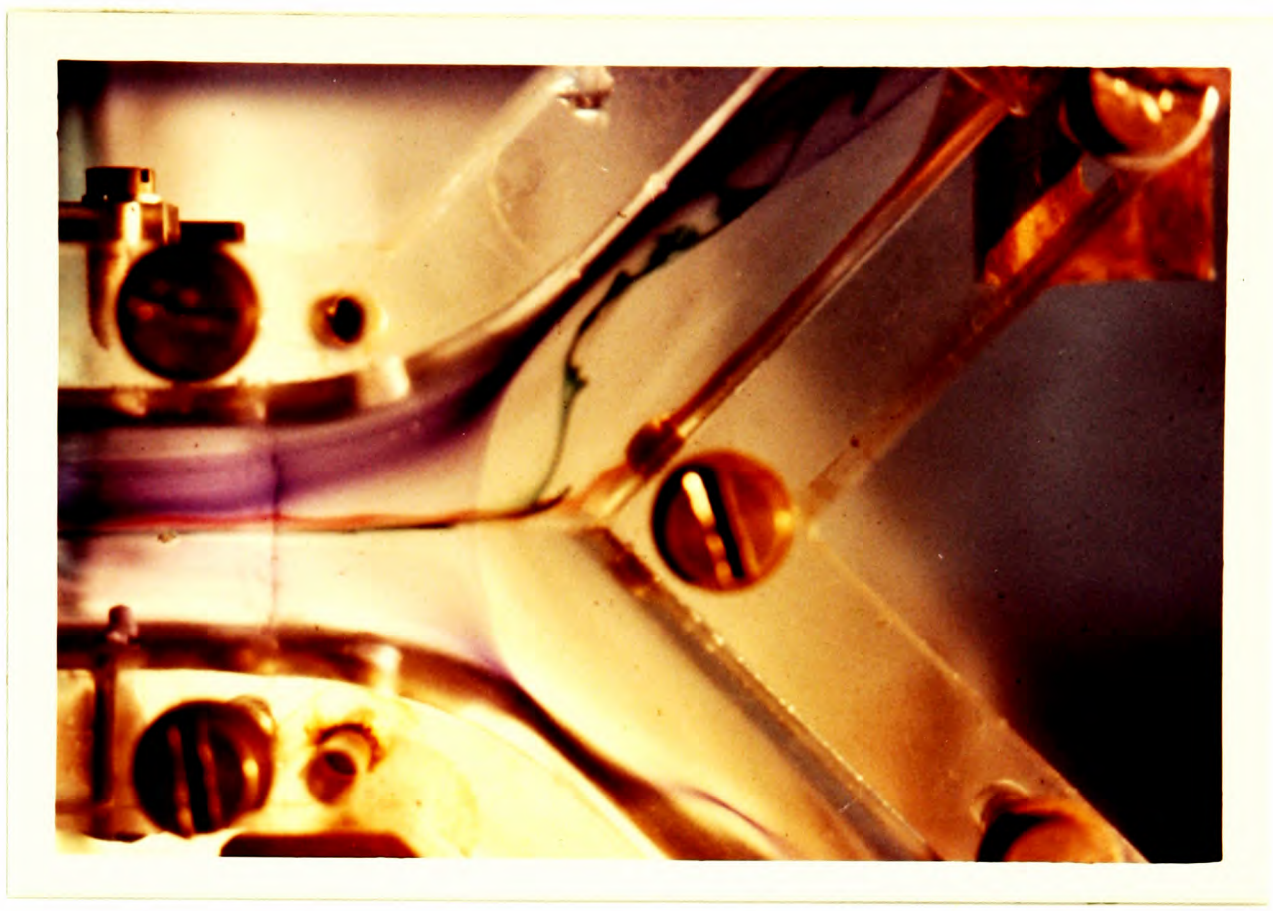
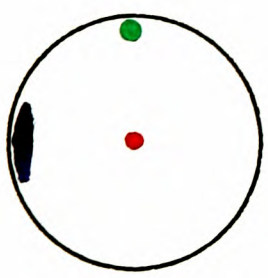
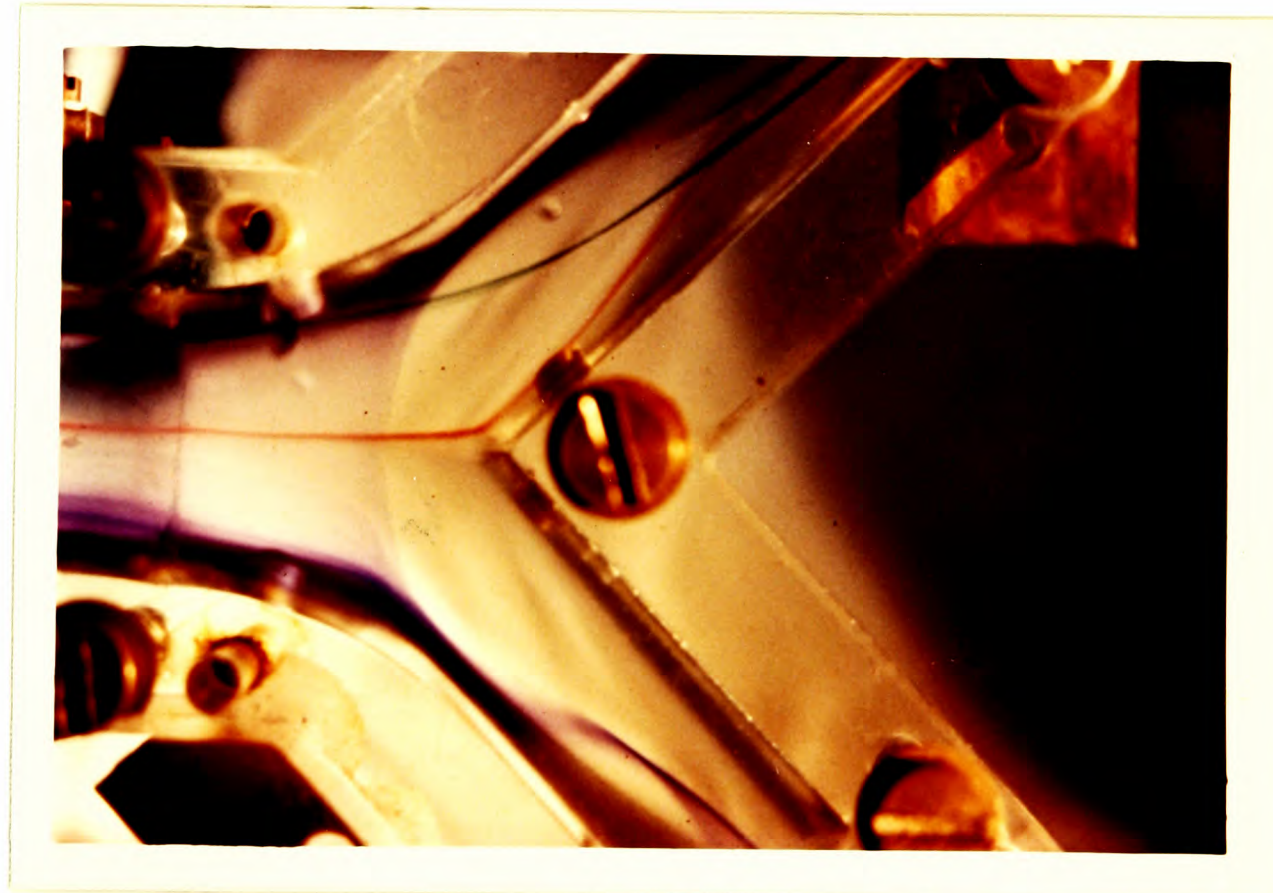


Figure 4.8. Diagram of streamlines in branch.









Figures 4.9 and 4.10. Streamlines in Branch 2.

by the action of the secondary vortices. The other red lines, which were near to the wall in the plane of the branch followed a similar pattern, moving towards the inside of the branch (the outside of the bend) under the action of its own momentum flux (centrifugal force). Note that the red streamlines were in the positions marked R in figure 4.6 and as pointed out above were not affected by the shape change but curved round into the limb leaving the areas on the outside of the branch for the fluid from top and bottom of the inlet. The green lines, which were the streamlines near but not at the top and bottom of the inlet tube approached quite closely to the carina and were then split up by impinging on the sloping ceiling and floor of the tube (see figure 4.8c), part bending back over and under itself and then moving across the top and bottom of the intersection and part moving directly across the top and bottom of the intersection, all joining up in a tight helix on the outside of each limb. The blue lines, which were the streamlines at the top and bottom of the inlet tube were unable to approach the carina closely owing to the reverse action of part of the faster-moving green lines and they were forced away across the top and bottom of the intersection to join up on the outside of each limb with the vortex formed by the green lines. The positions of the green and blue lines are marked as G and B in figure 4.6 and these were the streamlines affected markedly by the shape change.

It was not immediately apparent whether the vortex pattern was due in the main to the branch curvature or to

the cross-sectional shape change. Two further experiments were designed and carried out in an effort to separate the effects.

A straight branch was made up with a change in shape but with no curvature. This consisted of a 25 mm. diameter inlet and two 12 mm. diameter outlets, the axes of all three tubes being parallel. (See figure 4.11 below)

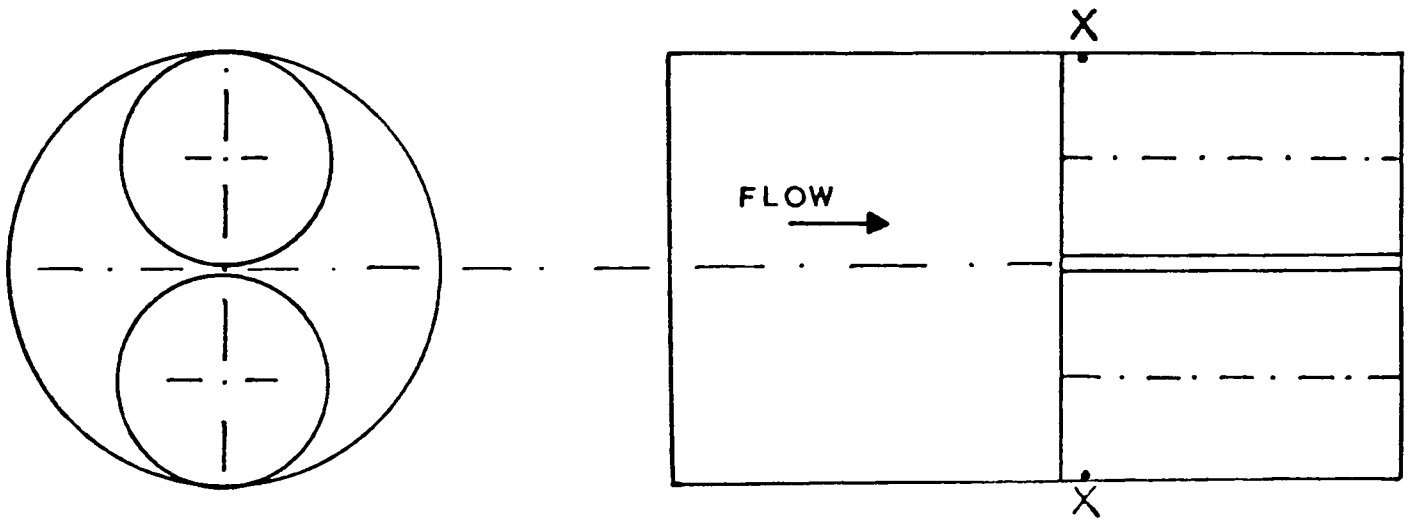


FIGURE 4.11 STRAIGHT BRANCH

Dye was injected near the top and bottom of the inlet and exactly the same patterns were observed as had been seen in the branches. Part of the streamlines near the top and bottom of the inlet turned back directly on themselves and then moved round the sides of the inlet to enter the outlet tubes near their outside walls. Similarly, streamlines actually at the top and bottom of the inlet tube were forced sideways before reaching the intersection by the reverse action of the streamlines next to them. Both sets of streamlines joined up on the outside wall (at points marked X in figure 4.11) but since the vortex was formed directly in the path of the main flow through

the outlet, it was dissipated almost immediately. The velocity through the limbs was substantially higher than in the inlet owing to the drop in cross-sectional area and purely axial flow was established in the outlet tubes within 3 to 4 mm. It had been shown, however, that a change in cross-sectional shape, similar to that in the experimental branches but with no curvature of the tube, caused a vortex pattern similar to that observed in the experimental branches.

A second experiment was carried out in a branch with sharp curvature but no shape change. This consisted of a 25 mm. diameter, 45° elbow (figure 4.12 below) with the cross-section split into two by a vertical strip placed at the start of the bend.

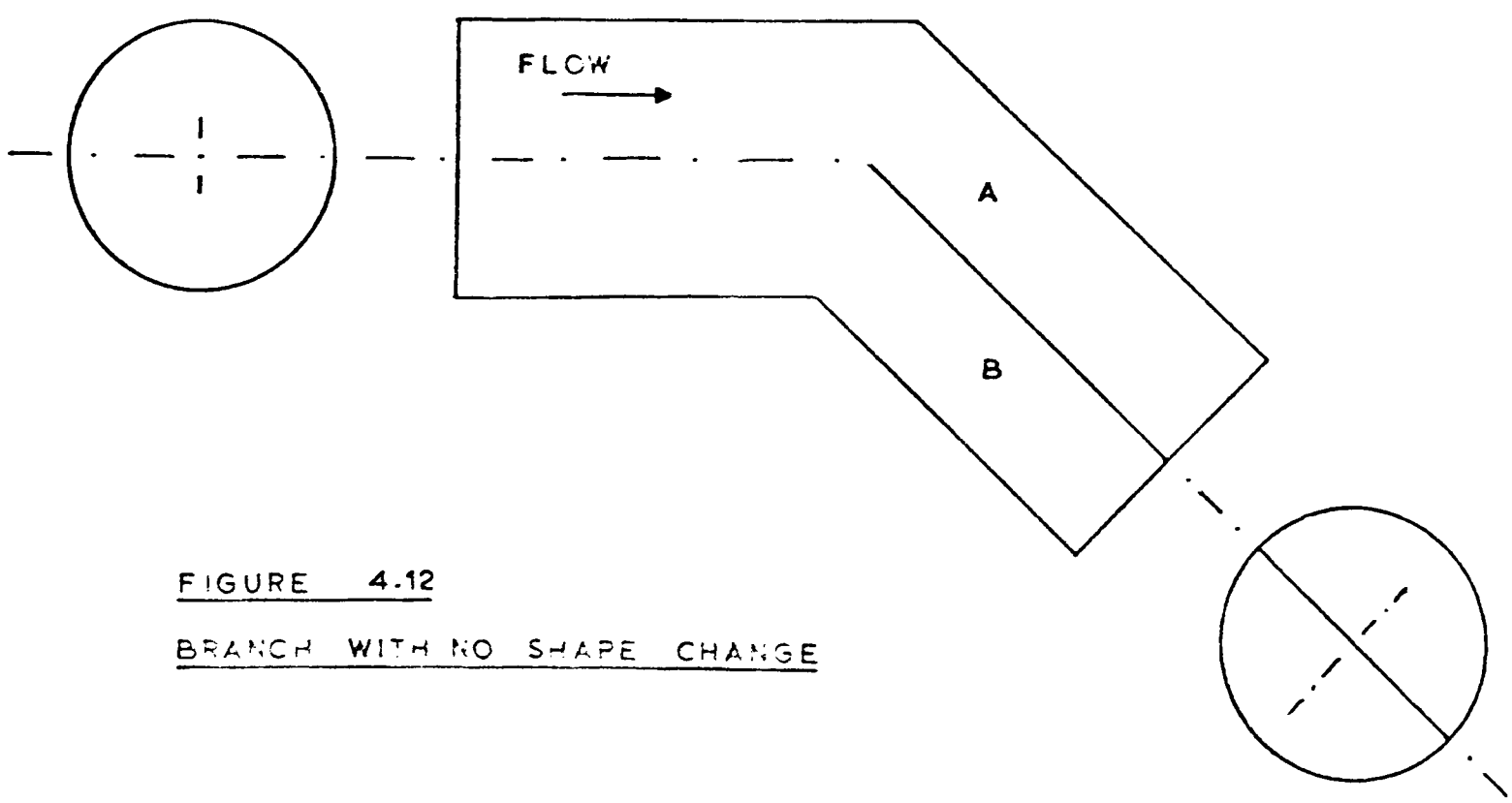


FIGURE 4.12

BRANCH WITH NO SHAPE CHANGE

Thus the inlet to limb B was similar to the inlet in the experimental branches 1 and 2 with the highest velocities close to the flow splitter. The cross-section of both inlet and outlet was the same, however, being 25 mm. diameter semi-circles. Dye was injected at points in the cross-section and once again the streamline pattern observed was very similar to the experimental branch observations though in this case there was no streamline turning back on itself.

It was thus demonstrated that sharp curvature with no cross-sectional shape change caused similar vortex patterns to a shape change with no curvature. Since the experimental branches were a combination of both cross-sectional shape change and sharp curvature, it was not possible to conclude from the above experiments which effect was dominant. The observation that the strength of the vortex pattern varied with the mean square velocity of the input also gave no indication as to the difference between the effects since curvature vortices are dependent on Σu^2 and shape change vortices are dependent on the change in momentum flux which is itself proportional to Σu^2. The fact that there was little difference between the vortex patterns in the two different branches, however, might suggest that shape change vortices were dominant. If curvature vortices were dominant, then the difference in radius of curvature between branches 1 and 2 (approximately threefold) should have an effect on the pattern. This was not evident from the dye studies though the

velocity profiles (section 7) showed a slight decrease of vorticity in branch 2 compared with branch 1. In both branches 1 and 2, however, the bend was short and sharp and curved streamlines were not fully established in either branch. Thus the concept of centrifugal forces proportional to radius of curvature is not valid and direct conclusions cannot be drawn.

Thus no definite distinction can be made between curvature and shape change vortices within the branch. Since both the bend and the change in cross-sectional shape are an integral part of the branch, the secondary vortices set up can be considered as a whole and it can be assumed that both curvature and shape change play a part in their formation.

4.3 Pulsatile Flow

In pulsatile flow, the accelerating pulse set up secondary flows in a similar manner to that described above, the strongest vortices being formed at the peak of the pulse. Towards the end of the pulse, however, backflow was observed on the outside of the limb for some 4 cm. downstream even though fluid on the inside of the limb was still moving forward, a two-way motion being set up within the limb. Thus the vortices on the outside of the limb moved only a short distance downstream during each pulse, the vortical motion from any one pulse being dissipated by the backward motion at the end of that pulse and the

acceleration at the beginning of the following pulse. The development of the flow patterns downstream was thus much more stable than in steady flow, the major part of the secondary motion being dissipated within a relatively short distance.

4.4 The Effect on the Streamline Pattern of Total Occlusion of one Limb

A study was made of the streamline pattern within the branch when one limb was totally occluded. Both steady and pulsatile flows were studied and comparisons were made with similar flows in a straight tube with an occluded limb. Dye was injected into the flow at different points across the stream upstream of the branch and note was taken of the observed streamline distribution within and around the occluded limb. The steady flow laminar streamlines are shown in figure 4.13 below for the symmetrical branch and in figure 4.14 below for the straight tube branch.

In the case of laminar steady flow in the straight tube branch, (Re = 1500) a very small quantity of fluid entered the occluded limb in the horizontal plane at the downstream end of the junction and left at top and bottom of the limb, setting up a very slow-moving vortex at the entrance to the occluded limb. Increasing the flowrate increased the strength of the vortex and a second slower-moving vortex was set up in the opposite direction further up the occluded limb. The streamline distribution in pulsatile flow was similar save that at the end of each pulse the vortex at the end of

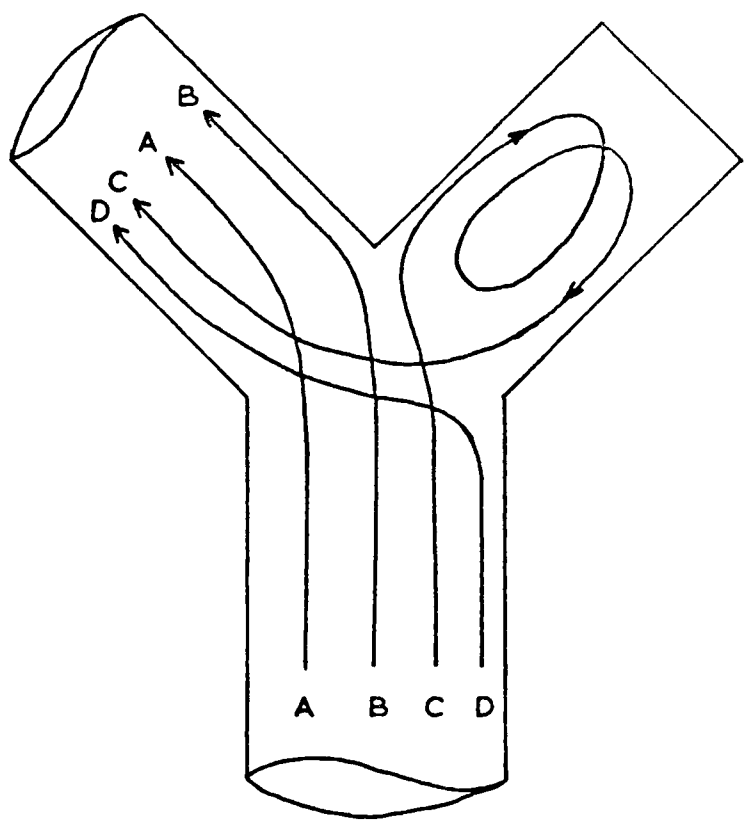


FIGURE 4.13

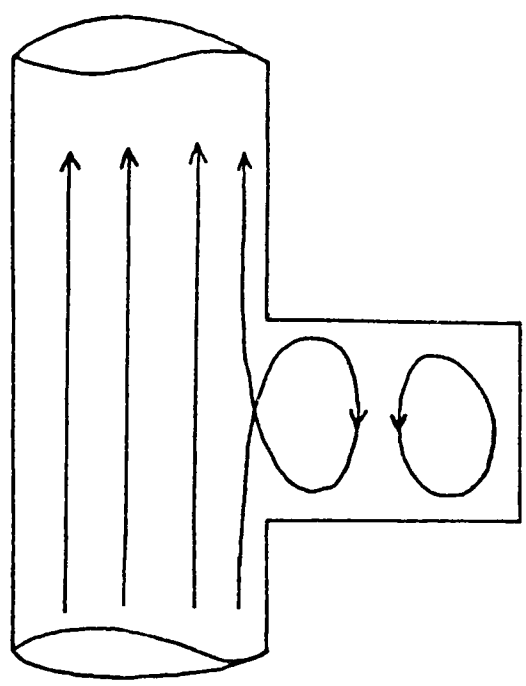


FIGURE 4.14

OCCLUSION OF ONE LIMB

the occluded limb was drawn slightly into the main stream with the result that the beginning of the following pulse, a small quantity of the fluid which had been within the occluded limb was carried downstream with the main flow. During the major part of the pulse, however, the streamline distribution was the same as in steady flow with very little interaction between the main flow and the occluded limb.

The situation that occurred in laminar steady flow in the symmetrical branch was more complex since fluid was continually entering and leaving the occluded limb.

The explanation of the streamline pattern observed and shown in figure 4.13 can be described by reference to the four streamlines A, B, C and D which are all in the plane of the branch. Note that with a parabolic input, D will be the slowest moving streamline and B the fastest. The main streamlines A and B bent round the branch and continued down the open daughter tube but they were translated towards the inside of the limb (the outside of the bend) by the action of the centrifugal forces described in section 4.1. Hence there was some critical streamline, C, which was forced into the occluded limb by this transverse action of the faster-moving streamlines A and B. Having entered the occluded limb, a slow-moving vortex was set up and streamline C emerged from the outside of the limb, split into two to cross over and under the faster-moving streamlines A and B and eventually linked up again near the outside of the open limb. Meanwhile, streamline D was unable to proceed into the occluded limb owing to the presence of the faster-moving outward stream, C, and was therefore forced to split, cross over and under streamline C and the main streamlines B and A and rejoin on the outside of the open limb. Secondary vortices were apparent in the open limb and these gave a double helical motion to the flow as it moved downstream. The path of streamlines C and D over the main stream can be seen in figure 3.2 by the trace of bubbles across the top of the tube. Although the limb in this photograph of switched

flow was not completely occluded, only 10% of the flow was passing down it and the effect on the flow pattern was similar to that shown in figure 4.13 for the totally occluded limb.

In pulsatile flow, the same patterns could be observed although there was more mixing of the fluid, particularly at the end of the pulse.

5. THE DESIGN OF A DIRECTIONALLY-SENSITIVE THIN-FILM VELOCITY PROBE

5.1 Introduction

The design, construction and calibration of thin-film velocity probes for the measurement of instantaneous velocity have been described by Bellhouse and Bellhouse (1968 and 1969b). These probes consist of a thin-film, platinum thermometer deposited onto a glass bead and cemented into a hypodermic needle. The thermometer is heated electrically to approximately 15°C. above ambient, this excess being known as the overheat, and is maintained at constant temperature by means of a feedback bridge arrangement of which the element forms one arm. (See figure 5.1 below).

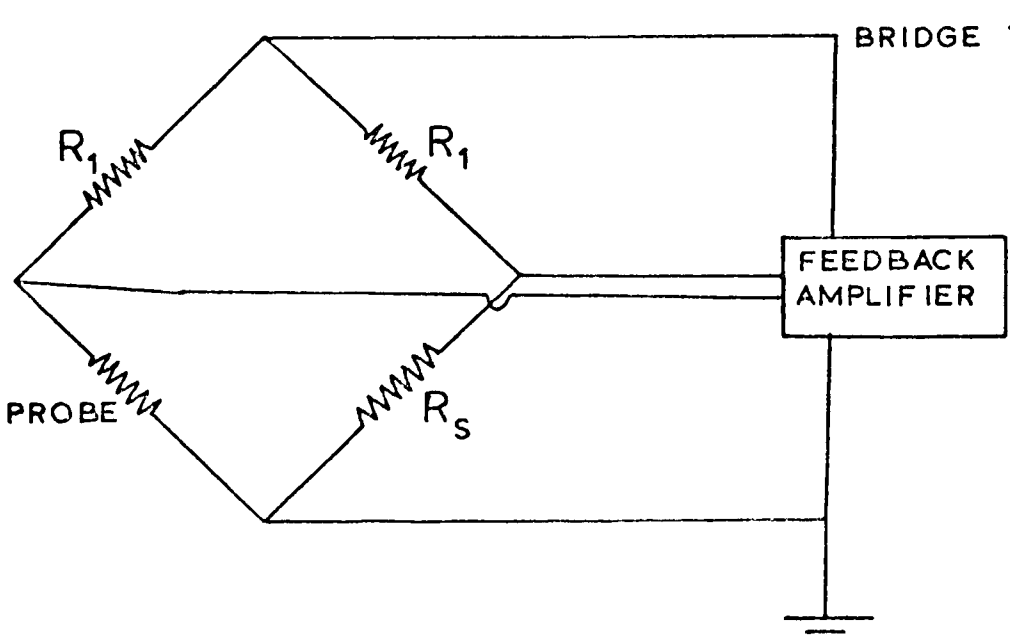


FIGURE 5.1

ANEMOMETER FEEDBACK BRIDGE

One of the other three arms of the bridge has a variable resistance, R_s, the other two remaining fixed. Since the temperature coefficient of resistance of the platinum element, β, is linear over the small range considered, i.e.

$$\beta = \frac{1}{R_o} \frac{\Delta R}{\Delta T} \qquad (5\text{-}1)$$

and since when the feedback bridge is in balance, R(probe)= R_s, the temperature overheat is uniquely determined by making the 'set' resistance, R_s, some suitable value above the probe 'cold' resistance, R_o. As β is approximately 2×10^{-3} per $^{o}C.$, an overheat of $15^{o}C$ is obtained by using a value of R_s such that $R_s = 1.03\ R_o$. Thus, having measured the resistance of the element, R_o, the value of R_s is set to $1.03\ R_o$ and the feedback bridge switched on. The heat convected away from the element by the fluid flow surrounding it is compensated for by the heat flowing in to the element from the power source and this is measured by monitoring the voltage required to keep the system balanced. If the fluid velocity increases, there will be an increase in the heat convected away from the element which will cause the element temperature and hence resistance to fall thus putting the bridge out of balance. This out-of-balance is monitored by the anemometer feedback system which increases the voltage at the bridge top to compensate, thus countering the tendency of the element temperature to fall by providing more heat to it. Thus as the bridge is always kept in balance, the element is always maintained at the 'set' resistance, R_s, and a

direct measure of the heat transfer is obtainable by monitoring the bridge-top voltage, V_b.

Solution of the viscous and thermal boundary layers over an exposed heated element yields the theoretical calibration (Bellhouse and Schultz, 1966)

$$\frac{i^2R}{\Delta T} = B\sqrt{u} + C \qquad (5\text{-}2)$$

where i and R are the current and resistance respectively, ΔT the difference between the film and fluid temperatures, u the velocity and B and C probe constants for a given medium.

Since $V_b = iR$ and $R = R_s$,

$$\frac{i^2R}{\Delta T} = \frac{V_b^2}{R_s \Delta T}$$

$$= \beta \frac{R_o V_b^2}{R_s \Delta R} \quad \text{from equation (5-1).}$$

Hence from equation (5-2),

$$\frac{\beta R_o V_b^2}{R_s \Delta R} = B\sqrt{u} + C$$

and if the overheat factor is kept constant, R_o/R_s is constant and so

$$\frac{V_b^2}{\Delta R} = b\sqrt{u} + c \qquad (5\text{-}3)$$

---

where b and c are constants. This is the final calibration equation for the probe and b and c are found from calibrations against known velocities.

When $u = 0$, $c = V_o^2 / \Delta R$ where V_o is the bridge-top voltage required at zero flow and hence:

$$\frac{V_b^2}{\Delta R} - \frac{V_o^2}{\Delta R} = b\sqrt{u} \qquad (5\text{-}4)$$

V_o will not be zero since, even at zero flow, there is a certain amount of natural convection and conduction away from the probe. Equation (5-4) can be used for calibration purposes in place of equation (5-3) but measurements of V_o are not as consistent as measurements of V_b in non-zero, steady velocities and it is recommended that equation (5-3) be used on account of its greater accuracy. Further details of the manufacture, calibration and use of thin film velocity probes and discussion of many of the associated problems can be found in Pope's (1971) work on the subject.

Previous designs of probe have been relatively insensitive to the direction of velocity and have therefore only been of use in flows where the velocity is uni-directional. As already discussed, the flow patterns downstream of branches are complex and the velocities not unidirectional. In order to measure the axial velocity plots downstream of the branch, some device was required that would measure only the velocity or component of velocity in one direction.

5.2 The Directionally-Sensitive Probe

In order to obtain screening from all but axial velocities, the platinum element was housed within a protective sleeve which would certainly protect the element from transverse velocities and which was expected would

read the component of velocity in the direction of the sleeve axis. The design is shown in figure 5.2 below which has been reproduced from Brech et al. (1971).

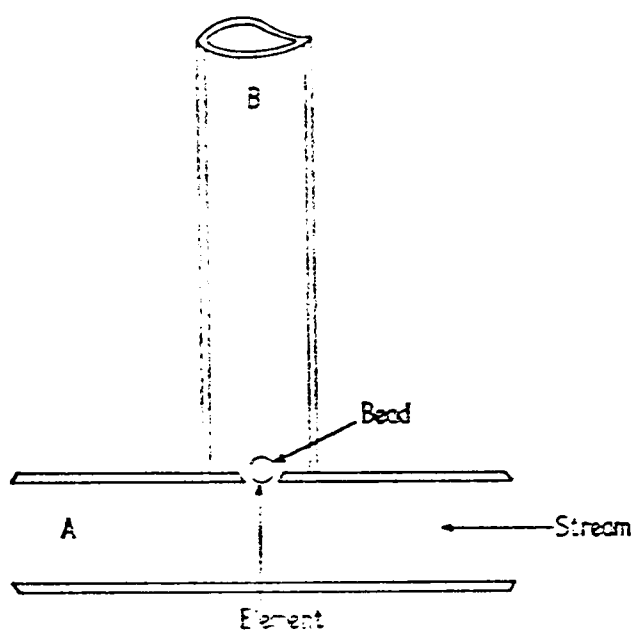


FIGURE 5.2

THE DIRECTIONALLY-SENSITIVE VELOCITY PROBE

The glass bead, 0.5 mm. in diameter, with the element painted and fused onto it was mounted within a thin-walled, stainless steel tube, 10 mm. long and of 1.5 mm. bore. (A in figure 5.2). The tube A was supported in the stream by means of a second similar tube, B, passing through the vessel wall, and the spherical glass bead was inserted into the joint between the two tubes so that the element was perpendicular to the axis of tube A and flush with the wall. The joint and bead were then sealed with Araldite and the wires to the element fed out through the supporting tube, B, to a BNC connector. The feedback bridge unit used was a DISA 55D01 anemometer unit and this was connected to a Dynamco 2022 digital voltmeter which had a facility for parallel output of the voltage reading.

5.3 Experimental Tests

The angle of the probe to the oncoming stream, θ, was varied in one plane by twisting the supporting tube. Measurements of velocity against angle were taken in the centre of a uniform, flat, laminar flow in 25.4 mm. pipe for angles varying from 0° to 90° in 10° steps and for steady velocities of 7.4, 9.8 and 14.9 cm./sec. Figure 5.3 shows the results obtained. The velocities, normalised with respect to the free stream velocity are plotted against angle and the extent of the scatter is shown. A cosine curve (broken line) is also plotted for comparative purposes.

There was no significant difference between the results obtained at the three different flowrates and for θ in the range 0° to 60° the velocity recorded was nowhere more than 10% from the value of the cosine component, even though the curve remained flat for the first 15°. When the probe was nearly at right angles to the flow direction, measurements were less reliable probably because of secondary flows caused by the probe. For the purposes for which it was required, however, which was to measure the velocity or component of velocity in the axial direction and to exclude the smaller transverse velocities, the probe was quite suitable.

This probe can also be used as a device for accurate measurement of velocity direction by using the following procedure. The probe is first rotated to within $\pm$ 15°

of the velocity direction, where the calibration curve, figure 5.3, is flat and the velocity measured. This will be the maximum reading of the probe. The probe is then rotated through a known angle, say 45^{o}, to where the calibration curve is most sensitive, and the component of velocity measured. The ratio of this component of velocity to the maximum velocity gives from figure 5.3 the angle of the velocity to the probe in its latter position to within three degrees.

An investigation was made into the behaviour of probes with higher aspect ratios (length of sleeve divided by diameter) in order to reduce the angle over which the calibration curve was flat and so increase the sensitivity of the instrument. The aspect ratio of the original probe was $6\frac{2}{3}$ (10 divided by $1\frac{1}{2}$) and this was increased by adding sleeving to each end to give aspect ratios of 13 and 21. No significant difference could be observed in the results for either case and there was no difference between the cases of the extra sleeving being all in front of the probe or all behind. In all cases, the same flat region of approximately 15^{o} persisted.

5.4 Calibration and Use of Probe

Before using the probe to measure the axial velocity profiles it was necessary to calibrate it against known velocities in order to confirm that its operating characteristics were in accordance with equation (5-3) above. Also, since the values of the constants could vary slightly

from day to day, as was also pointed out by Pope (1971), it was necessary to develop a technique for calibration within the experimental rig before and after each experiment since a towing tank was not readily available. These slight variations in the calibration constants could possibly be due to small deposits on the element or to small variations in temperature measurement and overheat factor.

The probe was first calibrated in a towing tank for velocities from 4.8 cm./sec., the lowest obtainable, up to 38 cm./sec. Velocities were measured by means of an electronic timing device activated by the passage of the probe holder past two switches one metre apart. Values of R_0, R_s and V_b were measured for each run and the calculated values of $V_b^2/\Delta R$ were plotted against $\sqrt{u}$. This graph gave a straight line up to a velocity of 23 cm./sec. when it began to curve off. Below 23 cm./sec. and above 4.8 cm./sec., however, equation (5-3) was confirmed.

Experimental calibration in the rig was performed in the centre of the 25.4 mm. pipe 23 cm. downstream of the conical inlet section where the central portion of the profile was still fairly flat. Possible small differences in the positioning of the probe would thus give no error in indicated velocity. It was necessary however to find the value of the central flat velocity compared with the mean velocity, the latter being easily calculated by means of a flowrate measurement.

A hooked probe (Bellhouse and Bellhouse 1968), which obeyed equation (5-4) right down to zero, was traversed

across the calibration section at a distance of 23 cm. downstream of the end of the conical section and a series of values of (V_b^2 / ΔR - V_o^2 / ΔR) was obtained for each of eight flowrates. For each flowrate, the following procedure was adopted. The maximum value of ($V_b^2/\Delta R$ - $V_o^2/\Delta R$) was found i.e. at the centre of the stream, and thus the value of $b\sqrt{u}_{max}$ was found. (Equation (5-4)). The other values of $b\sqrt{u}$ were then expressed as a fraction of this maximum value to give a series of values of $\sqrt{u/u_{max}}$. Squaring these results, the values of u/u_{max} were plotted against position to give a relative velocity profile. $\Sigma(A_i u_i/u_{max})$ was then found graphically by taking an average value of u/u_{max} for each of several circular annuli, working out from the centre, multiplying this value by the area of the annulus, A_i, and summing the results. Since the flowrate, $Q = A\bar{u} = \Sigma A_i u_i$, then

$$\frac{u_{max}}{\bar{u}} = \frac{A}{\Sigma A_i u_i / u_{max}}$$

and the value of $u_{max}/\bar{u}$ was found by dividing the cross-sectional area of the tube by the calculated value of $\Sigma A_i u_i/u_{max}$. These values of $u_{max}/\bar{u}$ are plotted in figure 5.4.

Theoretical Considerations

Langhaar (1942) has worked from the Navier Stokes equations to obtain the following relation for the calculation of the complete laminar velocity profile in the inlet section of a tube:

$$\frac{u}{\bar{u}} = \frac{I_0(\phi(z)) - I_0(\phi(z).\ r/a)}{I_2(\phi(z))}$$

where u is the velocity at radius r, $\bar{u}$ the mean velocity, a the tube radius, z the distance downstream from entry, I_0 and I_2 are modified Bessel functions of the first kind and $\phi(z)$ is a particular function of z. A table of values and a plot of $\phi(z)$ against $\frac{z/2a}{Re}$ can be found in Knudson and Katz (1958) p.229.

Langhaar's equation above is valid for sharp-entranced tubes and tubes provided with short bell-shaped mouths and it is assumed that the conical section leading into the experimental tube in this case falls into the latter category.

Putting r = 0 in Langhaar's equation in order to obtain u_{max} gives:

$$\frac{u_{max}}{\bar{u}} = \frac{I_0(\phi(z)) - I_0(0)}{I_2(\phi(z))}$$

In the experimental case, z = 23 cm., Re = 254 $\bar{u}$ and 2a = 2.54 cm. Hence $\frac{z/2a}{Re} = 0.0357/\bar{u}$. Table 5.1 shows the calculation of values of $u_{max}/\bar{u}$ for various values of $\bar{u}$, the values of $\phi(z)$ being found from Knudson and Katz (1958) and I_0 and I_2 from standard tables of Bessel functions.

$\bar{u}$	z/2aRe	$\phi(z)$	$I_0(\phi(z))$	$I_2(\phi(z))$	$u_{max}/\bar{u}$
2	0.0178	2.5	3.29	1.28	1.79
5	0.00714	4.4	16.0	9.63	1.56
10	0.00357	6.0	67.2	46.8	1.41
20	0.00178	8.7	824	646	1.27
50	0.000714	12.6	33,700	28,500	1.18
80	0.000446	15.9	811,000	712,000	1.14

Table 5.1.

Finally, figure 5.4 shows the theoretical plot of u_{max} against $\bar{u}$, together with the experimental points calculated as above. Figure 5.4 is in two parts, one for velocities below 10 cm./sec. and one for higher velocities. It can be seen that the correlation between theory and experiment is excellent.

Thus for any flowrate, the centreline velocity in the calibration section could be read off directly from figure 5.4 once the mean velocity was found. These values of velocity were the ones used for calibration purposes.

Having found the calibration velocities, the directionally-sensitive probe was inserted into the calibration section and calibrated for V_b^2/R against velocity. A typical but not a best calibration curve is shown in figure 5.5. Five calibrations were carried out throughout the day and the amount of scatter is shown by the error bars. This shows that the probe was consistent during the day to within 5% in velocity for the range $4<u<20$ cm./sec. and to within 15% in velocity for the range $1<u<4$ cm./sec. Above 20 cm./sec., the flattening of the calibration curve meant that errors could rise to the order of 20% to 25% in velocity.

The calibration formed a straight line satisfying equation (5-3) for the range $1.5<u<20$ cm./sec. and this agreed with the towing tank experiments. Above 20 cm./sec. the graph began to curve off somewhat, this again agreeing with the towing tank observations. Below 1.5 cm./sec. there was a very rapid flattening to the zero flow condition which meant that the probe was not sensitive to velocities

below 1.5 cm./sec. This is explained in section 5.5 below.

For use in the automatic processing of probe data (see sections 6.2 and 7.2), the calibration curve was divided into two sections. Above the value of 1.5 cm./sec. a straight line equation was used as in equation (5-3). Below this value, a parabolic curve of the form $V_b^2/\Delta R = F\ (\sqrt{u})^2 + G$ was fitted to the experimental calibration points. Velocities above 20 cm./sec. were not used in the branch so no further equations were required. The values of b, c, F and G found from the calibration curve were used directly in the computer program data tapes and were known as the calibration constants.

Dynamic calibration of the probe was also carried out in the rig. A pulsating sinewave of zero mean flowrate was used and the voltage output was recorded by means of a Sanborn 322 chart recorder. The theoretical waveform was obtained from Womersly's (1955) work and the experimental calibration was plotted onto a graph of this waveform as shown in figure 5.6. The experimental calibrations gave a sinewave which showed excellent correlation with the theory, the maximum error being only 6%. The amplitude of the pressure gradient was 57.5 cm./sec.^{2} (a piston amplitude of 1.27 cm. acting through an area increase of 17.0 at a frequency of 0.26 Hz.), nearly four times as great as that used in the pulsatile flow studies carried out with the probe.

The probe was also tested at higher values of frequency at a piston amplitude of 0.08 cm. The compliance in the pipes feeding the settling chamber was such, however, that

the pulse amplitude in the main pipe section fell off rapidly with frequency and it was not possible to test the probe accurately against theoretical predictions. Nevertheless, regular and consistent pulse-shaped variations in probe voltage were found for frequencies up to 10 Hz., the maximum obtainable in the rig, and when the probe was used in turbulent flow, fluctuations of the order of a kilocycle were observed.

5.5 Analysis of Probe Behaviour

The heated element within the probe tube reads the velocity within the probe tube, u_e. Since this tube is very narrow, the velocity profile within the probe tube level with the element will be more than 85% developed for all calibration velocities up to 20 cm./sec. (Langhaar, 1942). Thus, since the universal calibration for a heated element (Bellhouse and Schultz, 1966) is:

$$\frac{V_b^2}{\Delta R} = B + C\,\tau^{1/3} \qquad (5\text{-}5)$$

where τ is the shear stress and B and C are constants, and since for developed pipe flow, τ is proportional to velocity, then

$$\frac{V_b^2}{\Delta R} = B + Cu_e^{1/3} \qquad (5\text{-}6)$$

If u_e can be calculated from the local stream velocity, then equation (5-6) should hold and a plot of $V_b^2/\Delta R$ against $u_e^{1/3}$ should yield a straight line.

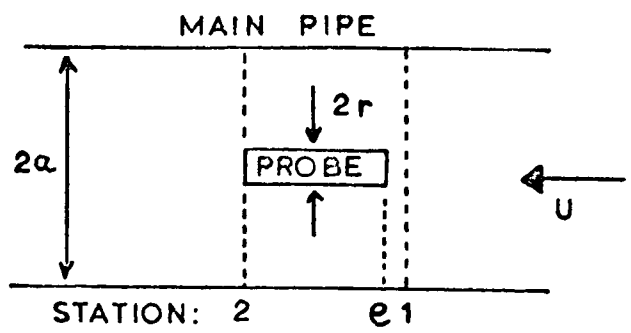


FIGURE 5.7
NOTATION

Referring to figure 5.7 above and defining the mean stream velocity by $\bar{u}$, the local stream velocity in line with the probe by u and the mean velocity in the probe tube by u_e, the application of Bernouilli's equation between stations 1 and e gives:

$$P_1 + \tfrac{1}{2}\rho u^2 = P_e + \tfrac{1}{2}\rho u_e^2$$

Poiseuille's equation for the main pipe gives:

$$P_1 - P_2 = \frac{8\ell\mu\,\bar{u}}{a^2}$$

Since for calibration velocities less than 15 cm./sec., the velocity profile in the probe tube will be more than 80% developed within the first 10% of its length (Langhaar, 1942), Poiseuille's equation can be used as an approximation within the probe tube to give:

$$P_e - P_2 = \frac{8\ell\mu u_e}{r^2}$$

where a is the main pipe radius and r the probe tube radius.

Eliminating P_1, P_2 and P_e,

$$\frac{8\ell\mu u_e}{r^2} = \frac{8\ell\mu\bar{u}}{a^2} + \tfrac{1}{2}\rho(u^2 - u_e^2)$$

In this case, ℓ = 1 cm., μ = 0.01 gm./cm./sec., r = 0.075 cm., a = 1.27 cm. and ρ = 1 gm./cm.^{3} Hence,

$$3.56\ u_e = 0.0496\ \bar{u} + 0.5\ (u^2 - u_e^2)$$

which yields

$$u_e^2 + 28.48\ u_e = 0.099\ \bar{u} + u^2 \qquad (5\text{-}7)$$

Table 5.2 gives the values of u_e calculated from equation (5-7) for various values of u and includes the values of $V_b^2/\Delta R$ found when calibrating against the velocity u. (The relation between u and $\bar{u}$ in the calibration section is found from figure 5.4).

u	cm./sec.	0	1.55	5.2	7.4	14.9	21.5	33.4	46.5
$\bar{u}$	cm./sec.	0	0.81	3.1	4.7	11.0	16.9	27.5	40.0
u_e	cm./sec.	0	0.085	0.93	1.82	6.40	11.6	22.1	34.4
$V_b^2/\Delta R$	watts	15.17	15.86	17.18	17.75	19.22	20.10	20.80	21.15

Table 5.2.

A graph of $V_b^2/\Delta R$ against $u_e^{1/3}$ was then drawn, as shown in figure 5.8, and this yielded a straight line in accordance with equation (5-6) up to a velocity of around 20 cm./sec. when a slight curving off was still evident. At this speed, however, flow within the probe tube would be less than 85% developed and this would begin to invalidate the theoretical approach. For velocities up to 20 cm./sec., however, the heated element calibrated directly with the velocity in the probe tube according to the universal calibration equation expressed in equation (5-5). The velocity in the probe tube did not, however, bear a linear relationship to the local stream velocity but varied according to equation (5-7). This accounted for the shape of the calibration curve of $V_b^2/\Delta R$ against $\sqrt{u}$ (figure 5.5), the initial flat portion being due to the very small change occurring in u_e for u in the range $0<u<1.5$ cm./sec.

The operating characteristics of the directionally-sensitive probe were further investigated by traversing across a parabolic profile from both sides of the tube and comparing the results. This showed that the velocity recorded by the element was the velocity in a position 1.25 mm. from the far wall of the probe sleeve tube as shown in figure 5.9 below.

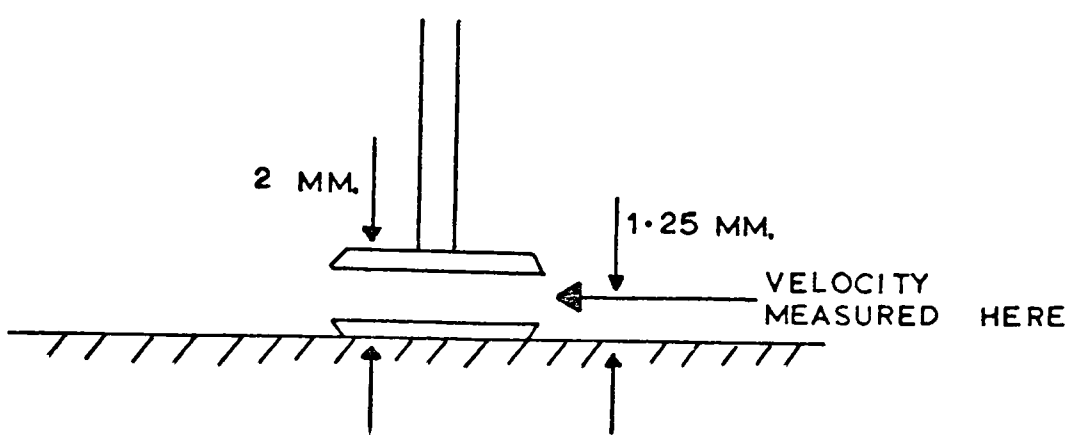


FIGURE 5·9

POSITION OF MEASURED VELOCITY

This position was slightly off the tube centreline, the probable cause being that steep velocity gradients at inlet to the probe tube were not being completely flattened by the time they passed the element. Taking the velocity at this position, however, eradicated any effects of inlet velocity gradient and the probe gave the same profile independent of the direction of traverse. When the probe tube was against a pipe wall, the velocity recorded by the element was thus that velocity at a distance 1.25 mm. from the pipe wall and this meant that the probe was limited in how closely to a wall it could measure velocities.

5.6 Summary

A thin film velocity probe has been designed for the measurement of axial velocity in complex flow situations. Transverse velocities are excluded and, provided the probe is aligned to within $\pm$ 60° of the main stream velocity, the axial component of the stream velocity is measured with a maximum error of 10%. The probe can also be used to measure the direction of velocity. Calibration of the probe is easy and consistent and is independent of the velocity gradient at inlet to the probe tube. Dynamic calibrations show that the probe is sensitive to velocity changes of the order of 50 cm./sec./sec. and there are indications that the probe also responds to higher frequencies although the sensitivity may be much reduced. Owing to the narrow bore of the probe tube, however, which is essential for accurate measurements, the probe is insensitive to velocities below 1.5 cm./sec.

6. THE VELOCITY DISTRIBUTION DOWNSTREAM OF BRANCHES IN STEADY FLOW

6.1 Introduction and Apparatus

The detailed flow patterns immediately within the branch were discussed in section 4 and it was found there that two pairs of helical secondary vortices were set up within the main flow. This section is concerned with the effect of these secondary flows on the development of the downstream flow and this has been investigated by plotting the distribution of axial velocity for several cross-sections and producing a velocity contour map, termed a velocity plot, for each of several positions downstream.

Careful setting up of the downstream conditions was necessary in order to ensure that the pressures and flows in each limb were identical. Exactly the same lengths of both 19 mm. and 25 mm. diameter tubes were used downstream of the branch in the same configurations and the flow from both limbs was fed to the same head tank, thus automatically equalising the downstream heads and obviating any small pressure disturbances such as have been described in section 3. A directionally-sensitive thin film velocity probe, as described in section 5, was used to measure the axial velocities.

The thin film probe was fitted into a special pipe section which formed part of one of the 19 mm. diameter daughter tubes of the branch and which allowed movement of the probe to any part of the cross-section by means of

a combination of rotation of the section and traverse of the probe. This working section is shown in figure 6.1. It consisted of a Perspex block in two halves, secured by screws and enclosing a 19 mm. diameter pipe section, which was fitted onto one of the branch daughter tubes. A holder for the probe and traversing mechanism was screwed to one side of the block and the probe projected through into the pipe section. The probe was gripped within a small Perspex clamp and transverse movement of the probe was controlled by a micrometer head acting on this clamp against the action of a compression spring. Rotation of the section was achieved by slackening the block securing screws, rotating the section to the desired angular position and retightening the screws. This could be done when the pipe was full of water. The working section could be positioned at any distance downstream of the branch by altering the length of 19 mm. diameter tube between the section and the branch.

6.2 Measurement, Computation and Presentation of Results

The velocity distribution was investigated at each of several positions downstream at three different flow-rates and in each case the input profile to the branch was laminar and parabolic. For the sake of continuity, all downstream measurements were taken in the same limb, limb B, but checks were made in the other limb from time to time and in all cases the velocity pattern was similar in both limbs. The three flowrates investigated were

31.0, 15.5 and 7.75 ml./sec. for the inlet flow (Inlet Reynolds' Numbers of 1550, 780 and 390 respectively) and these are referred to as High, Low and Very Low flows respectively.

Values of flowrate, Reynolds' Number and mean velocity in both the inlet and daughter tubes for the flows considered are shown in table 6.1 below.

	High Flow	Low Flow	Very Low Flow
Inlet flowrate: ml./sec. :	31.0	15.5	7.8
Inlet Reynolds' Number :	1550	780	390
Inlet mean velocity:cm./sec:	6.1	3.1	1.5
Limb flowrate: ml./sec. :	15.5	7.8	3.9
Limb Reynolds' Number :	1040	520	260
Limb mean velocity:cm./sec.:	5.5	2.7	1.4

Table 6.1.

Measurements of the velocity distribution downstream of branch 1 were taken at 3, 7, 11, 15, 23, 31, 47 and 63 cm. downstream of the carina for high flow, at 3, 7, 11, 15, 23, 31 and 47 cm. downstream of the carina for low flow and at 3, 7, 11, and 15 cm. downstream of the carina for very low flow. The measurements in branch 2 were taken at 7, 11 and 15 cm. downstream of the carina for both high (31.6 ml./sec.) and low (15.9 ml./sec.) flows. For each experiment, being defined as an investigation into the velocity distribution and the drawing of a velocity plot at one position downstream for one flowrate in one branch,

the following experimental procedure was adopted.

The working section was first of all rotated to the horizontal position and the probe was traversed across the cross-section, measurements of probe resistance, set resistance and anemometer voltage being taken at twelve different positions across the traverse at 1¼, 2¾, 4¼, 5¾, 7¼, 8¾, 10¼, 11¾, 13¼, 14¾, 16¼ and 17 mm. from the inside wall of the tube. The working section was then rotated by 22½° and the traverse measurements repeated. Further sets of twelve traverse measurements were taken at angles of 45°, 67½°, 90°, 157½°, 135° and 112½° to the horizontal, giving measurements at a total of 96 points within the cross-section. (Twelve traverse positions in each of eight angular traverses). This set of measurements at the 96 points was then completely repeated, working backwards from 112½° to 0° so that a mean could be taken which would help eradicate any small, time-varying discrepancies in flowrate or probe behaviour. The probe was calibrated before and after each experiment, as described in section 5, a mean taken and the calibration constants calculated. The total flowrate was also measured at the beginning and end of each experiment. If there was any significant difference between the probe calibrations or flowrates as calculated at the beginning and end of each experiment, the experimental results were discarded and the experiment repeated.

For each experiment, the values of ΔR (set resistance minus probe resistance) and anemometer voltage at each position were fed into the Oxford University English Electric

KDF9 computer together with a set of identification data and calibration constants. Using an Algol program, similar though slightly simpler than that used for pulsatile flow processing shown in Appendix 1 and explained in section 7.2, the velocity at each position for each of the two sets of readings was calculated from the calibration equations using the computed values of $V_b^2/\Delta R$ and the calibration constants provided. (See section 5.4). These velocities were labelled V(j,k,ℓ) where j (1-12) was the position in the traverse, ℓ(1-8) the traverse number and k (1-2) the particular set of readings. Thus V (3,1,2) would be the velocity recorded the first time at position 4¼ mm. from the wall in the traverse at 22½°. The centreline velocity of each traverse, M(ℓ,k) was then interpolated from the values of velocity at the positions 8¾ mm. and 10¼ mm. from the pipe wall, the centreline being 9½ mm. from the wall. The mean value of all sixteen M(ℓ,k) was then found and termed M(9,O) and the correction factor of M(9,O)/M(ℓ,k) applied to the velocities in each traverse. This was to refer all velocities to the same mean centreline velocity. An error calculation was then brought into action which calculated the percentage error between the two values of velocity at each position, V(j,1,ℓ) and V(j,2,ℓ), for all j and ℓ(96 values). Finally a mean of V(j,1,ℓ) and V(j,2,ℓ) was taken to give a final, corrected value of velocity at each of the 96 points in the cross-section. These values of velocity were then used in the graphical and numerical presentation of results which followed.

The facility of an English Electric graphical output system linked to the KDF9 gave the opportunity of having results output in direct, graphical form. This was achieved in two ways, a direct plot of velocity against position for each traverse, an example of which is shown in figure 6.2, and an overall velocity map or plot of the cross-section for each experiment. The graphs of velocity against position in the traverse were accomplished by using the graph plotter routines to plot the velocities found as above in their correct positions and draw a curve to pass through them all. Since the curve drawing routine operated by fitting cubics through sets of three points, it was necessary to insert dummy points near zero at each end of the traverse in order to ensure correct plotting. The overall velocity plots were achieved by selecting various set velocities, which were to be the contours, and using linear interpolation between the velocities at adjacent positions in each traverse and parabolic interpolation between the velocity at the end position and zero in each traverse to discover if and where the set velocities occurred within each traverse. The positions of these set velocities, thus found, were then plotted onto a plan of the cross-section, using a different plotting character for each set velocity and these characters were then joined up manually to give a set of lines of constant velocity or isovels. Further details of the computer processing are given in section 7.2.

Thus for each experiment a complete velocity contour map was produced. In the case of high flows, the contours

presented lines of constant velocity from 4 cm./sec. in steps of 1 cm./sec. to 11 cm./sec., the maximum integer value recorded. For low flows, they ran from 2 cm./sec. in steps of 0.5 cm./sec. to 5.5 cm./sec. and for very low flows from 1 cm./sec. in steps of 0.25 cm./sec. to 2.75 cm./sec. Occasionally an extra contour was drawn in manually from the values of velocity output on the lineprinter if it was felt that this would be an aid to visual comprehension of the plot.

6.3 Errors

The calculations of the percentage differences between the two separate sets of data recorded for each experiment in both high and low flows showed that an excellent degree of consistency was present and that the calculated velocities could in general be relied upon as accurate. 80% of readings were within 5% of each other, 93% were within 10% of each other and 97% within 15% of each other. The errors greater than 10% were usually found in positions where the velocity gradient was high and where a small error in probe positioning could lead to a large error in velocity.

For the very low flow experiments, the percentage errors tended to be marginally larger. This was to be expected since even a very small velocity differential becomes a significant percentage of a small velocity. Nevertheless, 82% of readings were within 10% of each other and 92% within 15% of each other. However, as the highest velocity recorded

for the very low flow experiments was 2.8 cm./sec.,all the velocities were perforce calculated from the least sensitive part of the probe calibration curve (see section 5.4). Thus, although the contour patterns were quite probably representative, the recorded velocities could not be relied on as accurate and for this reason the velocity plots for very low flow experiments have not been included in the specific graphical and numerical analysis which follows.

Calculation of the flowrate from the computed values of velocity at each cross-section was carried out by numerical integration as described in section 6.5. These served as a check on the accuracy of the velocity plots since they should be constant both for all the distributions in the high flow experiments and also for all the distributions in the low flow experiments. For high flow, the average error modulus between each computed flowrate and the mean of all computed flowrates, which was itself just 2% different from the mean actual flowrate, was found to be 5.0% with a maximum error of 13%. For low flow, the average error modulus between each computed flowrate and the mean of all computed flowrates, which was 3% different from the mean actual flowrate, was found to be 5.4% with a maximum error of 10%. This showed that good correlation existed between the separate plots and that there was also good agreement between the computed and measured flowrates.

6.4 Description of Velocity Plots

A total of 21 contour plots was produced for the various combinations of variables mentioned in section 6.2. These were plotted at a scale of ten to one, each taking up a full size A4 page and thus to reproduce them directly would result in an unmanageable stack of pages, making it difficult to follow the progress downstream of salient features. Although some numerical description of the plots is possible (see section 6.5) it was felt that the contour plots themselves were of fundamental importance and should be reproduced. Photographing and subsequent photocopying reduced the size to enable a number of the plots to be displayed on one page and this made direct comparison of one plot with another much easier. The plots themselves are shown in figures 6.3 to 6.8. They were taken in limb B and are presented as coming towards the observer, the inside wall of the limb being on the right of the plot. Figures 6.3 and 6.4 show the downstream progress of the contours for low flow in branch 1, figures 6.6 and 6.7 for high flow in branch 1 and figures 6.5 and 6.8 for low and high flow respectively in branch 2. Each plot is coded by three symbols, a number indicating the branch number, the letter H or L indicating high or low flow and a number showing the distance downstream from the carina in cms. Thus 1L23 indicates the plot 23 cm. downstream of branch 1 in low flow.

The branch carina splits the oncoming parabolic flow in half diverting half down each daughter tube. Thus at

the beginning of each limb, the velocity profile is a kind of semi-paraboloid with the peak velocity on the inside wall. This can be seen in the plots 3 cm. downstream as the high plateau on the right-hand side. The crescent-shaped contours extend round the outside of the tube, giving rise to the symmetrical double-peaked profile observed by Schroter and Sudlow (1969) in the plane normal to the plane of bifurcation. In both high and low flow, the peak velocity recorded was approximately 0.9 that of the peak parabolic input. This was to be expected since the cross-sectional area of the daughter tubes is 1.125 that of the parent tube which should cause an overall reduction in velocity of 0.89. The large area of low flow seen on the outside of the branch marks the position of the secondary vortices described in section 4.2 which have only a low axial velocity component. These gradually spread across the tube convecting the high velocities away from the inside wall though viscous action was at the same time slowing down these higher velocities.

Studying first the development in low flow in branch 1 (figs. 6.3 and 6.4) it can be seen that at 7 cm. downstream the high plateau is less marked and that the high velocities on the inside are being circulated round to where the very low velocities were before. At 11 cm. downstream the velocities are much more uniform, the originally high plateau much less marked and showing a slight clockwise rotation from the 7 cm. downstream position. (Note the 3.2 cm./sec. contour which has been inserted for visual comprehension

purposes but which tends to make the velocity gradients look steeper than they are). The 15 cm. downstream position shows the logical development, the plateau broadening out, moving towards the centre of the tube and beginning to increase in velocity. (Similarly, note the 3.8 cm./sec. and 3.9 cm./sec. contours). The plots at 23, 31 and 47 cm. downstream show the velocity plots approaching nearer and nearer to the steady-state downstream paraboloidal plot with a peak velocity of 5.5 cm./sec. Dye studies on the helical secondary flows showed them dying out approximately 15 cm. downstream and this is borne out by the stabilisation in the velocity plots between the 15 cm. and 23 cm. downstream positions.

The low flow plots in branch 2 (figure 6.5) show a remarkably similar development to those in branch 1, even down to quite small details and this would indicate that the inside geometry of the branch has little effect on the downstream velocity distributions in low flows.

Study of the high flow velocity plots in branch 1 (figures 6.6 and 6.7) shows a similar development to that in low flow though the velocities take longer to redistribute themselves and the detailed flow patterns are more complex and less stable. At 7 cm. downstream the high plateau seen on the inside wall of the 3 cm. downstream position has begun to split into two and move round the tube walls. Dye studies at this position showed the presence of very strong helical vortices. The plot at 11 cm. downstream shows that these vortices have distributed the

high plateau completely away from the inside wall, the velocity pattern becoming much more uniform. The plot at 15 cm. downstream, where the vortices were beginning to abate though they persisted in a small way for some 30 to 40 cm. downstream, shows the rearranging of velocities that lead on to the plot at 23 cm. downstream. The plots at 23, 31, 47 and 63 cm. downstream show the development towards the expected paraboloidal profile. Certain detailed features, such as the dip in the first quadrant, persist for a long distance downstream.

The high flow velocity plots in branch 2 (fig.6.8) are less complex than in branch 1 and this would seem to indicate that the helical vortices were less strong in branch 2 though this was not apparent from dye studies. A slight clockwise rotation is noticeable in the downstream development of velocity distribution.

The very low flow velocity plots which have not been reproduced for the reasons mentioned in section 6.3 showed a development very similar to the low flow plots but stabilising rather more quickly although the change from crescent-shaped to circular contours still took place at around 11 cm. downstream.

In all the four cases studied in detail, the development of the downstream velocity distribution was similar. The high plateau on the inside wall was convected round the tube by the action of the secondary vortices and the crescent-shaped contours gave way to the paraboloidal development at approximately 11 cm. downstream (6 diameters), this

distance being independent of input velocity and branch geometry. Since the spreading effect of vortices increases with their strength (Li and Lam, 1964), it is possible that an increase in input velocity which thus increases vortex strength (section 4.2) causes an increase in the spreading effect of the vortices sufficiently great to keep this distance of 6 diameters approximately constant. The stability of the flow downstream, however, decreased with increased input velocity. Branch internal geometry had little effect on the velocity distribution especially in low flow though in high flow, the smooth branch 2 gave a slightly more stable development than the sharp branch 1. There was a slight overall clockwise rotation of all the velocity plots as the flow moved downstream. It was thought that this might be caused by slight swirl in the input pipe but dye studies showed no trace of this and it Was concluded that it was caused by a tertiary flow induced by slight imbalance in the secondary helical vortices.

Knox (1962) has made pressure measurements downstream of various branches and has suggested that the length downstream required to ensure 99% developed flow is given by:

$$L = K\ a\ Re$$

where K is a constant depending on the angle of the branch, the area ratio and the discharge ratio. Using Knox's value of K for the present branch shape gives recovery lengths of 66 cm. and 33 cm. for high and low flow respectively. Although the velocity profiles were symmetrical at these distances, the centreline velocity was only 1.6 times the

mean velocity and the profile was thus still flattened at the centre. From these distances downstream, however, there is only 5% change in pressure gradient as the profile becomes fully developed and Knox's pressure tappings would thus indicate that fully developed flow occurred much earlier than it actually did. Extrapolation of the plot of centre-line velocity against distance downstream (figure 6.9, section 6.5.1) show that the values of recovery length are very approximately 90 cm. for low flow and 180 cm. for high flow. Knox's values of K should therefore be increased by an approximate factor of three.

A further set of downstream velocity distributions was plotted in branch 1 for a high flow input profile which was 90% flat for over 50% of the tube radius. The peak velocity was approximately 1.5 times the mean velocity and the mean square velocity was approximately 1.17 times the squared mean velocity. These compare with values of 2.0 and 1.33 respectively for a paraboloidal profile. It was found that the development was very similar to the paraboloidal input in branch 1 though it was slightly more stable. This was as expected owing to the lower value of mean square velocity on which the vortex strength depends. The initial high velocity plateau on the inside wall of the limb was slightly wider than in the paraboloidal case but this had little effect on the downstream development. This experiment showed that the development of the downstream velocity distribution was not sensitive to small changes in the shape of the input profile except in as much as they altered the value of the mean square velocity.

6.5 Numerical Analysis of Velocity Plots

6.5.1 Centreline Velocity

It was felt that some numerical description or analysis of the velocity plots would be useful. The centreline velocity was an obvious example and the values of the ratio of the centreline velocity to the mean velocity, $u_c/\bar{u}$, are shown in table 6.2 for each position downstream. These values of $u_c/\bar{u}$ were plotted against z, the distance downstream of the carina. This graph is shown in figure 6.9 and shows two distinct phases. Up to 11 cm. downstream the values of $u_c/\bar{u}$ are independent of input velocity, input profile and branch geometry and all values lie approximately on a straight line. This line levels off sharply at 11 cm. downstream and breaks into two, one curve being for high flow and the other for low flow. From this value of z onwards, the graphs follow similar lines to those predicted by Langhaar (1942) for an entrance length. Langhaar's theoretical treatise on entrance and transition lengths is well supported by Nikuradse's (1934) experimental results, the greatest difference being 6% for z greater than 0.005 a Re. It is noticeable that this value of 11 cm. downstream is the same distance as that observed in section 6.4 for when the velocity plots changed from crescent-shaped to circular and that this distance too was independent of input velocity and branch geometry. Dimensional analysis gives $u_c/\bar{u} = f(z/d, R/d, Re)$ and hence for the first 11 cm. where it has been shown that $u_c/\bar{u}$ is independent of Re and R/d, $u_c/\bar{u} = f(z/d)$. Figure 6.9 yields the empirical formula

CM. DOWNSTREAM

	Branch Flow	3	7	11	15	23	31	47	63
1. $\frac{u_c}{\bar{u}}$	1H	0.69	0.96	1.25	1.29	1.40	1.40	1.49	1.55
	2H	-	1.00	1.27	1.30	-	-	-	-
	1L	0.63	0.96	1.22	1.36	1.56	1.65	1.73	-
	2L	-	0.98	1.26	1.41	-	-	-	-
	1H(Flat)	0.68	0.89	1.19	1.35	-	-	-	-
2. $\frac{M2}{a^2}$	1H	0.444	0.443	0.401	0.392	0.382	0.376	0.357	0.353
	2H	-	0.441	0.397	0.390	-	-	-	-
	1L	0.441	0.427	0.393	0.376	0.350	0.339	0.335	-
	2L	-	0.429	0.392	0.371	-	-	-	-
	1H(Flat)	0.430	0.393	0.405	0.377	-	-	-	-
3. $\frac{\Delta P}{\Delta P_{Posi.}}$	1H	3.47	2.75	1.80	1.67	1.59	1.47	1.28	1.23
	2H	-	2.59	1.67	1.63	-	-	-	-
	1L	2.86	2.14	1.65	1.43	1.23	1.16	1.12	-
	2L	-	2.18	1.54	1.37	-	-	-	-
	1H(Flat)	2.83	2.23	1.84	1.49	-	-	-	-
4. $\frac{M2}{M2_{Ent.}}$	1H	1.07	1.13	1.06	1.06	1.06	1.07	1.04	1.04
	2H	-	1.12	1.05	1.05	-	-	-	-
	1L	1.11	1.15	1.09	1.06	1.02	1.00	1.00	-
	2L	-	1.16	1.09	1.05	-	-	-	-
	1H(Flat)	1.04	1.00	1.07	1.02	-	-	-	-

TABLE 6.2 (continued)

5.	$\frac{\Delta P}{\Delta P_{Ent.}}$	1H	1.19	1.27	1.03	1.05	1.15	1.15	1.12	1.13
		2H	-	1.20	0.96	1.02	-	-	-	-
		1L	1.20	1.47	1.19	1.11	1.07	1.06	1.03	-
		2L	-	1.49	1.11	1.06	-	-	-	-
		1H(Flat)	0.97	1.03	1.05	0.94	-	-	-	-

1. Ratio of centreline velocity to mean velocity. (section 6.5.1)
2. Value of $M2/a^2$. (section 6.5.2)
3. Ratio of pressure gradient to pressure gradient in same Poiseuille flow (section 6.5.3)
4. Ratio of $M2/a^2$ to $M2/a^2$ in same entrance flow (section 6.5.2)
5. Ratio of pressure gradient to same entrance flow pressure gradient (section 6.5.3).

Table 6.2.

for the initial 11 cm. (6 diameters) downstream:

$$u_c/\bar{u} = 0.47 + 0.135\ z/d \qquad (6\text{-}1)$$

6.5.2 Distribution Moments

Schreck and Mockros (1970), who have drawn the velocity profiles at two positions downstream for two different branching shapes in air flow, have considered the velocity plot as a distribution function and have calculated a set of distribution moments, MO, M1, M2 and M3, being defined in polar co-ordinates as follows:

$$MO = \int_o^{2\pi} \int_o^a u(r,\theta)\ r\ dr\ d\theta$$

$$M1 = \int_o^{2\pi} \int_o^a u(r,\theta)\ r^2\ dr\ d\theta/MO$$

$$M2 = \int_o^{2\pi} \int_o^a u(r,\theta)\ (r-\bar{r}).(r-\bar{r})\ r\ dr\ d\theta/MO$$

$$M3 = \int_o^{2\pi} \int_o^a u(r,\theta)\ (r-\bar{r})((r-\bar{r}).(r-\bar{r}))r\ dr\ d\theta/MO$$

From probability theory these moments can be explained as follows. MO is simply the flowrate, Q. M1 gives the location of the centre of mass flow, $\bar{r}$. M2 is defined with respect to the centre of mass flow and is a measure of the variance, $\sqrt{M2}/a$ being the standard deviation. M3 is a measure of the skewness of the distribution and is also defined with respect to $\bar{r}$.

These distribution moments were calculated for all the velocity plots described above by dividing the tube cross-section into 64 equal areas, interpolating a mean velocity

to each area from the computed values of $V(j,k,\ell)$ and integrating numerically with the requisite values of r and $r\ dr\ d\theta$.

Although Schreck and Mockros have used all three of the higher distribution moments, it was felt that the errors inherent in the calculation of M1 and M3 precluded their use in all but the most qualitative of arguments and that M2 was the only moment to be of quantitative use. This is due to the fact that the calculation of M1 and M3 involves the sign of r whereas in the calculation of M2, all r^2 are positive. An error of only 10% in just one of the interpolated mean velocities could lead to errors of the order of 15 to 20% in M1 and from 15 to 400% in M3 whereas the corresponding error in M2 would be only of the order of 0.2%. Therefore only the values of M2 have been used for numerical analysis and they are tabulated as $M2/a^2$ in table 6.2.

Schreck and Mockros have come to the erroneous conclusion that $M2/a^2$ does not vary with inlet Reynolds' Number. Their values of $M2/a^2$ vary from 0.396 to 0.464 which they conclude is approximately constant. The variation in $M2/a^2$ from a paraboloidal profile to a completely flat profile is only from 0.333 to 0.500, however, so that Schreck and Mockros' variation is in fact relatively large.

It was found that the values of $M2/a^2$ varied in a manner similar to the variation of $M2/a^2$ in entrance flows.

Table 6.2 shows the ratios of the experimental values of $M2/a^2$ to the values at the same downstream position in a symmetrical entrance flow. These latter values were calculated from Langhaar's (1942) theoretical velocity profiles. It can be seen that the experimental values start higher than the entrance flow values but fall faster and become equal to the entrance flow values at some distance downstream. The mean variation between the two sets of values was 7% with a maximum of 15% at 7 cm. downstream. Comparison of the experimental values of $M2/a^2$ with values calculated from Nikuradse's (1934) experimental entrance flow velocity profiles gave a slightly closer fit with a mean variation of 5% and a maximum of 13%. The experimental values of $M2/a^2$ in the flat inlet profile experiment were generally much closer to the Langhaar values than those in the paraboloidal inlet profile experiment with a mean variation of 3% and a maximum of 7%.

The computations for the distribution moment calculation made it possible also to calculate the flow distribution on the two sides of the limb. At 3 cm. downstream of branch 1 in both high and low flows, 65% of the flow was concentrated in the inside half of the limb and 35% in the outside half. By 7 cm. downstream, however, the distribution had become 55% to 45% and an approximate 50%-50% distribution was achieved soon after. The distribution between the top and bottom of the limb remained close to 50% in each, varying only by two or three per cent. Thus, if a second branch was placed 3cm. downstream of the first

and in the same plane, it would be expected that the two limbs of this second branch would receive an unequal flow distribution of 65% - 35% corresponding to the input flow distribution. This was not tested experimentally.

6.5.3 Energy Dissipation

Langhaar's theoretical results also enable the downstream pressure drop in an entrance flow to be calculated and this can also be compared with that found in the downstream branch flow. The downstream pressure drop is equal to the dissipation of energy per unit volume, the rate of which is given by Goldstein (1938) as:

$$\Phi = \mu \{ 2 \left(\frac{\partial u_r}{\partial r}\right)^2 + 2 \left(\frac{1}{r}.\frac{\partial v}{\partial \theta}\right)^2 + 2 \left(\frac{\partial w}{\partial z}\right)^2 + \left(\frac{1}{r}.\frac{\partial w}{\partial \theta} + \frac{\partial v}{\partial z}\right)^2 + $$

$$+ \left(\frac{\partial u_r}{\partial z} + \frac{\partial w}{\partial r}\right)^2 + \left(\frac{\partial v}{\partial r} + \frac{1}{r}.\frac{\partial u_r}{\partial \theta}\right)^2 \}$$

Assuming that the axial velocity, w, and its derivatives are large compared with u_r and v, and that derivatives in the z-direction are small compared with those in the r and θ directions, these assumptions being justified by the velocity plots themselves,

$$\Phi \simeq \mu \{ \left(\frac{1}{r}.\frac{\partial w}{\partial \theta}\right)^2 + \left(\frac{\partial w}{\partial r}\right)^2 \} \qquad (6\text{-}2)$$

The value of Φ at each downstream position was calculated by dividing the tube cross-section into 64 equal areas, interpolating a mean velocity to each area from the measured velocities and summing equation (6-2) numerically with the requisite values of r and θ. This value of Φ

was then multiplied by the area and divided by the calculated flowrate (MO, see section 6.5.2) to give the energy dissipation per unit volume per unit length at that position which is in fact the pressure gradient. The values of the pressure gradient, thus calculated, were expressed non-dimensionally as a ratio to the pressure gradient in the same Poiseuille flow. These ratios are shown in table 6.2. Values of pressure gradient were also calculated from Langhaar's results at the same downstream position and the ratios of the experimental branch pressure gradients to those calculated from Langhaar are also shown in table 6.2. There was good correlation between branches 1 and 2 in all cases the mean difference being only 5%. At the start of each limb, the pressure gradient was between 20% to 50% higher than in a similar entrance flow, the maximum difference being at 7 cm. downstream. After 11 cm. downstream, however, the pressure gradient was nowhere more than 15% higher than an entrance flow and the ratios gradually tended to unity. In the flat inlet profile experiment, however, the pressure gradient was within 5% of the entrance flow value at all measured positions right from the beginning of the limb.

Pedley et al. (1971) have measured the viscous dissipation immediately downstream of branches in air flow and have obtained results showing that the rate of energy dissipation at z/d diameters downstream ($z/d \leq 3.5$) can be calculated from the approximate theoretical formula:

$$Y = \frac{C}{8\sqrt{2}} \, (\mathrm{Re}\ d/z)^{\frac{1}{2}} \qquad (6\text{-}3)$$

where Y is the ratio of the rate of dissipation in a tube downstream of a branch to its value in the same Poiseuille flow, C being a constant for a given branch. This equation was obtained by assuming that the rate of energy dissipation was a constant ratio to the rate of energy dissipation in a symmetrical flat profile with a linear velocity boundary layer, the thickness of which increased as on a flat plate, and neglecting all but the leading terms.

Values of C for branch 1 were calculated from equation (6-3) using the experimental values of Y and Re for z = 3 and 7 cm., the only values of z in the present experiments which were within or near Pedley's limitation on z/d. (z = 7 cm. gives z/d = 3.7). It was found that C varied only between 1.53 and 2.04 but the higher values of C were in those flows with lower Reynolds' numbers and vice versa which would possibly indicate that C was a function of Reynolds' number. The calculations of C from the full solution, of which equation (6-3) is only an approximation, gave slightly less spread for C though the same variation with Reynolds' number was observed. Pedley's experimental values of Y, which were obtained by making just two velocity traverses across the limb, in the horizontal and vertical planes, using a hot wire, and interpolating values of velocity for the remainder of the tube, gave values of Y varying between 1.86 and 2.75 with a mean of 2.13. It is felt, however, that the complexity of the flow in the region immediately downstream

of the branch is such as to render this experimental method undependable and liable to inaccuracy. Thus too much reliance should not be placed on this result.

It was found that the values of Y in the present paraboloidal input experiments for both branches for all z up to and including 11 cm. could be expressed within 5% by the empirical formula:

$$Y = 0.068\ (Re)^{\frac{1}{4}}\ (10.5 - z/d) \qquad (6\text{-}4)$$

6.6 Summary

The main difficulty in the analysis of the flow downstream of branches is the lack of availability of any theoretical treatment. Approximate solution of the Navier Stokes equations has only been achieved in the greatly simplified case of symmetrical flow in curved pipes of non-varying diameter under certain conditions. Dean (1927) has produced an analytical solution for values of his $K(=2aRe^2/R)$ up to 576 and McConalogue and Srivastava (1968) have more recently extended his work by producing a numerical solution for values of K up to $2x10^4$. This compares with the branch flow in which the flow is asymmetric through a tube of varying diameter with a value of K of the order of 10^6. No solution of any form is available for branching flow and it seems unlikely in view of the complexity of the flow regime that any solution will be forthcoming, at least by present-day methods. There can therefore be no direct comparison between theoretical treatises and experimental results.

The velocity distribution downstream of the branches has been plotted in detail with errors kept to a minimum and experimental correlation has been shown to be good throughout. It was found in all cases that the initial velocity distribution consisted of a high velocity plateau on the inside of the limb with crescent-shaped contours extending round to the outside of the limb where contra-rotating vortices were set up, the strength of which depended on the mean square velocity of the input profile. The maximum velocity at 1½ diameters downstream was 0.9 that of the maximum input velocity. By 6 diameters downstream, this distance being independent of inlet Reynolds' number, branch geometry and inlet profile shape, the velocity distribution had become very approximately symmetrical through the action of viscosity and the spreading effect of the helical vortices. Within this first 6 diameters downstream, the ratio of the centreline velocity to the mean velocity varied linearly with distance downstream and was independent of inlet Reynolds' number, branch geometry and inlet profile shape.

In all cases, branch geometry and input profile shape had little or no effect on the general velocity patterns. The mean square input velocity affected the strength of the helical vortices and the stability and development of the velocity distribution after six diameters downstream but had little effect on the distribution within the initial six diameters.

Numerical analysis of the velocity plots showed that

comparisons could be made with symmetrical inlet flows. For paraboloidal input profiles, for distances up to 33 diameters downstream, the spread of the distribution (M2, see section 6.5.2) was on average 7% higher than in an entrance flow at the same downstream distance, the highest values being at 4 diameters downstream. The energy dissipation was on average 15% higher than in an entrance flow with the highest values again at 4 diameters downstream. When the input profile was flat over 50% of the radius (25% of the area), the spread of the distribution was on average only 3% higher than in an entrance flow while the energy dissipation was the same as in an entrance flow. It was also found that the positioning of a second branch at 1½ diameters downstream and in the same plane as the first branch should lead to a 65% - 35% flow distribution in the limbs of the second branch owing to the unequal flow distribution in the limb of the first branch.

7. DESIGN OF A METHODOLOGY FOR SAMPLING AND ANALYSING PULSATILE FLOW VELOCITIES.

7.1 The data logging system

It was intended to extend the work of section 6 to pulsatile flows and to measure the time-varying cross-sectional velocity distributions downstream of the branch. Some system therefore had to be devised to obtain the velocity data in relevant form.

Pulsatile flow was achieved by superimposing a sinusoidal variation on the steady flow by means of a piston operating on the fluid in the settling chamber. The piston was operated by an electric motor through a cam and follower arrangement. Details can be found in Bellhouse and Bellhouse (1969a).

At each point in the cross-section, the directionally-sensitive probe would measure the instantaneous axial velocity throughout the pulse and output a continuous variable voltage signal through the anemometer and voltmeter. It was required to sample this output at suitable intervals throughout the pulse, say ten times in all, at speeds up to 1 pulse/sec. and also to take a chain of say five pulses at each point in order to obtain a mean and so lessen errors. This meant that 50 probe voltages had to be sampled and stored from each cross-sectional position at a rate of up to 10 per second. Assuming that 96 points were still used within the cross-section as in steady flow, and it was considered that using many less than this would

bring in inaccuracies, a total of 50 x 96 = 4800 voltages had to be stored and processed in order to obtain each time-varying downstream plot. Each voltage would consist of a minimum of five digits and a delimiter.

Various methods, both automatic and manual, of dealing with this amount of data were considered and it was finally concluded that direct digital output would be of the optimum suitability. The output from the anemometer was fed into a Dynamco 2022 digital voltmeter which output the five voltage digits in parallel form into a Dynamco 6003/8 serialiser and output unit. This transformed the parallel voltage digits into serialised form and converted them to electrical punched tape pulse codings. These were fed to a Data Dynamics 110 tape punch to finally produce the voltages on punched tape in the format ddddd;CR/LF where the five digits were followed by an Algol delimiter and a carriage return/line feed symbol. This latter was included to facilitate tape print-out if required. The output from the voltmeter to the serialiser was governed by an external 9-Volt trip and thus the number of voltages output per pulse could be strictly controlled.

The advantages of the system were paramount. It gave direct, immediate output with no need for any intermediate analogue to digital conversion. Values of other variables, such as probe resistance and set resistance, could be inserted directly onto the punched tape during an experiment by means of a small numeric keyboard coupled to the

serialiser and thus no tape editing was required before processing. The system was permanent and reliable. The speed of operation of the system was determined by the speed of the tape punch. The Data Dynamics 110 operated at a maximum speed of 110 characters/sec. which gave a top operating speed of 15 voltages per second for voltages of seven characters. By dropping the CR/LF symbol on the tape so reducing each voltage to six symbols only, the operating speed could be increased to 18 voltages per second. If faster speeds were required, the anemometer output could be recorded on magnetic tape in analogue form and played back to the digital voltmeter at a slower speed. Using an Ampex tape recorder, the sampling rate could thus be increased by a factor of eight, giving an overall sampling rate of about 120 per second which is fast enough for most signal inputs apart from turbulence measurements. For the purposes of the experiments in hand, however, the straightforward sampling rate of 15 voltages per second was more than sufficient.

Control of the output voltage sampling was achieved by means of an electronic system consisting of a variable frequency multivibrator which was gated by two micro-switches operated by contacts on the pulse-producing piston wheel. This multivibrator produced a chain of 9-Volt electrical impulses which were fed to the external trip of the digital voltmeter. The sampling rate, i.e. the multivibrator frequency, could be varied from 1 to 20 per

second. Since the microswitches were always operated at the same relative position in the velocity pulse, the sampled voltages also always occurred in the same positions relative to the pulse. This was important both for the taking of means and for the comparison of pulses in different downstream positions. A further refinement to the system enabled a chain of n ($n \leq 7$) velocity pulses to be sampled automatically, the system shutting off when it had sampled the nth. pulse. Thus with the probe in one position, the pressing of one button would sample a chain of n pulses at say ten velocity voltage samples per pulse and output these readings on punched tape all entirely automatically. A block diagram of the system is shown in figure 7.1, a diagrammatic output form for n = 2 is shown in figure 7.2, a photograph of the electrical apparatus shown in figure 7.3 and the modus operandi described below.

Assume that it was required to sample a chain of three velocity pulses at a rate of ten samples per second. Reference should be made to the block diagram shown in figure 7.1. The set count switch was set to three and the frequency of the multivibrator adjusted to give the required ten samples per pulse. When the start button was pressed, a relay pulled in and held in the master switches on the 'start' and 'stop' impulse lines. The next time that the 'start' microswitch was operated by the contact on the piston wheel, an electrical impulse was fed through a monostable circuit to a bistable gate

and started the multivibrator thus commencing the voltage sampling. This bistable gate held the multivibrator in the same 'home' position when it was not operating so that it always started in the same direction. The 'start' impulse also operated a counter and the figure one appeared in binary lamps. Since this count of one did not equal the set count of three, there was no output from the count/set count Equivalent gate and nothing further occurred. Towards the end of the velocity pulse, the 'stop' microswitch was operated and a second impulse was fed to the bistable gate cutting out the multivibrator. This second impulse was also fed to an And gate together with the output from the count/set count Equivalent gate but since this latter was zero, no further action was taken. The second pulse to be sampled followed the same pattern as the first. The counter went up to two and this figure appeared in the binary lamps; it was still not equal to the set count, however, and nothing further occurred, though the multivibrator was started and stopped as before. At the beginning of the third pulse, the impulse from the 'start' microswitch started the multivibrator as usual. The counter went up to three and since this time the count equalled the set count, an output appeared from the count/set count Equivalent gate. This output was held at the And gate input until the 'stop' impulse appeared when the And gate gave an output to a relay driver which dropped out the relay thus opening the master switches on the 'start'

and 'stop' impulse lines. No further impulses could thus be received by the system until the whole procedure was re-initiated by pressing the start button. The voltmeter had thus received a chain of three sets of ten impulses, each set being in the same position relative to the velocity pulse. On each impulse, the voltage being read at that instant was output to the serialiser and tape punch to give three sets of ten voltage readings on punched tape each set being in the same relative position with respect to the velocity pulse.

7.2 The Computer Program

The punched tape output was in the following form. For each of the 12 points in each of the 8 traverses, fifty voltages were sampled in five sets of ten time-varying readings. At beginning and end of each traverse a value of ΔR was also included on the tape and the calibration constants and identification data were added on at the start of the tape. An Algol computer program for use on the Oxford University English Electric KDF9 computer was developed to process this data and this is shown in Appendix 1, its structure being described below.

For each traverse, at each cross-sectional position a value of ΔR was interpolated from the given values at beginning and end of the traverse and the value of $V_b^2/\Delta R$ was calculated for all readings in the traverse. (See section 5). The value of velocity corresponding to each value of $V_b^2/\Delta R$ was then calculated using the calibration

constants provided and this velocity was referred to as V(i,j,k) where i (1-10) was the time position in the pulse, j (1-12) the position in the traverse and k (9-13) the pulse number plus eight. e.g. V(2,3,12) was the second time-sampled velocity in the fourth pulse at the third traverse position. A mean of all V(i,j,k) was taken over the number of pulses, k, and this mean was termed V(i,j,ℓ) where ℓ(1-8) was the number of the traverse. This method of using a three-dimensional array to describe all the velocities instead of a four-dimensional array V(i,j,k,ℓ) was used to save on computer storage space. A storage space of only 1560 words was required instead of the 4800 words which would be required for the more conventional four-dimensional array.

The difference between each value of V(i,j,k) and the mean V(i,j,ℓ) was also calculated as a percentage error. Checks were included in the program to ensure that any velocities outside the range considered, perhaps caused by punching errors which did occur very occasionally, were excluded as also were any values that fell more than 25% from the calculated means. In such an event, the relevent mean would then be recalculated without the offending values. Having obtained all the values of V(i,j,ℓ), centreline velocities, M(i,ℓ) were interpolated for each time-sample and traverse, a mean taken over the traverses and all the values of V(i,j,ℓ) corrected to the same mean traverse centreline velocity for each value of i. These corrected values of V(i,j,ℓ) were output on the

lineprinter and were then used in the automatic graphical and numerical processing which followed.

The distribution moments were calculated in a similar fashion to steady flow. The time-varying velocity distribution was split into 64 equal areas for each time sample, a mean velocity interpolated to each area from the measured velocities and the distribution moments integrated numerically. These were output from the computer in both visual and punched tape form in case further computer analysis of them was required.

The facility of an English Electric incremental plotter linked to the KDF9 gave the opportunity of having the results output in direct graphical form. For each sampled time the following routine was obeyed. A set velocity was taken and the measured velocities in each traverse were scanned to see if any of them were higher than the set velocity. If so, then the set velocity must have occurred within the traverse. Linear interpolation between adjacent points and parabolic interpolation between the end points and zero then gave the positions in each traverse where the set velocity occurred. These positions were then plotted onto a plan of the cross-section to give a series of such points around the cross-section. This was repeated for various set velocities, a different plotting character being used for each one. The automatic graphical output was left in this form and the series of points for each set velocity were joined up manually to give a velocity contour for

that set velocity. Thus a complete velocity contour plot was produced for each sampled time.

Some work was done on the feasibility of using the graph plotter routines to draw in the contours automatically but it was eventually decided that the complexity of the program that would be required both to join up the points in the correct order for all the various contour configurations obtained and also to take into account the shape of neighbouring contours in the determination of the shape of any one contour was such that its development would be more time-consuming than the manual drawing itself.

8. THE VELOCITY DISTRIBUTION DOWNSTREAM OF BRANCHES IN PULSATILE FLOW.

8.1 Experimental Technique

An investigation into the velocity profiles downstream of the branch was carried out in pulsatile flow in order to discover how different they were from the steady flow profiles and what effect, if any, the pulse had on the flow distributions. The methodology for dealing with pulsatile flows in general has already been described in section 7. By varying the independent parameters of flowrate, pulse frequency and pulse amplitude, a pulse of any desired mean flowrate, frequency and backflow ratio could be obtained. It was decided to use the same mean flowrates as had been used in the steady flow experiments at a frequency of 0.5 cycles/sec. This gave Strouhal numbers (= fd/u) of 0.10 and 0.21. Experiments were carried out in branch 1 in both high (31.6 ml./sec. mean inlet) and low (15.5 ml./sec. mean inlet) flows at 3, 7, 11 and 15 cm. downstream from the carina. Choosing the pulse amplitude was more difficult since, once the flow was developed, substantially more backflow appeared near the inlet tube walls at the end of the pulse than did at the tube centre. Thus, arranging for zero backflow at the centreline gave very substantial backflow at the walls and arranging for zero backflow at the walls meant that the centreline velocity was always very much greater than zero. A compromise was therefore reached such that backflow

appeared at the walls for approximately 40% of the pulse, the centreline velocity approaching fairly close to zero though never actually reaching it. The volume flowrate had a minimum of approximately zero, rising to approximately twice the mean value. Thus the pulse could be described by reference to the mean flowrate, $\bar{Q}$, as

$$Q(t) = \bar{Q} (1 + \cos \pi t) \qquad (8\text{-}1)$$

One of the limitations of the directionally-sensitive thin film velocity probe was exposed during these experiments and this was that owing to the lack of sensitivity of the calibration curve (figure 5.5) between zero and 2 cm./sec. it was not possible to follow in detail pulsatile velocities between 2 and -2 cm./sec.. The probe measured forward and backward velocities equally so that a velocity falling from 3 cm./sec. to -3 cm./sec. would appear as falling from 3 cm./sec. to 2 cm./sec. and then rising back to 3 cm./sec. Bearing this in mind, however, and watching the pulse on an oscilloscope screen, areas of backflow could be observed and noted. The shape of the inlet pulses for high flow is shown in figure 8.1. which shows the variation of velocity, u, with time, t, for both the centreline and for a position 1.67 mm. from the inlet tube wall. The cross-sectional profile was approximately paraboloidal for all times though it was obviously distorted when backflow appeared at the walls. The numbers one to ten on the abscissa refer to the positions in the pulse at which the velocity samples were taken in the daughter

tube and these time positions are referred to as t = 1,2,3.....10. The low flow input pulse shape was similar to figure 8.1 though the peak centreline velocity was not relatively quite as high as in the high flow case.

Measurement of the downstream velocity plots was achieved by using the methodology developed in section 7 in conjunction with the basic experimental method used for steady flow and described in section 6. The same precautions as described in section 6 were taken to ensure equiflow. At each downstream position for each flowrate, the probe was traversed across the cross-section at eight successive angles of $22\frac{1}{2}^{o}$, samples of pulsatile anemometer voltage being taken at twelve positions within each traverse. Five pulses were sampled at each position at a rate of ten readings per pulse and these were output on punched tape as described in section 7. Readings of the probe 'cold' resistance and the 'set' resistance were taken at the beginning and end of each traverse and the value of ΔR was calculated ($\Delta R = R_s - R_o$) and included on the tape by means of a small numeric keyboard coupled to the serialiser. The probe was calibrated both before and after each experiment, a mean taken and the calibration constants calculated as in section 5.4. These were included at the beginning of the punched tape. Using this data, the anemometer voltages were processed by the computer to produce a set of velocity plots as described in section 7. Each velocity plot was coded by five symbols. The

first three were the same as those used in steady flow, the figure 1 or 2 denoting the branch number, the letter H or L indicating high or low flow and a number indicating the downstream position. There then followed the letter P denoting pulsatile flow and this was followed by a number between 1 and 10 inclusive indicating the point of time in the pulse. e.g. 1H15P3 is the pulsatile flow velocity plot taken in high flow 15 cm. downstream from the carina of branch 1 at the third time-sampling position. (i.e. halfway during the acceleration phase; see figure 8.1).

8.2 Errors

The sampling of five pulses at each traverse position and the taking of a mean enabled the percentage difference between each of the five samples and the mean to be calculated thus giving a check on the consistency of the results. Of the 19,200 readings taken in high flow, (10 samples each of 5 pulses at 96 traverse positions at each of 4 downstream positions) 77% were within 5% of their respective mean, 94% were within 10% of their respective mean and 98.5% within 15% of their respective mean. Of the 19,200 readings taken in low flow, 100% were within 5% of their respective mean. This showed that consistency was excellent, particularly in the low flow experiments, and one can note that in general the scatter was less than had been observed in the steady flow experiments.

The calculation of MO, i.e. the flowrate, for each time sample at each of the four downstream positions also gave a chance of correlating the four separate experiments. For each value of t, the value of MO should be the same at each downstream position if the flow is assumed incompressible. A mean was therefore taken of the four values of MO at the four different downstream positions from t = 2 to t = 9 and the percentage differences of each value of MO from its respective mean calculated. (The plots at t = 1 and t = 10 were not studied for the reasons given below). It was found that the mean absolute difference of the values of MO from their respective mean was 4.8% for high flow and 6.9% for low flow and this was considered to show good correlation between the separate experiments.

8.3 The Pulsatile Flow Velocity Plots

Each velocity plot consisted of a set of constant velocity contours. For low flow, these ran from 2 cm./sec. in steps of 1 cm./sec. to 7 cm./sec., the maximum integer value recorded, and backflow is recorded where in excess of 2 cm./sec. as negative values. For high flow, the contours ran from 4 cm./sec. in steps of 2 cm./sec. to 16 cm./sec. and backflow is recorded as negative values where in excess of 4 cm./sec. The velocity plots were produced from the computer at a scale of ten to one, each occupying a full size A4 page. As before, photographing and subsequent photocopying

enabled several plots to be shown on one page thus reducing the data to manageable size.

At the beginning and end of each pulse (t = 1 and t = 10), the velocity plots were of little interest, there being uniformly no more than one contour, which was quite possibly suspect owing to the directionally-sensitive probe's inability to detect low velocities, and these plots have therefore not been reproduced. The remaining plots for t = 2 to t = 9 are shown in figures 8.2 to 8.9. Figures 8.2 to 8.5 show the time-varying plots obtained in low flow at 3, 7, 11 and 15 cm. downstream of the carina of branch 1 respectively and figures 8.6 to 8.9 similarly for high flow. They are presented in limb B, the flow coming towards the observer and the inside wall of the limb being on the right.

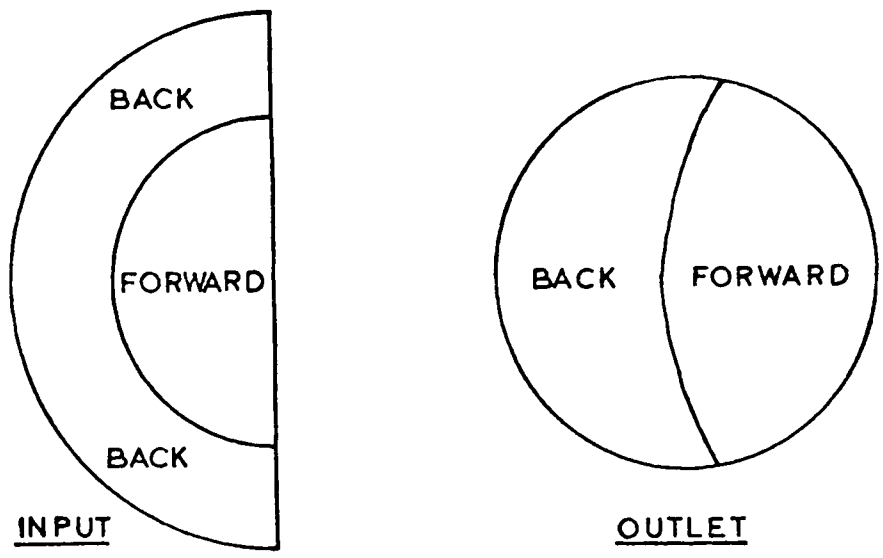
Studying first the low flow plots, 3 cm. downstream (figure 8.2), the four plots in the accelerating phase from t = 2 to 5 show a marked resemblance to each other, differing only in the values of the respective contours. They are also similar to the steady, low flow, 3 cm. downstream plot 1L3 (figure 6.3), the main difference being on the outside of the limb where the velocities were rather higher than in steady flow. This was due to the accelerating pulse acting first on stationary fluid with little or no vortical motion left on the outside of the daughter tube by the reverse movement of the previous pulse. (see section 4.3). New fluid entered the limb and moved to the outside of the limb with strong vorticity, as

described in section 4.2, but did not have a high enough axial velocity to reach 3 cm. downstream before being reversed at the end of the decelerating phase of the pulse. Thus the boundary layer on the outside wall of the limb at 3 cm. downstream was formed by the acceleration of low vorticity fluid already within the limb. This was a different mechanism to that in steady flow where the boundary layer was formed with strongly vortical fluid from the slow-moving areas of the inlet. Apart from this difference, the main features of the high velocity plateau on the inside wall and the crescent-shaped contours extending round to the area of low velocity on the outside wall were the same in both steady and pulsatile flow. The four decelerating plots (t = 6 to 9) show the same basic features but the velocity contours were less crescent-shaped, the velocities being somewhat further displaced from the vessel wall. Areas of backflow appeared on the outside wall at t = 8 and 9 giving rise to a two-way motion in the tube, fluid on the inside still moving forwards whereas fluid on the outside was reversing. Since this outside area of fluid had come from the slow-moving top and bottom of the inlet (see section 4), backflow occurred on the outside of the limb at the same time as it occurred near the walls of the inlet tube. Reference can be made to figure 8.10 below which may clarify this point.

The plots at 7 cm. downstream (figure 8.3) show a similar development to the steady flow plot 1L7 (figure 6.3)

FIGURE 8.10

BACKFLOW DIAGRAM



including the slight overall clockwise rotation. No backflow was observable. The plots at 11 and 15 cm. downstream (figures 8.4 and 8.5) follow the same development as in steady flow though the flows stabilised more quickly than in steady flow owing to the more rapid dissipation of vorticity in the pulsatile flow.

Study of the high flow velocity plots (figures 8.6 to 8.9) again shows a development of velocity distribution similar to steady flow. The flow again stabilised itself more quickly than in steady flow and the flow pattern was much more stable overall. (Compare plots 1H11P with 1H11, figure 6.6). Backflow was only evident as shown in plot 1H3P9.

Calculation of the ratio of centreline velocity to mean velocity (found by dividing the computed flowrate at any time, MO, by the cross-sectional area) showed remarkable consistency over the first half of the cycle. At each downstream position, the ratio of centreline velocity to mean velocity for both flowrates for the plots t = 2 to 6

remained within an average 3% of the mean value. The values of this ratio at 3, 7, 11 and 15 cm. downstream were respectively 1.01, 1.17, 1.27 and 1.30. These were rather higher than the corresponding steady flow values at 3 and 7 cm. downstream but became approximately equal to the steady flow values beyond 11 cm. downstream. This was due to the initial velocity distribution in pulsatile flow being rather flatter than in steady flow as explained above. During the second half of the cycle, the centreline velocity ratio varied rather more than the 3% observed in the first half of the cycle but the same approximate values were maintained in most cases.

As expected from the shape of the velocity plots which showed little time-varying difference, the values of $M2/a^2$ showed no consistent variation with time but were scattered about a mean value for each downstream position in each flowrate. There was in fact remarkably little difference between the time-varying values of $M2/a^2$. At each downstream position for each flowrate, the mean difference of the values of $M2/a^2$ from the mean value for t = 2 to 9 was less than 2%. Comparison of the pulsatile flow values of $M2/a^2$ with the corresponding steady flow values showed that at 3 and 7 cm. downstream, the pulsatile values were approximately 5% lower than in steady flow, this being due to the flatter shape of the profile, whereas at 11 and 15 cm. downstream the variation between the pulsatile and steady flow values was negligible.

8.4 Summary

It has been shown that the velocity profiles downstream of a branch in pulsatile flow were very similar to those observed in the same mean steady flow, the main variation being that the pulsatile flow dissipated the initial vorticity more quickly. This made the initial velocity distribution somewhat flatter than in steady flow which led to a quicker stabilisation of the flow patterns downstream. Backflow was observable on the outside of the branch 3 cm. downstream at the end of the pulse even though fluid on the inside of the limb was still moving forward. Backflow was not evident further downstream where the flow was more uniform.

There was marked similarity between the shapes of the time-varying velocity patterns. This was confirmed by the consistency of the values of the ratio of centre-line velocity to mean velocity and of $M2/a^2$.

9. DISTRIBUTION OF WALL SHEAR STRESS IN BRANCHES

9.1 Introduction

An indication of the relative magnitude of the wall shear stresses at different positions downstream of the branches can be obtained from the velocity plots described in sections 6 and 8. The more contours there are in the region close to the wall, the higher the velocity gradient and hence the higher the wall shear stress. To obtain a value for the shear stress at any position, however, involves the assumption of a particular shape for the velocity boundary layer between the wall and the first position of measured velocity at 1¼ mm. from the wall. Since several theories of the formation of early atherosclerotic lesions (see section 10) are dependent on the magnitude of wall shear stress, it was important to obtain accurate values of shear stress within and around the branch.

A thin-film, heated element for the measurement of local shear stress was made up as described in section 5.2 by painting thin layers of platinum on to a glass bead. This bead was cemented into a Perspex plug, 4 mm. in diameter, which could be inserted into any position where it was required to measure the local wall shear stress. The face of the plug containing the element was shaped to a 19 mm. diameter curvature so that when placed in the wall of the 19 mm. diameter branch daughter tubes,

there was no discontinuity in the tube wall. The probe was calibrated by inserting it into the tube wall at the end of a long, straight, 19 mm. diameter pipe, 200 diameters from entry. The velocity profile at this position was at least 98% developed for all calibration flows (Langhaar, 1942) and the wall shear stress in any flowrate could be calculated from:

$$\tau = -\mu \left| \frac{\partial u(r)}{\partial r} \right|_{r=a} \qquad (9\text{-}1)$$

$$\text{knowing } u(r) = 2\bar{u}\,(1 - r^2/a^2)$$

Measured values of $V_b^2/\Delta R$ (section 5) were plotted against $\tau^{1/3}$ and a straight line resulted. A typical calibration is shown in figure 9.1, the error bars showing the maximum scatter in the measurements at four different positions, equally-spaced around the calibration tube. This straight line was in accordance with the universal calibration for a heated element given in equation (5.5). Thus, values of local wall shear stress at any position could be obtained from this calibration curve by measuring the local value of $V_b^2/\Delta R$.

9.2 Experimental Observations

Measurements of wall shear stress were made downstream of branch 1 in steady flow in both High and Low flows. (see table 6.1 for definitions of these flows). Measurements were taken all round the tube at 3 cm. and 7 cm. downstream and also at positions in the plane of the branch at 0.4 cm. downstream. It was found at all positions that

the wall shear stress varied directly and linearly with input velocity. Figure 9.2 shows the variation of wall shear stress with distance downstream for positions on the inside, outside, top and bottom of the daughter tubes. Figure 9.3 shows the variation in wall shear stress around the tube for distances of 3 cm. and 7 cm. downstream. In both figures the shear stress is plotted as a ratio to the limb mean velocity and the distance downstream as a number of diameters. The value of wall shear stress in a similar, developed, parabolic flow in a tube of the same diameter is also shown for comparative purposes. This value is $0.042\bar{u}$ dynes/sq.cm. and all other values will tend asymptotically to this value as the distance downstream increases. It should be noted that the developed value of wall shear stress in each daughter tube was approximately 20% greater than the developed value in the parent tube. This is evident from substituting the relevant values of a and $\bar{u}$ into equation (9-1).

On the inside of the branch, the wall shear stress at 0.2 diameters downstream was $0.416\bar{u}$ dynes/sq.cm., nearly ten times the developed value. By 1.6 diameters downstream however, it had dropped to four times the developed value and by 3.7 diameters downstream to 2.7 times the developed value. On the outside wall of the branch, the wall shear stress was about $0.007\bar{u}$ dynes/sq.cm. (1/6 of the developed value) at 0.2 diameters downstream, but the developed value of $0.042\bar{u}$ dynes/sq.cm. was reached and held within one diameter downstream. The values at top and bottom of the

branch were similar to each other. They were slightly less than the values on the inside wall but followed a similar downstream development.

The values of shear stress around the tube wall at 3 cm. and 7 cm. downstream (1.6 and 3.7 diameters respectively) shown in figure 9.3 showed that the shear stress distribution was symmetrical about the diameter in the plane of the branch and that the variation with position round the tube was very close to a sinewave. At both downstream positions, the shear stress on the outside of the limb was the developed value of $0.042\bar{u}$ dynes/sq.cm. and the values of wall shear stress around the tube were given within an average 5% by

$$\tau/\bar{u} = 0.042 + B \cos \tfrac{1}{2}\theta \qquad (9\text{-}2)$$

where B was the difference between the values of shear stress on the inside and outside of the limb and θ was the angle at the tube centre between the position under consideration and the inside of the limb. At 3 cm. downstream, B = 0.128 and at 7 cm. downstream, B = 0.072.

Dimensional analysis shows that the shear stress at any position in the branch is given by:

$$\tau = C\, \bar{u}^2\, Re^n$$

where C and n are constants. Since it has been shown that τ depends directly on velocity, n can be taken as -1. Thus,

$$\tau = C\, \mu\bar{u}/d \qquad (9\text{-}3)$$

which is of the same form as for a parabolic velocity profile in a pipe.

From equations (9-2) and (9-3), the distribution of wall shear stress downstream of a branch can be written as follows with a mean absolute error of 5%. The values of $\bar{u}$ and d refer to the limb.

0.2 diameters downstream: (θ=0) $\tau/\bar{u} = 79\mu/d$ (9-4)

1.6 diameters downstream: $\tau/\bar{u} = 8(1+3.0 \cos \frac{1}{2}\theta)\mu/d$ (9-5)

3.7 diameters downstream: $\tau/\bar{u} = 8(1+1.7 \cos \frac{1}{2}\theta)\mu/d$ (9-6)

Comparison of the values of wall shear stress with values interpolated from the velocity plots by assuming a linear velocity boundary layer between the wall and the first position of measured velocity at 1¼ mm. from the wall showed varying results. At 3 cm. downstream, the values of measured shear stress were on average 15% higher than the interpolated values in high flow but 45% higher than the interpolated values in low flow. This showed that the velocity boundary layer was thicker in low flow than in high flow as shown in figure 9.4 below. This was consistent with the quicker stabilisation of the low flow velocity plots. (Section 6.4).

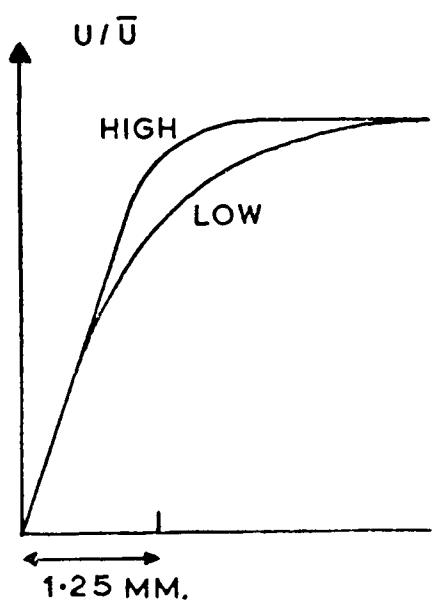


FIGURE 9.4
VELOCITY BOUNDARY LAYER

By 7 cm. downstream, however, the measured and interpolated values of shear stress were approximately equal in both high and low flows which showed that the velocity boundary layer was approximately linear.

Measurements of wall shear stress in pulsatile flows were achieved by connecting the shear stress probe anemometer output to the serialiser and tape punch and using the methodology described in section 7 to produce sets of time-varying voltages which after computation gave the time varying shear stress at each position. Calculation of the errors between sets of readings in a manner similar to that described in section 7.2 showed that 98% of the readings were within 10% of their respective mean. This showed good consistency between the pulsatile flow readings.

It was found that the pulsatile flow shear stress was a direct and linear function of velocity at all positions and at all times although there was more scatter than had been observed in steady flow. Over the major part of the pulse, however, (t = 2 to 8) the mean difference between $\tau/\bar{u}$ for high and low flows was less than 10%. It was found also that in all positions the mean pulsatile shear stress was approximately equal to the same mean steady flow shear stress.

Figure 9.5 shows the time-varying shear stress (plotted as $\tau/\bar{u}$) at four positions downstream of the branch; on the inside wall at 0.2 diameters downstream and on the inside, top and bottom and outside walls at 1.6 diameters downstream. The shear stress varied approximately sinusoidally

with time at all positions and was markedly higher on the inside wall at 0.2 diameters downstream than at any other measured position. The maximum wall shear stress at the peak of the pulse at this position was $0.59\bar{u}$ dynes/sq.cm., a value fourteen times greater than the value in a similar, developed, steady flow. From this position the shear stress decreased rapidly downstream. At 1.6 diameters downstream, the value of shear stress on the inside wall was approximately 0.35 times the value at 0.2 diameters downstream. Figure 9.6 shows the wall shear stress distribution around the tube at 1.6 diameters downstream at four different times in the pulse, t = 1, 3, 5 and 7. These distributions were of the same shape as those shown in figure 9.3 for steady flow.

Comparison of the measured values of pulsatile shear stress at each time sample with values interpolated from the velocity plots as above gave varying results, In high flow, the ratio of measured wall shear stress to interpolated wall shear stress varied from 0.61 to 1.77 with a mean of 1.12. In low flow, the values varied from 0.60 to 2.05 with a mean of 1.36. The wide spread of values indicated that the shape of the velocity boundary layers varied considerably during the pulse. Thus, values of wall shear stress interpolated from velocity measurements could not in general be relied upon.

Summary

In steady flow, the wall shear stress depended directly and linearly on velocity. The relative values of wall shear stress at different positions can be summarised with reference to the steady, developed flow value as shown in table 9.1 below. In pulsatile flow, values of wall shear stress varied approximately sinusoidally with time but the mean values were the same as in a similar steady flow. Values of wall shear stress interpolated from velocity measurements could not in general be relied upon.

Diameters Downstream	Inside	Top/Bottom	Outside
0.2	10	-	0.2
1.6	4	3	1
3.7	3	2	1
∞	1	1	1

Table 9.1. Shear stress distribution.

9.3 An Estimate of Shear Stress in Arterial Branches

It was shown in equation (9-3) that the shear stress in a branch was given by:

$$\tau = C\mu\bar{u}/d$$

where C was a constant depending on the position within the branch. Comparing the values of τ to be found in blood and water, using suffices b and w respectively, and putting $\mu_b = 3.5\ \mu_w$,

$$\tau_b = 3.5\ \tau_w\ (\bar{u}/d)_b/(\bar{u}/d)_w \qquad (9\text{-}7)$$

It was found in section 9.2 that the mean pulsatile flow value of τ_w on the inside wall of the limb 0.2 diameters downstream was the same as the steady flow value of $0.42\bar{u}$ dynes/sq.cm. Inserting this into equation (9-7) together with $d_w = 1.90$ cm. gives:

$$\tau_b = 2.8\ (\bar{u}/d)_b \qquad (9\text{-}8)$$

where $(\bar{u}/d)_b$ is the value of the ratio of blood velocity to vessel diameter measured in sec^{-1}. Taking $(\bar{u}/d)_b$ to be approximately 80 per sec. for arteries (Whitmore, 1968), though it can be higher than this,

$$\bar{\tau}_b = 225 \text{ dynes/sq.cm.}$$

and $$\tau_b(\text{max}) = 320 \text{ dynes/sq.cm.}$$

Fry (1968) has estimated the 'yield stress' of blood to be between 294 and 464 dynes/sq.cm. and he notes that while momentary exposure to stresses higher than the yield stress can be tolerated, exposure for longer periods can lead to severe blood damage. It can be said therefore that the mean shear stress experienced by the blood passing close to the carina of a branch is certainly of the order of the blood yield stress as calculated by Fry (1968) and the maximum shear stress possibly higher than the yield stress. It is possible therefore that damage to blood could occur simply by its passage through a normal arterial branch. Furthermore, a small stenosis immediately prior to a branch such that the diameter narrows

only 20% would increase the mean blood velocity by 56% and increase the shear stress by a factor of two (equation (9-8)) to a level well above the blood yield stress.

9.4 Shear Stress and Vortex shedding in a Confluence

In order to be able to compare the variation of shear stresses in arteries and veins, one of the branches was reversed to form a confluence with water flowing up the two limbs to join into one stream. A system was arranged whereby the flows in both limbs were equal and both inlet velocity profiles were laminar, developed and parabolic. Measurements of wall shear stress were made at various positions around the confluence, but in no position was there found a value of wall shear stress larger than the developed steady flow value of $0.042\bar{u}$ dynes/sq.cm. Very low wall shear stress was evident in the main stream for approximately 1 cm. beyond the confluence. The distribution of wall shear stress was therefore much more uniform than in a branch and there were no areas of high shear. Contra-rotating vortices were set up by the turning action of the two streams and these persisted for some way downstream. These secondary flows, however, appeared less strong than had been observed in similar flows through a branch.

It was discovered while measuring the shear stress in the confluence in steady flows with a main stream Reynolds' number greater than 1000 that vortices were shed from the carina. i.e. the central meeting point of the

two limbs. Observations with dye showed that the vortices were formed on both sides of the carina and shed together although they tended to be shed uniformly from one side of the carina thus forming a single vortex street slightly off the tube centreline. Further observations showed that vortices were not shed when the two flowrates were equal nor when the flow in one limb substantially predominated but only when the flowrates in the two limbs were slightly different from each other. The flow in the limb with the higher flow had to be within approximately 52% to 65% of the total flow for the phenomenon to occur and the shedding frequency increased as the percentage flow increased within these limits.

The length of one of the tubes feeding the confluence was increased marginally in order to cause a small, constant imbalance in the flowrates and measurements of vortex shedding frequency were then made as the flowrate was increased. The results are presented in figure 9.7 which shows that once the mean main stream velocity was high enough (3.8 cm./sec.) for vortex shedding to begin, the shedding frequency increased linearly with mean stream velocity, the equation of the straight line giving:

$$f = 0.33\ (\bar{u} - 3.8) \qquad (9\text{-}9)$$

where f (per sec) is the shedding frequency and $\bar{u}$ the mean main stream velocity. This compares with the rate of vortex shedding behind a circular cylinder of radius R which is given by Goldstein (1938) for Reynolds' numbers greater than 1000 as:

$$f = 0.09\ \bar{u}/R \qquad (9\text{-}10)$$

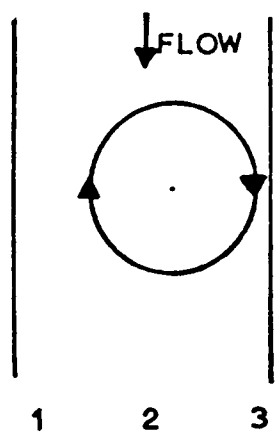
Thus although equations (9-9) and (9-10) differ by a constant term, the rate of increase with velocity of the shedding frequency from the branch carina is similar to that from a circular cylinder of radius 0.3 cm. The shape of figure 9.7 and the positive intercept on the ordinate is confirmed by Roach (1971) who has made similar observations although beginning at rather lower Reynolds' numbers.

Figures 9.8 and 9.9 show the effects of the vortex shedding on the shear stress and velocity measurements downstream. Both figures are taken directly from polaroid films of oscilloscope traces. The upper trace in figure 9.8 shows the anemometer voltage output from the shear stress probe (approximately proportional to the sixth root of shear stress) with the probe positioned in the plane of the confluence at 0.4 cm. downstream of the confluence in a main stream Reynolds' number of 1800. The lower trace shows the centreline velocity in one of the input limbs just prior to the confluence thus demonstrating the lack of any pulsing in the input flows. Both traces were taken with voltage and time scales of 0.05 volts/div. and 5 sec./div. respectively. For the velocity probe, this was equivalent to about 2 cm./sec./div. which showed that there was a maximum variation in input velocity of about 3%.

Figure 9.9 shows the anemometer voltage output from the velocity probe (approximately proportional to the

fourth root of velocity) at 1.8 cm. downstream of the confluence in a main stream Reynolds' number of 3000. (Each limb input Reynolds' number was 2000). The upper trace shows the variation in velocity close to the wall which was furthest from the vortex street. The central trace shows the velocity on the tube centreline and the lower trace the velocity close to the wall nearest to the vortex street. All measurements were in the plane of the confluence. All three traces were taken with voltage and time scales of 0.05 volts/div. (equivalent to about 2 cm./sec./div.) and 1 sec./div. respectively. It can be seen that very regular pulse-shaped variations in velocity were produced by the vortex shedding. There was the greatest variation in velocity near the walls of the main stream and least variation at the centre. The difference between the magnitudes of the two traces at the walls was caused by the vortices being shed non-centrally as described above, the larger variation being at the wall position nearest the vortex. The variations in velocity were consistent with the observations of a single vortex street. The velocity close to one wall showed a sudden increase as the vortex passed it at the same time as the velocity close to the other wall showed a sudden decrease. Reference can be made to figure 9.10 below which shows how a single vortex adds to the velocity on one side of the tube and subtracts from it on the other.

FIGURE 9.10
SHED VORTEX



A small variation in centreline velocity was evident just before the velocities near the wall were affected.

McDonald (1960) has observed a similar phenomenon of vortex shedding at a model confluence but he has made no quantitative measurements. As far as can be ascertained, no measurements in the actual venous system have shown the existence of vortices being shed from confluences and it may be that Reynolds' numbers in the venous system are low enough to preclude the phenomenon. According to Whitmore (1968), however, the Reynolds' number in the Vena Cava of a dog is 1375 which should be large enough to permit vortex shedding, at least of low frequency.

10 DISCUSSION

10.1 The formation of early atheromatic deposits

Early atheromatic deposits generally occur at branches on the outside wall (Murphy et al. 1962, Caro et al. 1971). The mechanism of the formation of these deposits is not yet understood, however, and the many theories invoke widely differing fluid mechanic and biochemical effects. Some of the theories can be examined briefly in the light of the conclusions of this study.

The theory of turbulence (Mitchell and Schwartz, 1965) is not considered generally acceptable since no turbulence was ever observed in either branch at inlet Reynolds' numbers up to 1550. In pulsatile flow, turbulence is even less likely (Schultz et al., 1969). The theory of low pressure sucking on the inside of the branch caused through Bernouilli's equation by the increase in velocity (Texon, 1960) is discounted on several grounds. In general the velocity will not increase but decrease, owing to the slight increase in cross-sectional area and even if the velocity did increase, the change in pressure would be minimal. The inside wall of the branch is also not in general a site of atheromatic deposit. (See above). This is also the objection to the theory of high shear (French, 1970) since it has been shown that high shear only occurs on the inside wall of the branch. The theories of boundary layer separation (Fox and Hugh, 1966) and of low pressure sucking on the outside of the branch (Texon, 1963) are discounted on the evidence of section 4. Although it may

appear two-dimensionally as though there is a static zone immediately after the angle on the outside of the branch, this area is in fact filled with the fluid coming over and under the main stream to form the vortices on the outside of the limb. There is thus no area of boundary layer separation or zone of low pressure. The theory of Caro et al.(1971) that plaques form in areas of low shear is acceptable to a certain extent since the areas downstream of branches where deposits are generally found are also areas of relatively low shear as was found in section 9.2. It should be noted, however, that the mean shear stress on the outside wall of the branch is only less than the developed steady flow value for one diameter downstream. Beyond this distance, the mean shear stress on the outside wall, although lower than that on the inside wall, would still be generally higher than it was in the parent tube. Therefore, if low shear was the main reason for the siting of atheromatic deposits, it would be expected that the limbs would generally be less affected than the parent tube, excepting only the very small area existing on the outside of the branch for just one diameter downstream. This is not borne out by clinical observations. (Young et al. 1960, Murphy et al. 1962, Caro et al. 1971). It is concluded, therefore, that although it can be said that deposits tend to occur in areas of lower rather than higher shear, the shear stress itself is not the main contributary factor.

French (1970) and Murphy et al.(1962) have both suggested that platelets form the initial deposits on the vessel walls. Since platelets are normally carried within the core of the blood and not in the outside of the surrounding plasma, they would not normally be in contact with the arterial walls. At curves and bends, however, the secondary velocities set up (section 4) would

convect these platelets to the walls of the vessel where they could be deposited especially in areas of low shear. In areas of high shear, such as the inside wall of the branch, they would find attachment difficult owing to the relatively large forces dragging them along. Young et al.(1960) have produced evidence to show that the major deposits occur not immediately opposite the carina but at a slight distance downstream which could possibly be the position taken up by the initial vortex formation. It is quite possible therefore that the siting of deposits is dependent on a combination of secondary velocities and relatively low shear.

The fact that atheromatic deposits occur mainly in the arterial system and seldom in the venous (e.g. British Medical Journal Editorial, April, 1971) is probably unrelated to fluid mechanics. Nevertheless, the observed reduction in secondary flow velocities in confluences, when compared with branches, and the lower Reynolds' numbers in the venous system compared to arteries (Whitmore, 1968) may be contributary factors.

10.2 Suggestions for further work

The present investigation has been carried out in one particular shape of symmetrical branch. One of the first new investigations that should be carried out is of the downstream velocity distribution in symmetrical branches with varying angles and cross-sectional area ratios in order to ascertain what effects, if any, these have on the flow patterns. Studies should also be made on non-symmetrical branches and on small tributaries leaving the main stream. Detailed study of confluences is also required, a field that is at present almost untouched. There is of the order of a thousand million branches in the circulatory system and until good and detailed knowledge of fluid flow in all shapes and sizes of branches and confluences is obtained, knowledge of the details of blood flow will also be lacking.

REFERENCES

Abbreviations:

Circ. Res.	Circulation Research.
J.	Journal.
J.Sci.Instr.	Journal of Scientific Instruments.
Proc.	Proceedings.
Proc.Roy.Soc.	Proceedings of the Royal Society.

Alexander R.S. (1954)
The influence of constrictor drugs on the distensibility of the splanchnic venous system, analysed on the basis of an aortic model.
Circ.Res.Vol.2 p.140.

Barnett C.H. and Cochrane W. (1956)
The flow of viscous liquids in branched tubes.
Nature (London). Vol.177 p.740.

Bellhouse B.J. and Bellhouse F.H. (1968)
Thin-film gauges for the measurement of velocity or skin friction in air, water or blood.
J.Sci.Instr. (J.Physics E.) Series 2. Vol.1 p.1211.

Bellhouse B.J. and Bellhouse F.H. (1969a)
Fluid mechanics of model normal and stenosed aortic valves.
Circ.Res. Vol.25 p.693.

Bellhouse B.J. and Bellhouse F.H. (1969b)
A straight needle-probe for the measurement of blood velocity.
J.Sci.Instr. (J.Physics E.) Series 2. Vol.2. p.936.

Bellhouse B.J. and Schultz D.L. (1966)
Determination of mean and dynamic skin friction, separation and transition in low-speed flow with a thin-film heated element.
J.Fluid Mechanics. Vol.24(part 2) p.379.

Brech R., Bellhouse B.J. and Bellhouse F.H. (1971)
A directionally-sensitive thin-film velocity probe.
J.Sci.Instr. (J.Physics E.) Series 2. Vol.4 p.464.

Caro C.G., Fitz-Gerald J.M. and Schroter R.C.(1971)
Atheroma and arterial wall shear.
Proc.Roy.Soc.(London) B. Vol.177 No.1046 p.109.

Clutter D.W. and Smith A.M.O. (1961)
Flow visualization by electrolysis of water.
Aerospace Engineering. Vol.20 No.1 pp.24 and 74.

Cutler S.S. and Burbank B. (1968)
Fluid control devices, rheostasis and the human circulation.
J.Thoracic and Cardiovascular Surgery. Vol.56 No.4 p.558.

Dean W.R. (1927)
Motion of fluid in a curved pipe.
Philosophical Magazine (7). Vol. 4 p.208.

Fox J.A. and Hugh A.E. (1966)
Localization of atheroma: A theory based on boundary layer separation.
British Heart J. Vol.28 p.388.

French J.E. (1970)
Atherosclerosis.
In General Pathology Ed. H.Florey. London 1970.

Fry D.L. (1968)
Acute vascular endothelial changes associated with increased blood velocity gradients.
Circ.Res. Vol. 22 p.165.

Goldstein S. (1938)
Modern developments in fluid mechanics.
Clarendon Press, Oxford.

Groat R.A. (1948)
Relationship of volumetric rate of blood flow to arterial diameter.
Fed.Proc. 1948.
Quoted in Medical Physics Vol.2. Ed. Grasser.

Hess W.R. (1927)
Die Verteilung von Querschnitt, Widerstand, Druck-gefalle und Stromungsgeschwindigkeit im Blutkreislauf.
Handb.d.normale u. path. Physiol. Bd.7, Teil 2, p.904.

Knox C.K. (1962)
An experimental investigation of the steady flow of a viscous fluid in circular, branched tubes.
MS thesis. Univ. of Minnesota.

Knudsen J.G. and Katz D.L. (1958)
Fluid dynamics and heat transfer.
McGraw-Hill.

Langhaar H.L. (1942)
Steady flow in the transition length of a straight tube.
J.Applied Mechanics. June 1942. p.A-55.

Li W.H. and Lam S.H. (1964)
Principles of Fluid Mechanics.
Addison-Wesley, Mass.

McConalogue D.J. and Srivastava R.S. (1968)
Motion of a fluid in a curved tube.
Proc.Roy.Soc. A. Vol. 307 p.37.

McDonald D.A. (1960)
Blood flow in arteries.
Edward Arnold Ltd., London.

Mitchell J.R.A. and Schwartz C.J. (1965)
Arterial disease.
Blackwell Scientific Publications, Oxford.

Murphy E.A., Rowsell H.C., Downie H.G., Robinson G.A. and Mustard J.F. (1962)
Encrustation and atherosclerosis.
Canadian Medical Association J. Vol.87. p.259.

Murray C.D. (1926a)
The physiological principle of minimum work.
Proc.National Academy of Science. Vol.12 p.207.

Murray C.D. (1926b)
The physiological principle of minimum work applied to the angle of branching of arteries.
J.General Physiology. Vol.9 p.836.

Nikuradse J. (1934)
In Applied Hydro- and Aeromechanics. Prandtl L. and Tietjens O.G.
McGraw-Hill. 1934. p.27.

Pedley T.J., Schroter R.C. and Sudlow M.F. (1971)
Flow and pressure drop in systems of repeatedly branching tubes.
J.Fluid Mechanics. Vol.46(part 2) p.365.

Pope R.J. (1971)
The use of thin-film heated elements in water flows.
D.Phil.thesis, Univ. of Oxford.

Roach M. (1971)
Professor M.Roach, London, Ontario.
Private Communication.

Sandler M. and Bourne G.H. (1963)
Atherosclerosis and its origin.
Academic Press, New York.

Schroter R.C. and Sudlow M.F. (1969)
Flow patterns in models of the human bronchial airways.
Respiration Physiology. Vol.7 p.341.

Schreck R.M. and Mockros L.F. (1970)
Fluid dynamics in the upper pulmonary airways.
Presented at the American Institute of Aeronautics and Astronautics 3rd. Fluid and Plasma Dynamics Conference, Los Angeles.
AIAA Paper 70-788.

Schultz D.J., Tunstall-Pedoe D.S., Lee G.de J., Gunning A.J. and Bellhouse B.J. (1969)
Velocity distribution and transition in the arterial system.
In CIBA Foundation Symposium on Circulatory and Respiratory Mass Transport.

Stedman (1961)
Stedman's Medical Dictionary.
E. and S. Livingstone Ltd., Edinburgh.

Stehbens W.E. (1959)
Turbulent blood flow.
Quarterly J. of Experimental Physiology. Vol.44 p.110.

Texon M. (1960)
The hemodynamic concept of atherosclerosis.
Bulletin of the New York Academy of Medicine.
Vol.36 p.263.

Texon M. (1963)
The role of vascular dynamics in the development of atherosclerosis.
In Sandler and Bourne (above) p.167.

Whitmore R.L. (1968)
Rheology of the Circulation.
Pergamon Press.

Womersley J.R. (1955)
Method for the calculation of velocity, rate of flow and viscous drag in arteries when the pressure gradient is known.
J.Physiology. Vol.127 p.553.

Young W., Gofman J.W., Tandy R., Malamud N. and Waters E.S.G.
The Quantitation of atherosclerosis.
American J. of Cardiology. Vol.6 p.288.

APPENDIX ONE ALGOL COMPUTER PROGRAM

PULSATILE FLOW ANALYSIS OF VELOCITY PROFILES

```
FAEBE BR P4 APU
PULSATILE FLOW PROCESSING;
SAVE;
TL1200;→

begin real array X[0:13], Y[0:13],v[1:12], x[1:64], y[1:64],
                 z[1:40], u[1:12,1:8], um[1:64], ar[1:8],br[1:8],
                 cr[1:8],dr[1:8];
      integer ID,K,I,i,j,k,l,e,f,h,m,n,p,L,W,f1,f2,f3,f4,f5,f6,f7;
      real q,r,a,b,c,d,A,B,C,D,E,F,G,H,J,Q,S,R,T,U,DR,DR1,
           DR2,DYDX,cs,sn,M0,M1X,M1Y,M1R,M2X,M2Y,M2,M3X,M3Y;
      library A6,A12,A30,G0,G1;
      procedure circle(x,y,r); value x,y,r; real x,y,r;
                000300(60,x,y,r);

f1:=format([dds]); f2:=format([sdd.dds]); f3:=format([7sdd]);
f4:=format([3s-dd.dd]); f5:=format([3s-dd.ddc]);
f6:=format([4s+dd.ddd]); f7:=format([4sdd.dddc]);
open(20);
ID:=read(20); n:=read(20); Q:=read(20); p:=read(20); I:=read(20);
 K:=read(20); A:=read(20); B:=read(20); C:=read(20); D:=read(20);
 E:=read(20); F:=read(20); G:=read(20); H:=read(20); J:=read(20);
begin real array  V[1:I,1:12,1:8+K], M[1:I,1:9];
open(30); a:=0; b:=0; c:=0;
for l:= 1 step 1 until 8 do
begin DR1:=read(20);
      for j:=1 step 1 until 12 do
      for k:=9 step 1 until 8+K do
      for i:=1 step 1 until I do V[i,j,k]:=0.0001×(read(20));
      DR2:=read(20);
      for j:=1 step 1 until 12 do
      for k:=9 step 1 until 8+K do
      for i:=1 step 1 until I do
      begin DR:=DR1+(DR2-DR1)×(j-1)/11;
            V[i,j,k]:=((V[i,j,k])↑2)/DR;
            V[i,j,k]:=(if V[i,j,k]>G then ((V[i,j,k]-B)/A)↑2
                       else if V[i,j,k]>F then
                       (((D↑2+4×C×(V[i,j,k]-E))↑0.5-D)/(2×C))↑2
                       else ((V[i,j,k]-J)/H));
      end;
      for i:=1 step 1 until I do
      for j:=1 step 1 until 12 do
      begin S:=0; f:=0;
            for k:=9 step 1 until 8+K do
            begin if V[i,j,k]>0 and V[i,j,k]<30 then
                  begin S:=S + V[i,j,k];
                        f:=f+1;
                  end;
                  if V[i,j,k]<0 or V[i,j,k]>30 then
                  begin writetext(30,[[c]]);
                        write(30,f1,i); write(30,f1,j);
                        write(30,f1,k); write(30,f1,l);
                        writetext(30,[DATA*ERROR[2c]]);
                  end;
            end;
```

```
                V[i,j,l]:=S/f; h:=f;
                if V[i,j,l]>2 then
                begin for k:=9 step 1 until 8+K do
                      begin if V[i,j,k]>0 and V[i,j,k]<30 then
                            begin R:=(V[i,j,k]-V[i,j,l])/V[i,j,l];
                                  if abs(R)>0.25 then
                                  begin S:=S-V[i,j,k];h:=h-1; end;
                            end;
                      end;
                      if h>0 then V[i,j,l]:=S/h;
                      if h<K then write(30,format([d]),h);
                end;
                for k:=9 step 1 until 8+K do
                begin R :=(V[i,j,k]-V[i,j,l])/V[i,j,l];
                      if abs(R)<0.05 then a:=a+1;
                      if abs(R)<0.1  then b:=b+1;
                      if abs(R)<0.15 then c:=c+1;
                end;
          end;
    end;
A:=read(20);
close(20);
writetext(30,[[3cl]);
open(10);
for i:= 1 step 1 until I do
begin M[i,9]:=0;
      for l:= 1 step 1 until 8 do
      begin M[i,l]:=(1/2)x(V[i,6,l]+V[i,7,l]);
            M[i,9]:=M[i,9]+M[i,l];
      end;
      M[i,9]:=M[i,9]/8;
end;
for i:= 1 step 1 until I do
for j:= 1 step 1 until 12 do
for l:= 1 step 1 until 8 do V[i,j,l]:=(M[i,9]/M[i,l])xV[i,j,l];
write(30,f1,-3);
writetext(30,[CM*DOWNSTREAM*OF*BRANCH*1]); write(30,f1,n);
writetext(30,[[2c]CHECK*99*EQUALS*1]); write(30,f1,A);
f:=96xIxK;
a:=100xa/f; b:=100xb/f; c:=100xc/f;
writetext(30,[[2c]1]);
write(30,f1,a); writetext(30,[PER*CENT*OF*READINGS*ARE*
WITHIN*5*PER*CENT*OF*THE*MEAN[c]1]);
write(30,f1,b); writetext(30,[PER*CENT*OF*READINGS*ARE*
WITHIN*10*PER*CENT*OF*THE*MEAN[c]1]);
write(30,f1,c); writetext(30,[PER*CENT*OF*READINGS*ARE*
WITHIN*15*PER*CENT*OF*THE*MEAN[c]1]);

for i:= 1 step 1 until I do
begin
writetext(30,[[4c]I*EQUALS*1]); write(30,f1,i);
writetext(30,[[2c]MEAN*CENTRELINE*VELOCITY*IS[1]);
write(30,f2,M[i,9]); writetext(30,[[3cs]m/s]);
for j:= 1 step 1 until 12 do write(30,f3,j);
writetext(30,[[2s]CENT.VEL[2c]-[2c]1]);
for l:= 1 step 1 until 8 do
begin write(30,f1,-7);
      for j:= 1 step 1 until 12 do write(30,f4,V[i,j,l]);
      write(30,f5,M[i,l],-1);
end;
writetext(30,[[3c]1]);
```

```
for j:= 1 step 1 until 12 do
for l:= 1 step 1 until 8  do u[j,l]:=V[i,j,l];
for l:= 1 step 1 until 8 do
begin ar[l]:= (1/24)x(6xu[11,l]+4xu[10,l]+2xu[9,l]);
      br[l]:= (1/24)x(6xu[2,l] +4xu[3,l] +2xu[4,l]);
      cr[l]:= (1/38)x(u[10,l]+6xu[9,l]+6xu[8,l]+
                      5.25xu[7,l]+0.75xu[6,l]);
      dr[l]:= (1/38)x(u[3,l] +6xu[4,l]+6xu[5,l]+
                      5.25xu[6,l]+0.75xu[7,l]);
end;
for l:= 1 step 1 until 8 do
begin DYDX:= (u[12,l]-u[11,l])/(-0.75);
      A:= 0.25xDYDX-0.25xu[12,l]+0.25xDYDX;
      B:= -DYDX+u[12,l];
      u[12,l]:=(25/16)xA+(5/4)xB;
end;

um[1] :=0.25x(u[12,5]+u[12,8]); um[2] :=0.25x(u[12,8]+u[12,7]);
um[3] :=0.25x(u[12,7]+u[12,6]); um[4] :=0.25x(u[12,6]+u[1,1]);
um[5] :=0.25x(u[1,1]+u[1,2]);   um[6] :=0.25x(u[1,2]+u[1,3]);
um[7] :=0.25x(u[1,3]+u[1,4]);   um[8] :=0.25x(u[1,4]+u[1,5]);
um[9] :=0.25x(u[1,5]+u[1,8]);   um[10]:=0.25x(u[1,8]+u[1,7]);
um[11]:=0.25x(u[1,7]+u[1,6]);   um[12]:=0.25x(u[1,6]+u[12,1]);
um[13]:=0.25x(u[12,1]+u[12,2]); um[14]:=0.25x(u[12,2]+u[12,3]);
um[15]:=0.25x(u[12,3]+u[12,4]); um[16]:=0.25x(u[12,4]+u[12,5]);

um[17]:=um[1] +0.25x(u[11,5]+u[11,8]);
um[18]:=um[2] +0.25x(u[11,8]+u[11,7]);
um[19]:=um[3] +0.25x(u[11,7]+u[11,6]);
um[20]:=um[4] +0.25x(u[11,6]+u[2,1]);
um[21]:=um[5] +0.25x(u[2,1]+u[2,2]);
um[22]:=um[6] +0.25x(u[2,2]+u[2,3]);
um[23]:=um[7] +0.25x(u[2,3]+u[2,4]);
um[24]:=um[8] +0.25x(u[2,4]+u[2,5]);
um[25]:=um[9] +0.25x(u[2,5]+u[2,8]);
um[26]:=um[10]+0.25x(u[2,8]+u[2,7]);
um[27]:=um[11]+0.25x(u[2,7]+u[2,6]);
um[28]:=um[12]+0.25x(u[2,6]+u[11,1]);
um[29]:=um[13]+0.25x(u[11,1]+u[11,2]);
um[30]:=um[14]+0.25x(u[11,2]+u[11,3]);
um[31]:=um[15]+0.25x(u[11,3]+u[11,4]);
um[32]:=um[16]+0.25x(u[11,4]+u[11,5]);

um[33]:=ar[5]+ar[8]; um[34]:=ar[8]+ar[7];
um[35]:=ar[7]+ar[6]; um[36]:=ar[6]+br[1];
um[37]:=br[1]+br[2]; um[38]:=br[2]+br[3];
um[39]:=br[3]+br[4]; um[40]:=br[4]+br[5];
um[41]:=br[5]+br[8]; um[42]:=br[8]+br[7];
um[43]:=br[7]+br[6]; um[44]:=br[6]+ar[1];
um[45]:=ar[1]+ar[2]; um[46]:=ar[2]+ar[3];
um[47]:=ar[3]+ar[4]; um[48]:=ar[4]+ar[5];

um[49]:=cr[5]+cr[8]; um[50]:=cr[8]+cr[7];
um[51]:=cr[7]+cr[6]; um[52]:=cr[6]+dr[1];
um[53]:=dr[1]+dr[2]; um[54]:=dr[2]+dr[3];
um[55]:=dr[3]+dr[4]; um[56]:=dr[4]+dr[5];
um[57]:=dr[5]+dr[8]; um[58]:=dr[8]+dr[7];
um[59]:=dr[7]+dr[6]; um[60]:=dr[6]+cr[1];
um[61]:=cr[1]+cr[2]; um[62]:=cr[2]+cr[3];
um[63]:=cr[3]+cr[4]; um[64]:=cr[4]+cr[5];
```

```
for k:=1 step 1 until 64 do
begin  A:=(if k÷17=0 then 8.864 else if k÷33=0 then 7.472 else
            if k÷49=0 then 5.734 else 2.375);
       x[k]:=A×cos((78.75-22.5×(k-1))×0.017453);
       y[k]:=A×sin((78.75-22.5×(k-1))×0.017453);
end;
writetext(30,[VALUES*OF*MEAN*VELOCITY*FOR*EACH*AREA[2c]]);
for k:=1 step 1 until 64 do
begin write(30,f3,k); write(30,if k÷4=k/4 then f5 else f4,um[k]);
      write(10,format([dd.dd;c]),um[k]);
end;
writetext(30,[[2c]]);
M0:=0; M1X:=0; M1Y:=0; M2:=0; M3X:=0; M3Y:=0; M2X:=0; M2Y:=0;
for k:=1 step 1 until 64 do
begin M0:=M0+um[k];
      M1X:=M1X+um[k]×x[k];
      M1Y:=M1Y+um[k]×y[k];
end;
M0:=M0×4.43; M1X:=(M1X×4.43)/M0; M1Y:=(M1Y×4.43)/M0;
for k:=1 step 1 until 64 do
begin M2X:=M2X+((x[k]-M1X)↑2)×um[k];
      M2Y:=M2Y+((y[k]-M1Y)↑2)×um[k];
end;
M2X:=(M2X×4.43)/M0; M2Y:=(M2Y×4.43)/M0;
M2:=(M2X+M2Y);
for k:=1 step 1 until 64 do
begin M3X:=M3X+((x[k]-M1X)↑2+(y[k]-M1Y)↑2)×x[k]×um[k];
      M3Y:=M3Y+((x[k]-M1X)↑2+(y[k]-M1Y)↑2)×y[k]×um[k];
end;
M3X:=(M3X×4.43)/M0; M3Y:=(M3Y×4.43)/M0;
M0:=M0/100;
M1R:=(M1X↑2+M1Y↑2)↑0.5;
writetext(30,[[7s]M0[8s]M1X[8s]M1Y[8s]M1R[8s]M2X[8s]M2Y
                [9s]M2[8s]M3X[8s]M3Y[8s]M2C[7s]M3C[2c]]);
write(30,f6,M0); write(30,f6,M1X); write(30,f6,M1Y);
write(30,f6,M1R);write(30,f6,M2X); write(30,f6,M2Y);
write(30,f6,M2); write(30,f6,M3X); write(30,f6,M3Y);
M2:=(M2↑0.5)/9.5;
M3X:=((M3X↑2+M3Y↑2)↑(1/6))/9.5;
write(30,f6,M2); write(30,f7,M3X);
writetext(30,[[4c]]);


incplt(1); cms;
crset(4);
L:=ID÷10; W:=ID-10×L;
limits(0,21,0,27);
region(1,20,3,22);
circle(10.5,12.5,9.5);
point(10.5,3); join(10.5,22); point(1,12.5); join(20,12.5);
plotas(17,2.5,[CM/SEC]); plotas(5,26.5,[VELOCITY*PLAN*]);
typenc(L); typenc(W);
typeas([*CM.*DOWNSTREAM *OF*BRANCH*]); typenc(n);
plotas(2,25.3,[I*EQUALS*]);
if i<10 then typenc(i);
if i>9  then begin L:=i-10; typenc(1); typenc(L); end;
plotas(13,24.5,[FLOWRATE:******ML/SEC]);
plotas(2,24.5,[SCALE:***10:1]);
mspace; region(-9.5,9.5,-9.5,9.5);
```

```
for e:=p step 1 until 12 do
begin v[e]:=e/Q;
h:=0; for l:= 1 step 1 until 8 do
begin for j:= 1 step 1 until 11 do
      begin X[j]:=(if l÷6=0 then (19.25-1.5xj) else (1.5xj-0.25));
            Y[j]:=Y[i,j,l];
      end;
      X[0]:=(if l÷6=0  then 19.0 else 0.0);
      X[12]:=(if l÷6=0 then 2.0 else 17.0);
      X[13]:=(if l÷6=0 then 0.0 else 19.0);
      Y[0]:=0; Y[13]:=0; Y[12]:=Y[i,12,l];
      DYDX:=(Y[12]-Y[11])/(X[12]-X[11]);
      R:=((X[12]-X[13])xDYDX-Y[12])/((X[12]-X[13])↑2);
      T:=DYDX-2xRxX[12];
      U:=-Rx(X[13])↑2 - TxX[13];

      for j:=0 step 1 until 11 do
      begin if l=1 then cs:=1.0;    if l=2 then cs:=0.9239;
            if l=3 then cs:=0.7071; if l=4 then cs:=0.3827;
            if l=5 then cs:=0.0;    if l=6 then cs:=0.9239;
            if l=7 then cs:=0.7071; if l=8 then cs:=0.3827;
            sn:=(1-cs↑2)↑0.5;
            if l÷6=0 then
            begin if Y[j]< v[e] and Y[j+1]> v[e] then
            begin h:=h+1;
            z[h]:=X[j+1]+(Y[j+1]-v[e])x(X[j]-X[j+1])/(Y[j+1]-Y[j]);
            x[h]:=(z[h]-9.5)xcs;
            y[h]:=(9.5-z[h])xsn;
            end;
            if Y[j]> v[e] and Y[j+1]< v[e] then
            begin h:=h+1;
            z[h]:=X[j]-(Y[j]-v[e])x(X[j]-X[j+1])/(Y[j]-Y[j+1]);
            x[h]:=(z[h]-9.5)xcs;
            y[h]:=(9.5-z[h])xsn;
            end;
            if Y[j+1]= v[e] then
            begin h:=h+1;
            z[h]:=X[j+1];
            x[h]:=(z[h]-9.5)xcs;
            y[h]:=(9.5-z[h])xsn;
            end;
            end;
            if l÷6=1 then
            begin if Y[j]< v[e] and Y[j+1]> v[e] then
            begin h:=h+1;
            z[h]:=X[j+1]-(Y[j+1]-v[e])x(X[j+1]-X[j])/(Y[j+1]-Y[j]);
            x[h]:=(z[h]-9.5)xcs;
            y[h]:=(z[h]-9.5)xsn;
            end;
            if Y[j]> v[e] and Y[j+1]< v[e] then
            begin h:=h+1;
            z[h]:=X[j]+(Y[j]-v[e])x(X[j+1]-X[j])/(Y[j]-Y[j+1]);
            x[h]:=(z[h]-9.5)xcs;
            y[h]:=(z[h]-9.5)xsn;
            end;
            if Y[j+1]=v[e] then
            begin h:=h+1;
            z[h]:=X[j+1];
            x[h]:=(z[h]-9.5)xcs;
            y[h]:=(z[h]-9.5)xsn;
            end;
            end;
      end;
end;
```

```
        if (T↑2+4×R×(v[e]-U))>-0.00001 then
        begin q:=(-T+(T↑2+4×R×(v[e]-U))↑0.5)/(2×R);
              r:=(-T-(T↑2+4×R×(v[e]-U))↑0.5)/(2×R);
              if l÷6=0 then
              begin if q<X[12] and q>X[13] then
                    begin h:=h+1;
                          x[h]:=(q-9.5)×cs;
                          y[h]:=(9.5-q)×sn;
                    end;
                    if r<X[12] and r>X[13] then
                    begin h:=h+1;
                          x[h]:=(r-9.5)×cs;
                          y[h]:=(9.5-r)×sn;
                    end;
              end;
              if l÷6=1 then
              begin if q>X[12] and q<X[13] then
                    begin h:=h+1;
                          x[h]:=(q-9.5)×cs;
                          y[h]:=(q-9.5)×sn;
                    end;
                    if r>X[12] and r<X[13] then
                    begin h:=h+1;
                          x[h]:=(r-9.5)×cs;
                          y[h]:=(r-9.5)×sn;
                    end;
              end;
        end;
end;
```

```
if h>0 then
begin writetext(30,[m[8s]x[8s]y[2c]]);
      for m:= 1 step 1 until h do
      begin write(30,f1,m); write(30,f4,x[m]);write(30,f5,y[m]);
      end;
      crset(4); crsize(.4);
      if e=1 then ptplot(x,y,1,h,59);
      if e=2 then ptplot(x,y,1,h,54);
      if e=3 then ptplot(x,y,1,h,56);
      if e=4 then ptplot(x,y,1,h,50);
      if e=5 then ptplot(x,y,1,h,51);
      if e=6 then ptplot(x,y,1,h,52);
      if e=7 then ptplot(x,y,1,h,53);
      if e=8 then ptplot(x,y,1,h,60);
      if e=9 then ptplot(x,y,1,h,61);
      if e=10then ptplot(x,y,1,h,55);
      if e=11then ptplot(x,y,1,h,57);
      if e=12then ptplot(x,y,1,h,58);
end;
writetext(30,[U*EQUALS*]); write(30,f2,v[e]);
writetext(30,[H* EQUALS*]); write(30,f1,h);
writetext(30,[[3c]]);
end;
frame;
end;
close(30); close(10); incplt(0); grend;
end;
end→
```

APPENDIX ONE(a) ALGOL COMPUTER PROGRAM

In order to obtain graphical plots of velocity against position for each traverse, the following routine should be inserted in the computer program shown in Appendix One after the routine for the calculation of the distribution moments.

```
incplt(1); cms;
limits(0,21,0,27.7);
for l:=1 step 1 until 8 do
begin if l÷5=0 then begin a:=28.2 -7×l;b:=34.2-7×l;c:=1;d:=9;
                    end;
      if l÷5=1 then begin a:=56.2 -7×l;b:=62.2-7×l;c:=11;d:=19;
                    end;
      incplt(1); region(c,d,a,b);
      plotas((c+0.3),(b-0.4),[u]);
      point(c,a); join(d,a); join(d,b); point(c,a); join(c,b);
      for f:=1 step 1 until 6 do
      begin point((c-0.2),(a+f)); line(0.4,0);
      end;
      point((c+4),a); line(0,0.3);
      if Q=1 then
      begin
      plotas((c-0.5),(a+1),[2]);
      plotas((c-0.5),(a+2),[4]);
      plotas((c-0.5),(a+3),[6]);
      plotas((c-0.5),(a+4),[8]);
      plotas((c-0.8),(a+5),[10]);
      plotas((c-0.8),(a+6),[12]);
      end;

      if Q≠1 then
      begin
      plotas((c-0.5),(a+1),[1]);
      plotas((c-0.5),(a+2),[2]);
      plotas((c-0.5),(a+3),[3]);
      plotas((c-0.5),(a+4),[4]);
      plotas((c-0.5),(a+5),[5]);
      plotas((c-0.5),(a+6),[6]);
      end;
      if l=1 then plotas ((c+4.0),(a+0.7), [0]);
      if l=2 then plotas ((c+3.7),(a+0.7),[22.5]);
      if l=3 then plotas ((c+3.8),(a+0.7),[45]);
      if l=4 then plotas ((c+3.7),(a+0.7),[67.5]);
      if l=5 then plotas ((c+3.8),(a+0.7),[90]);
      if l=6 then plotas ((c+3.5),(a+0.7),[-22.5]);
      if l=7 then plotas ((c+3.8),(a+0.7),[-45]);
      if l=8 then plotas ((c+3.5),(a+0.7),[-67.5]);
      mspace;
      if Q≠1 then region(0,19,0,6);
      if Q=1 then region(0,19,0,12);
      X[0]:=(if l÷6=0 then 19.0 else 0.0);
      X[12]:=(if l÷6=0 then 2.0 else 17.0);
      X[13]:=(if l÷6=0 then 0.0 else 19.0);
      Y[0]:=0; Y[13]:=0; Y[12]:=V[i,12,1];
      for j:=1 step 1 until 11 do
      begin X[j]:=(if l÷6=0 then (19.25-1.5×j)else(1.5×j-0.25));
            Y[j]:=V[i,j,1];
      end;
      crset(4); crsize(.2); grphpt(X,Y,0,13,53);
end;
```

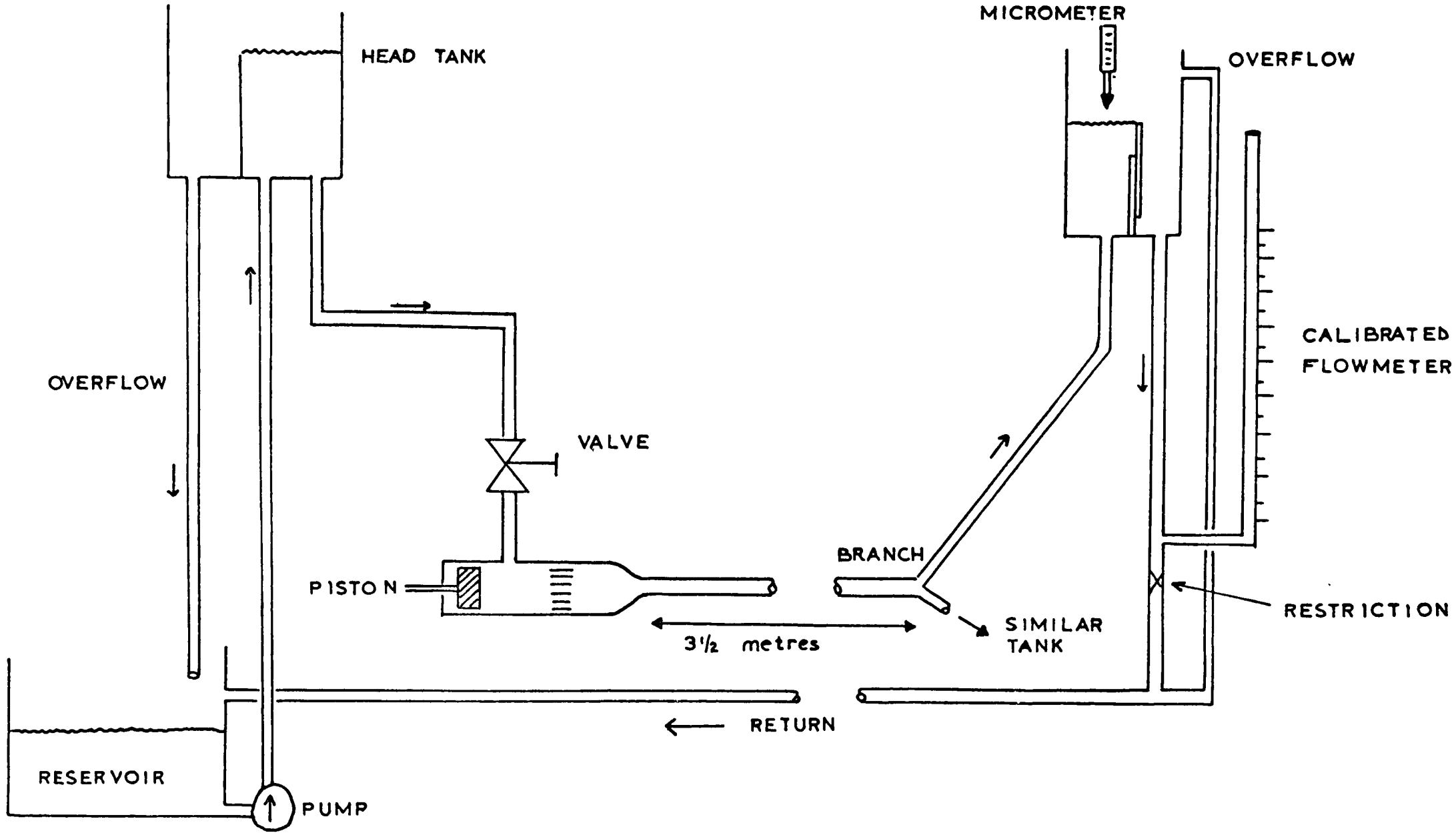


FIGURE 1·1

EXPERIMENTAL LAYOUT

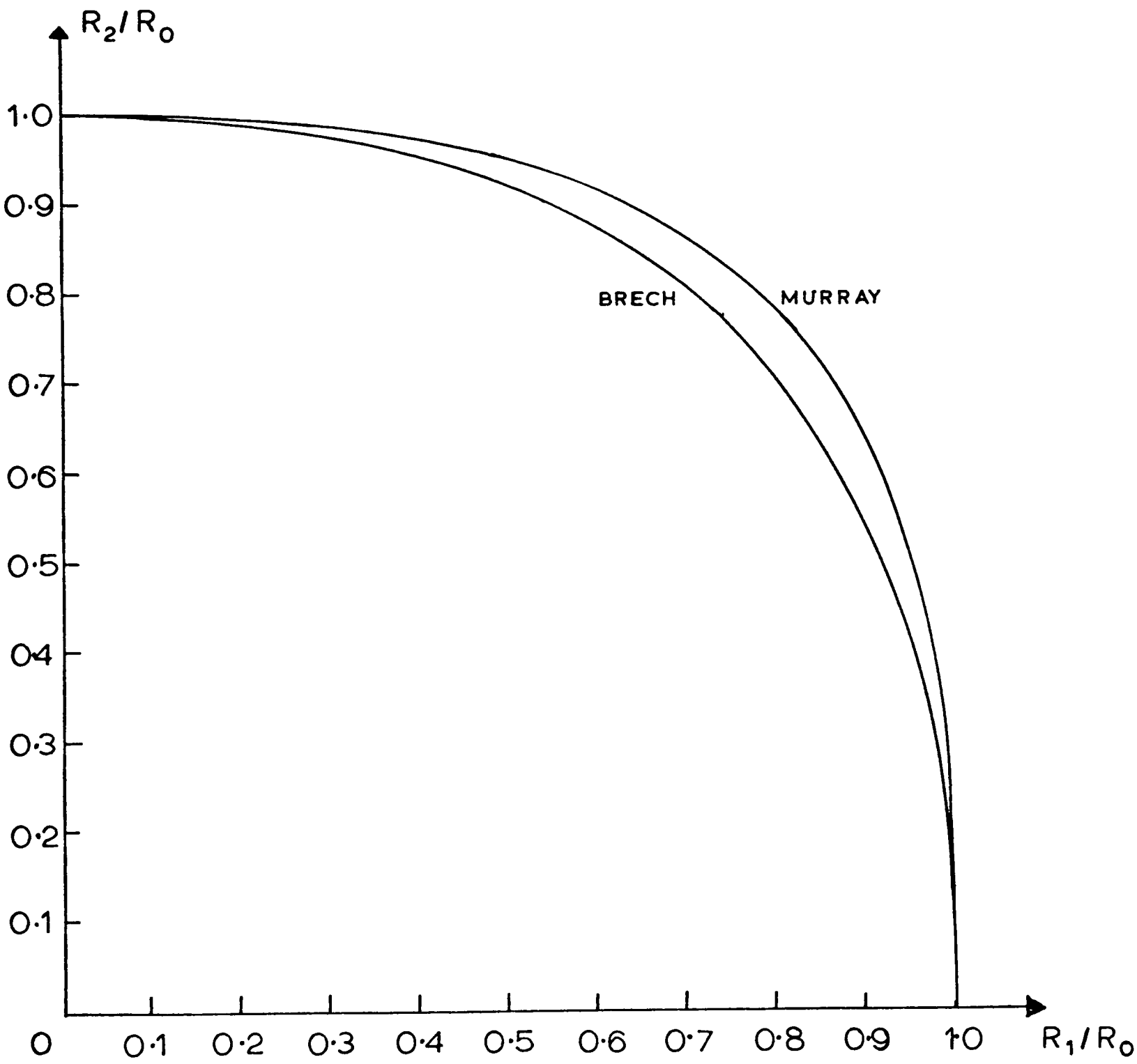


FIGURE 2.2

LIMB RADII RATIOS

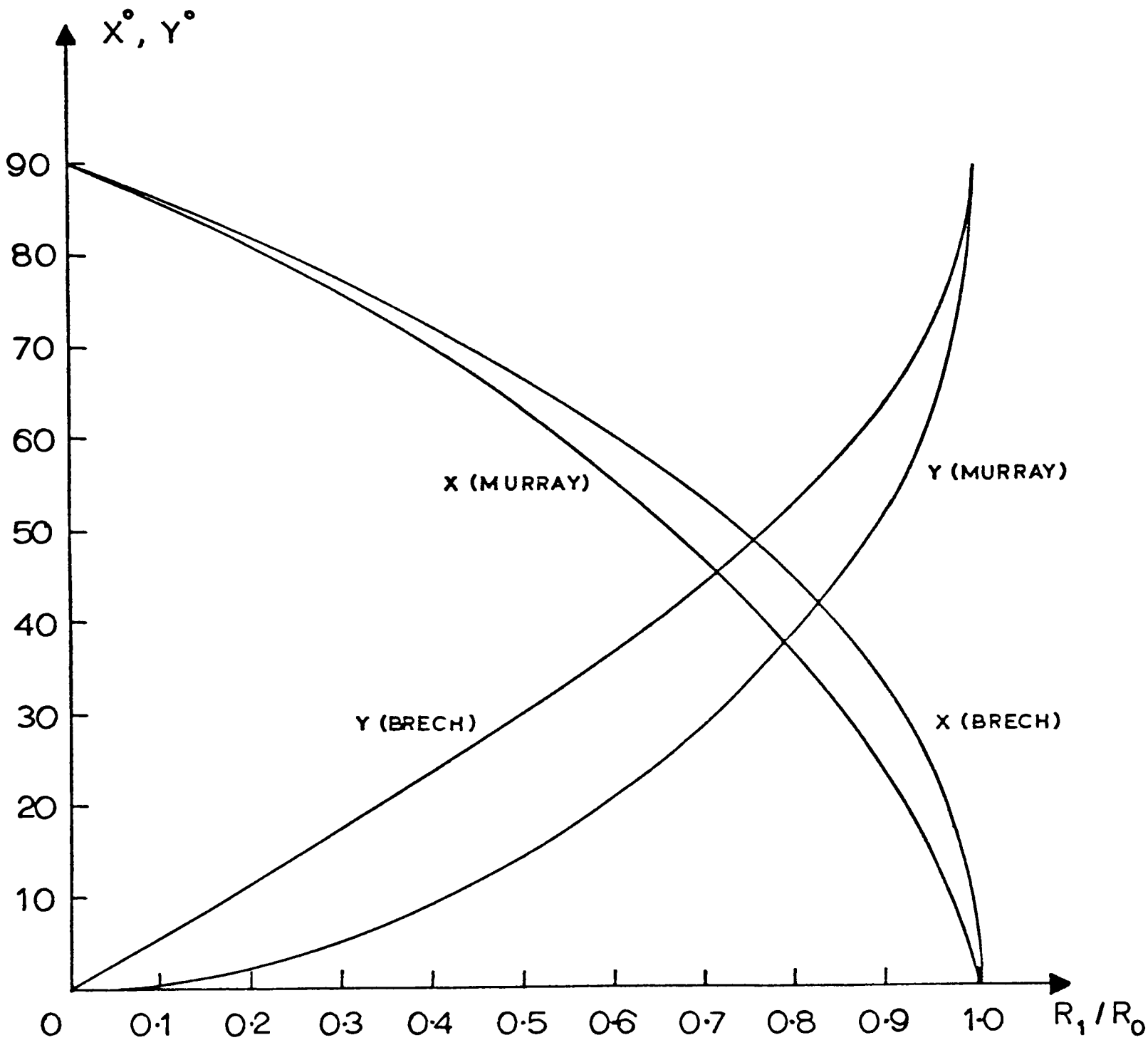
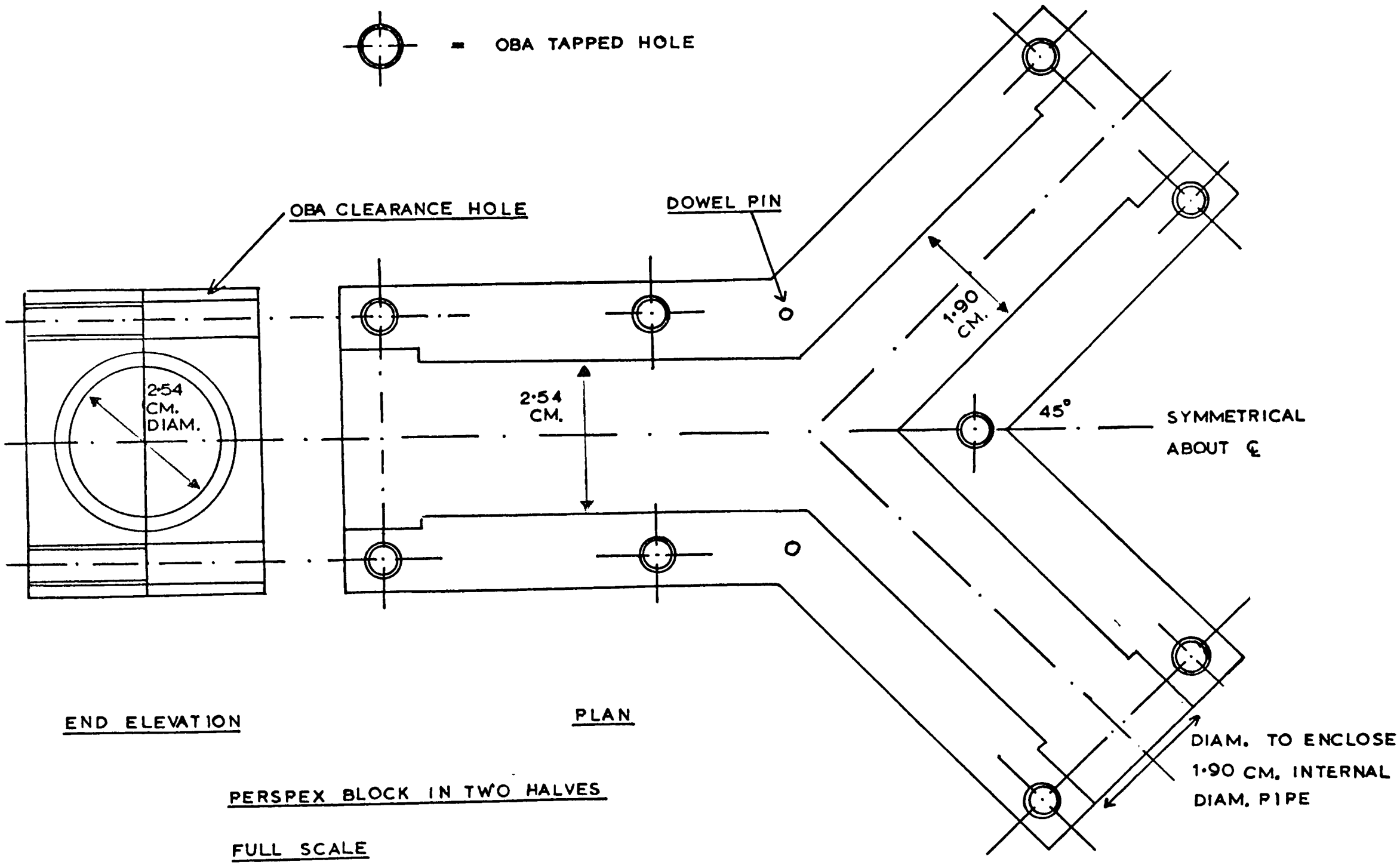


FIGURE 2.3

BRANCH ANGLE V. RADIUS RATIO

FIGURE 2·4

BRANCH NO 1



PERSPEX BLOCK IN TWO HALVES

FULL SCALE

= OBA TAPPED HOLE

OBA CLEARANCE HOLE

DOWEL PIN

2·54 CM. DIAM.

2·54 CM.

1·90 CM.

45°

SYMMETRICAL ABOUT ℄

5·0 CM. RADIUS CURVATURE

DIAM. TO ENCLOSE 1·90 CM. INTERNAL DIAM. PIPE

END ELEVATION

PLAN

PERSPEX BLOCK IN TWO HALVES

FULL SCALE

FIGURE 2.5

BRANCH NO. 2

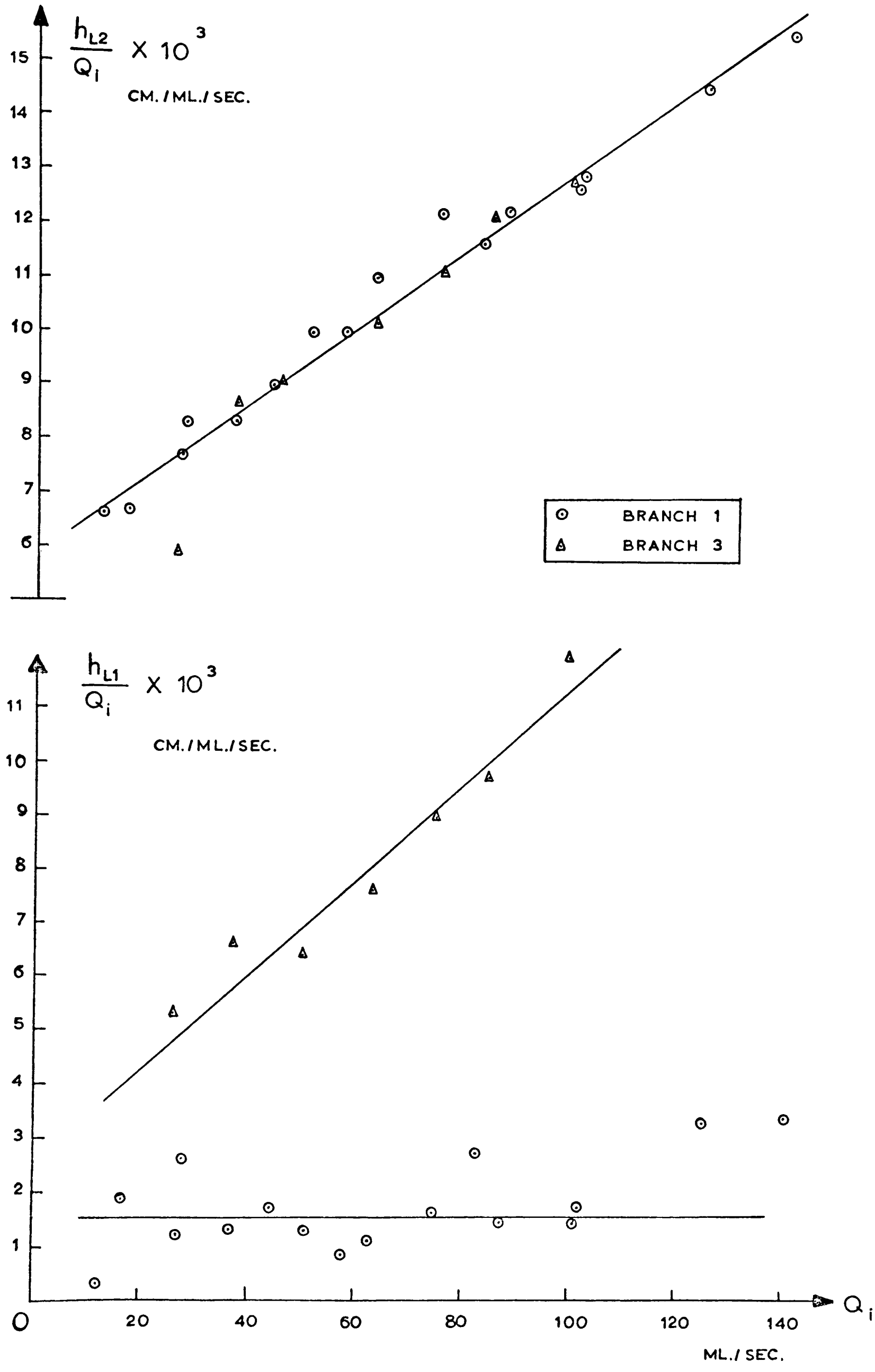


FIGURE 3.1. $\frac{h_L}{Q_i}$ V. Q_i

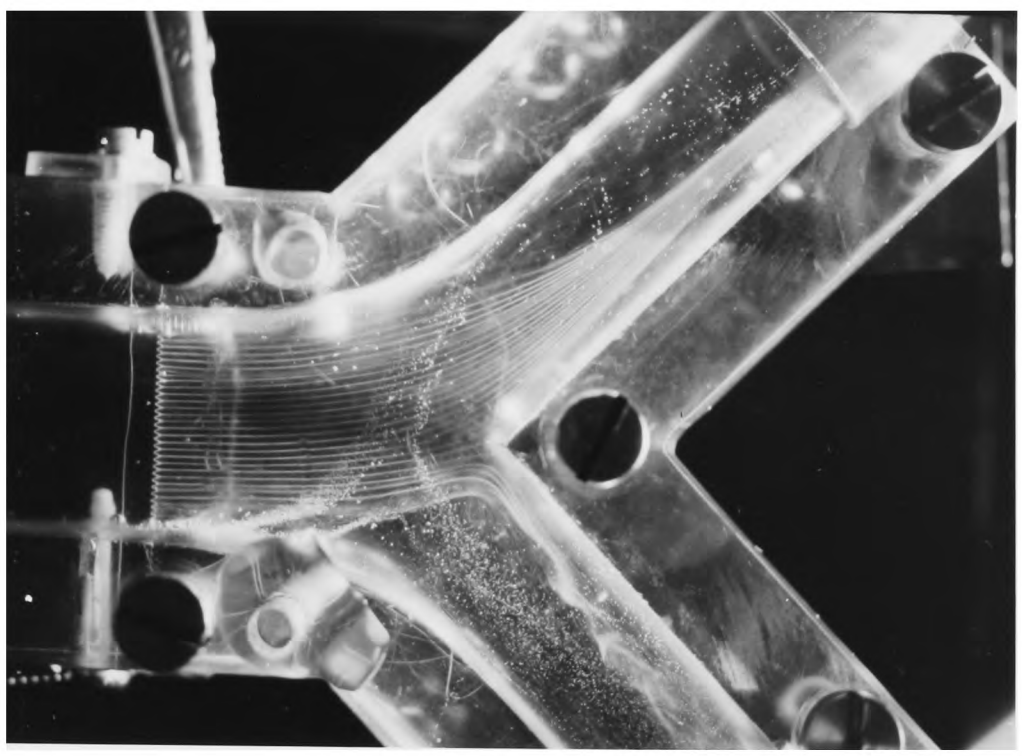


Figure 3.2. Flow 90% switched.

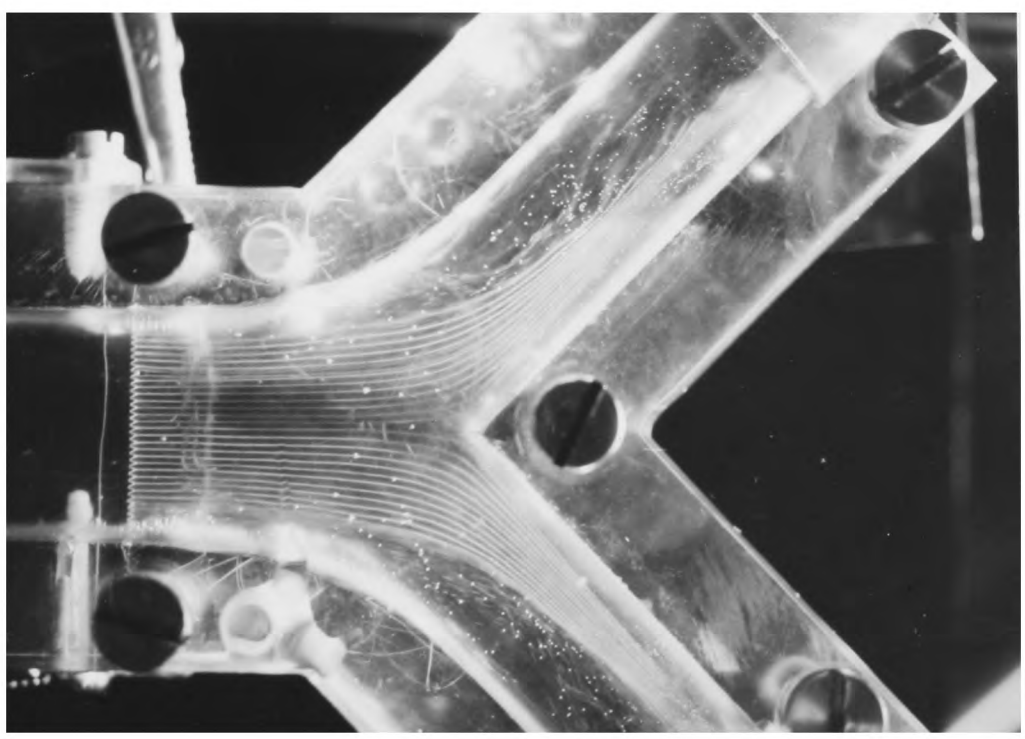
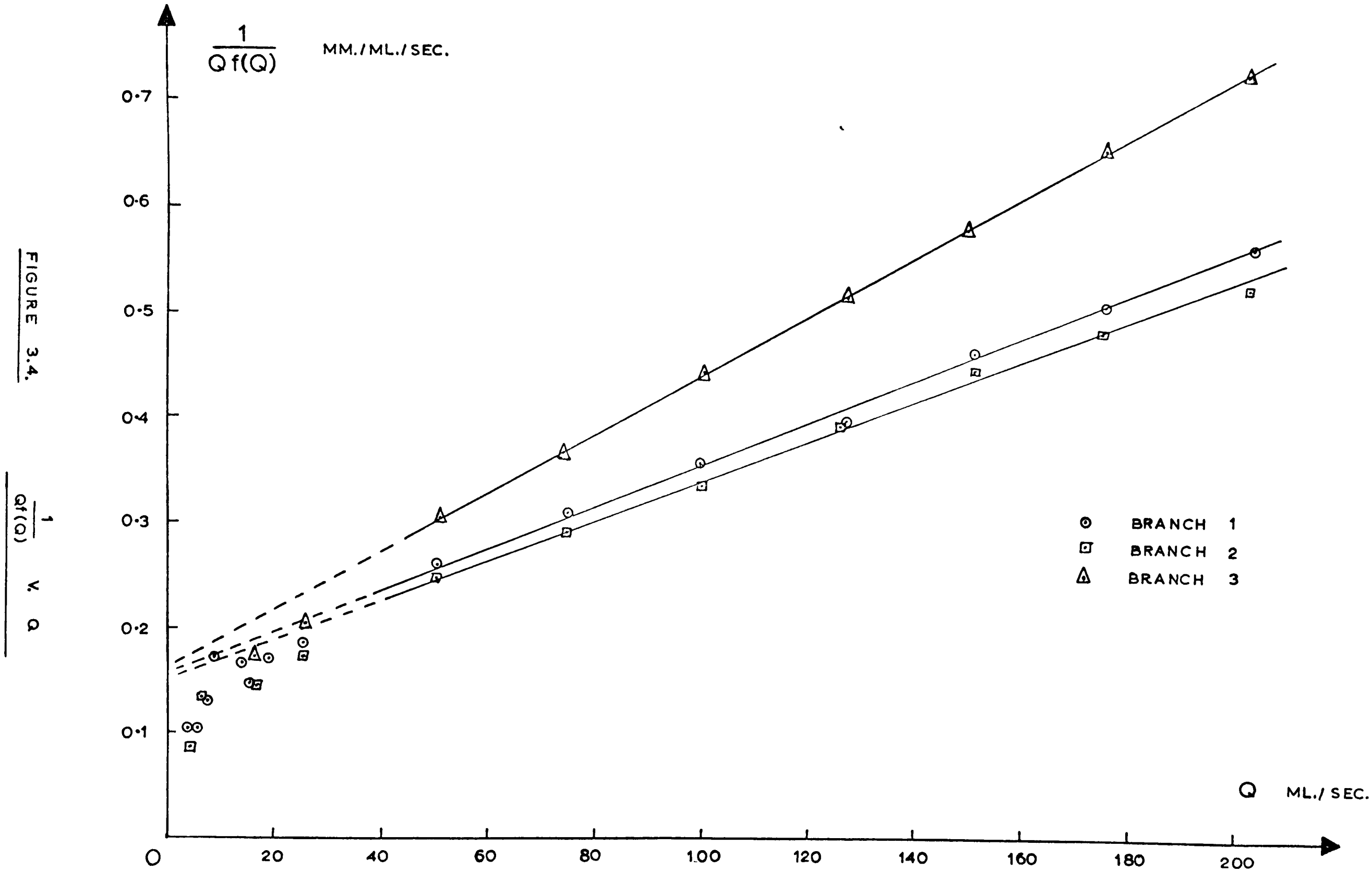


Figure 3.3. Equiflow.

FIGURE 3.4.



1/Q f(Q) Vs Q

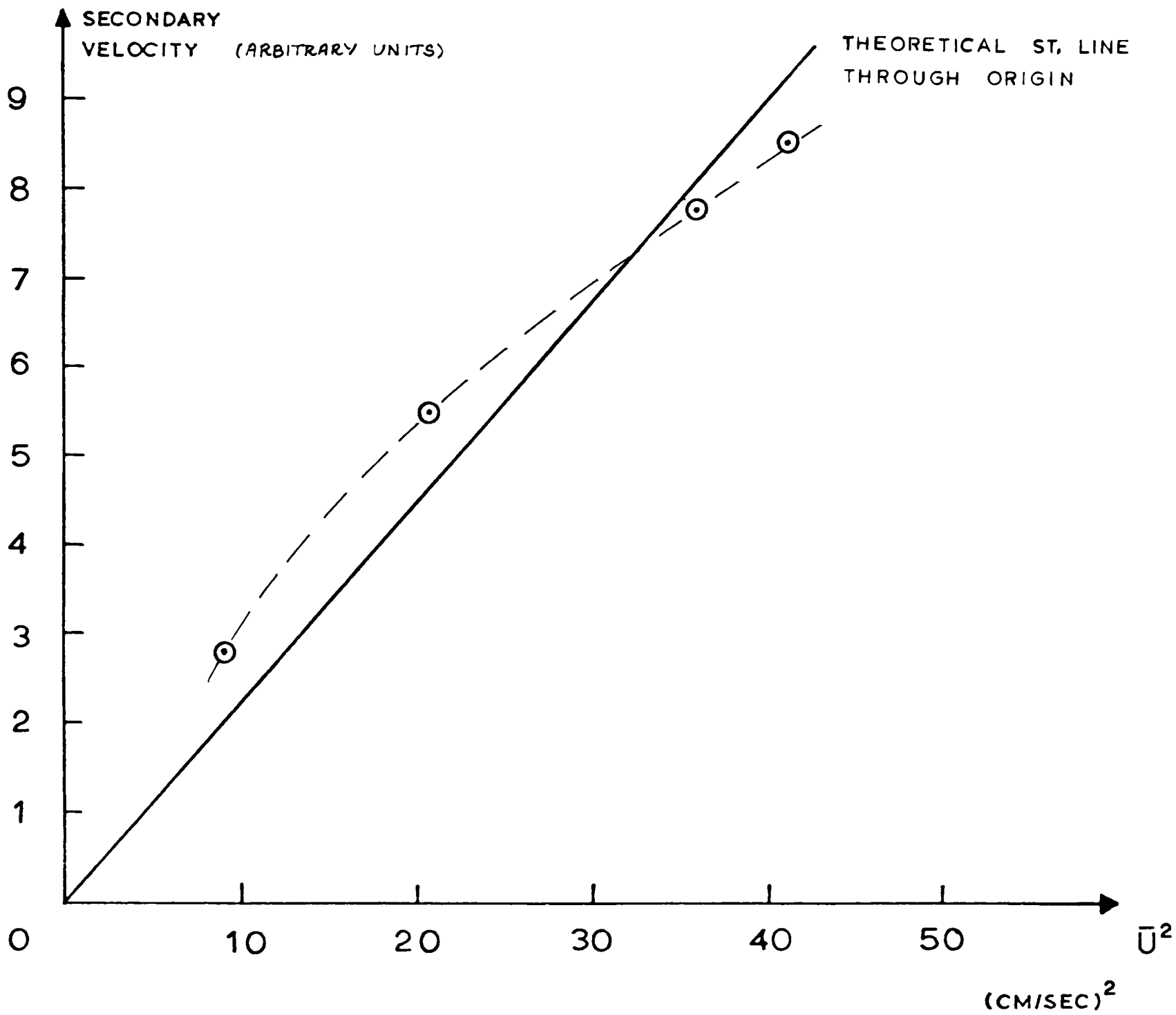
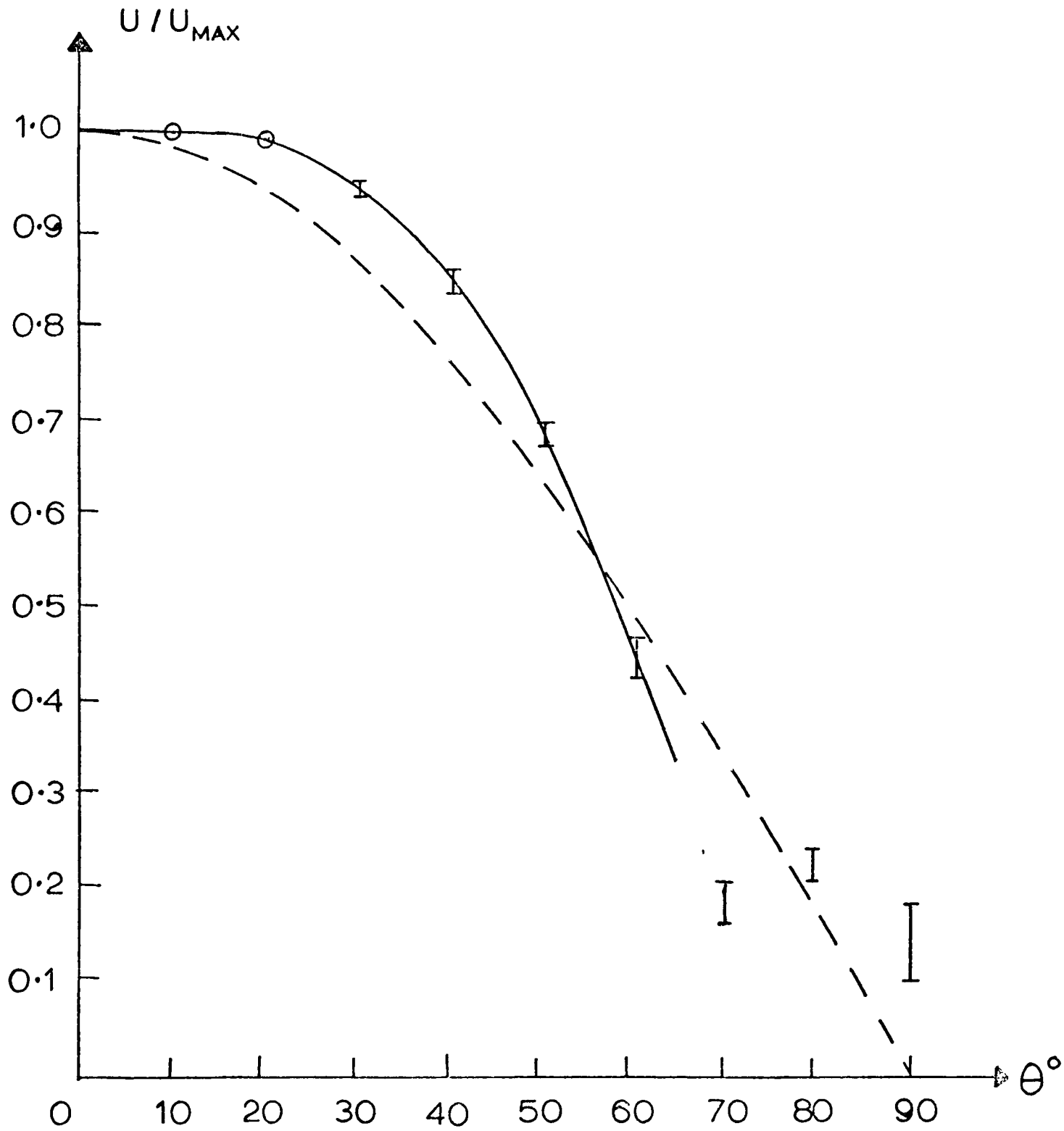


FIGURE 4.7

SECONDARY VELOCITY V. MEAN VELOCITY SQUARED



I : SCATTER OF EXPERIMENTAL POINTS

— — — — : COSINE CURVE

FIGURE 5.3

CALIBRATION OF PROBE AGAINST ANGLE

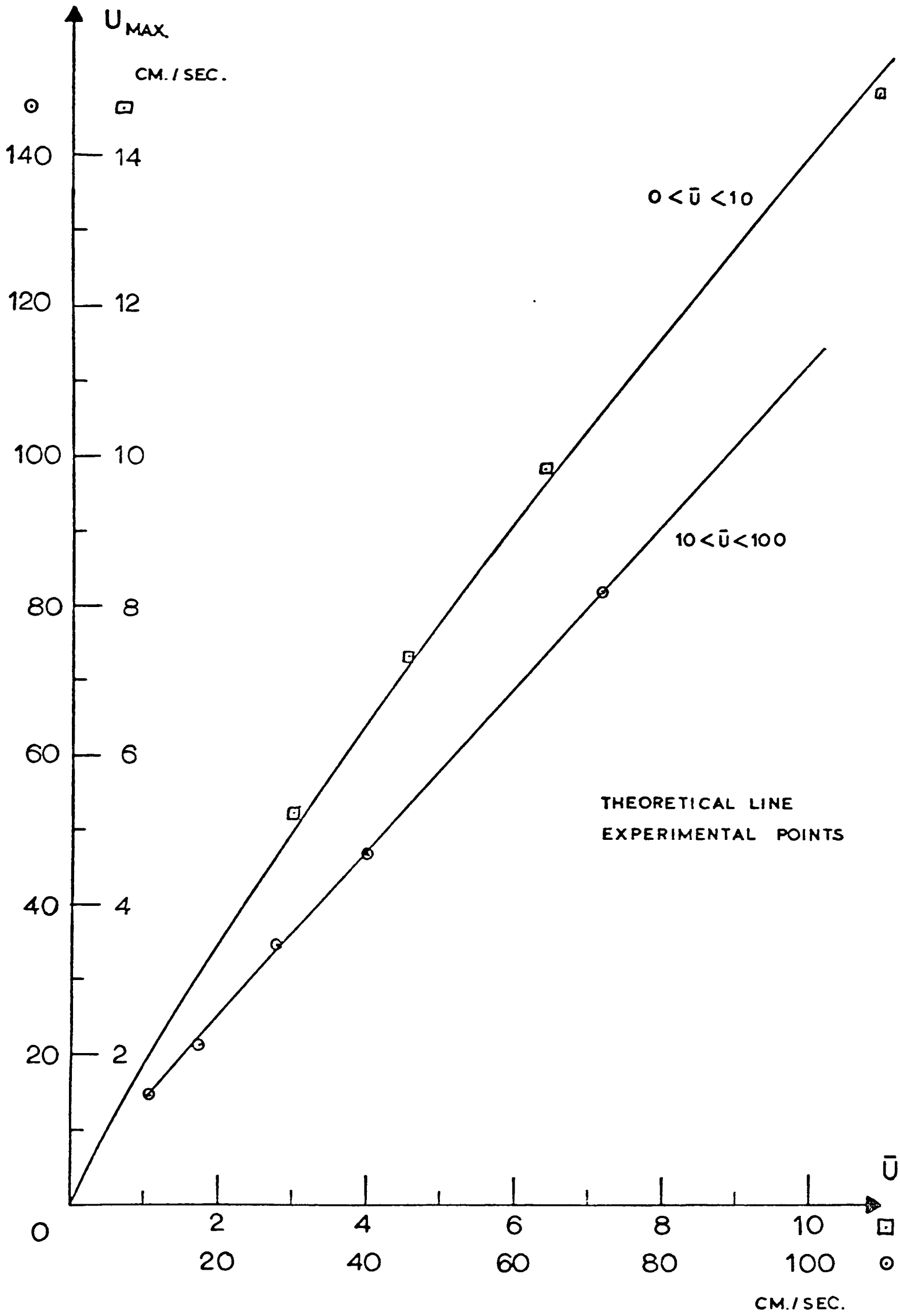


FIGURE 5·4

CALIBRATION SECTION VELOCITIES

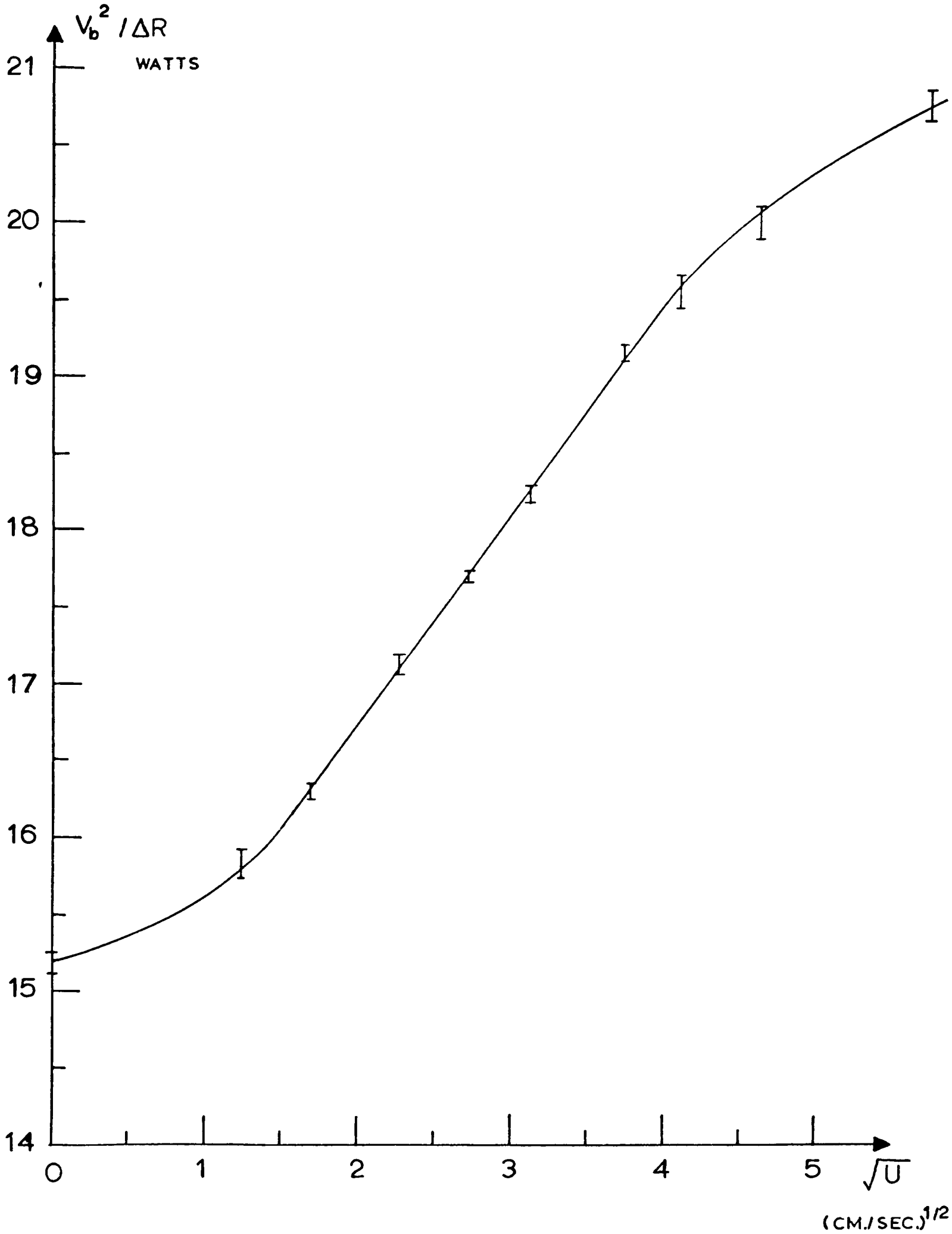


FIGURE 5.5

TYPICAL PROBE CALIBRATION CURVE

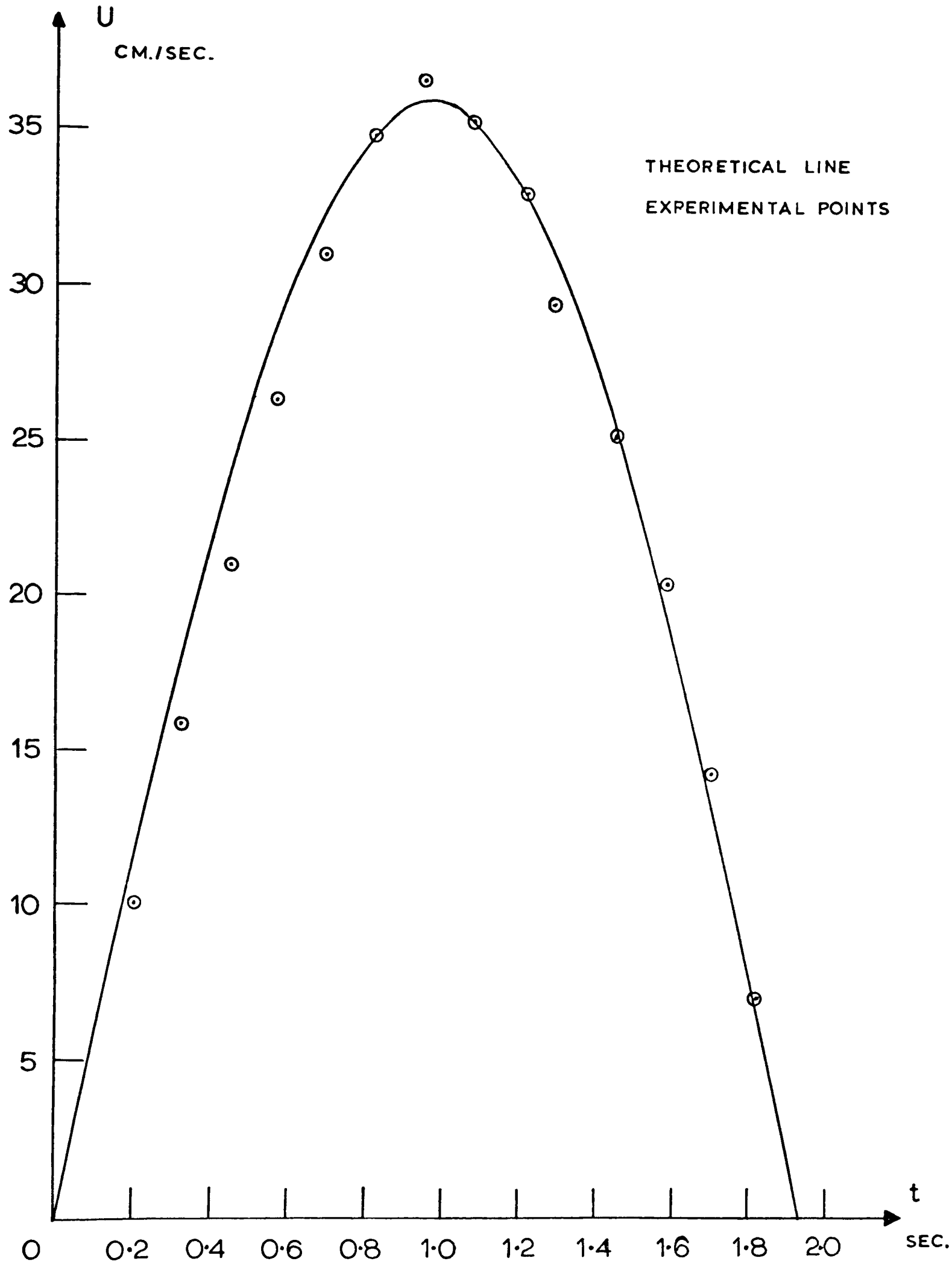


FIGURE 5·6

DYNAMIC CALIBRATION OF PROBE

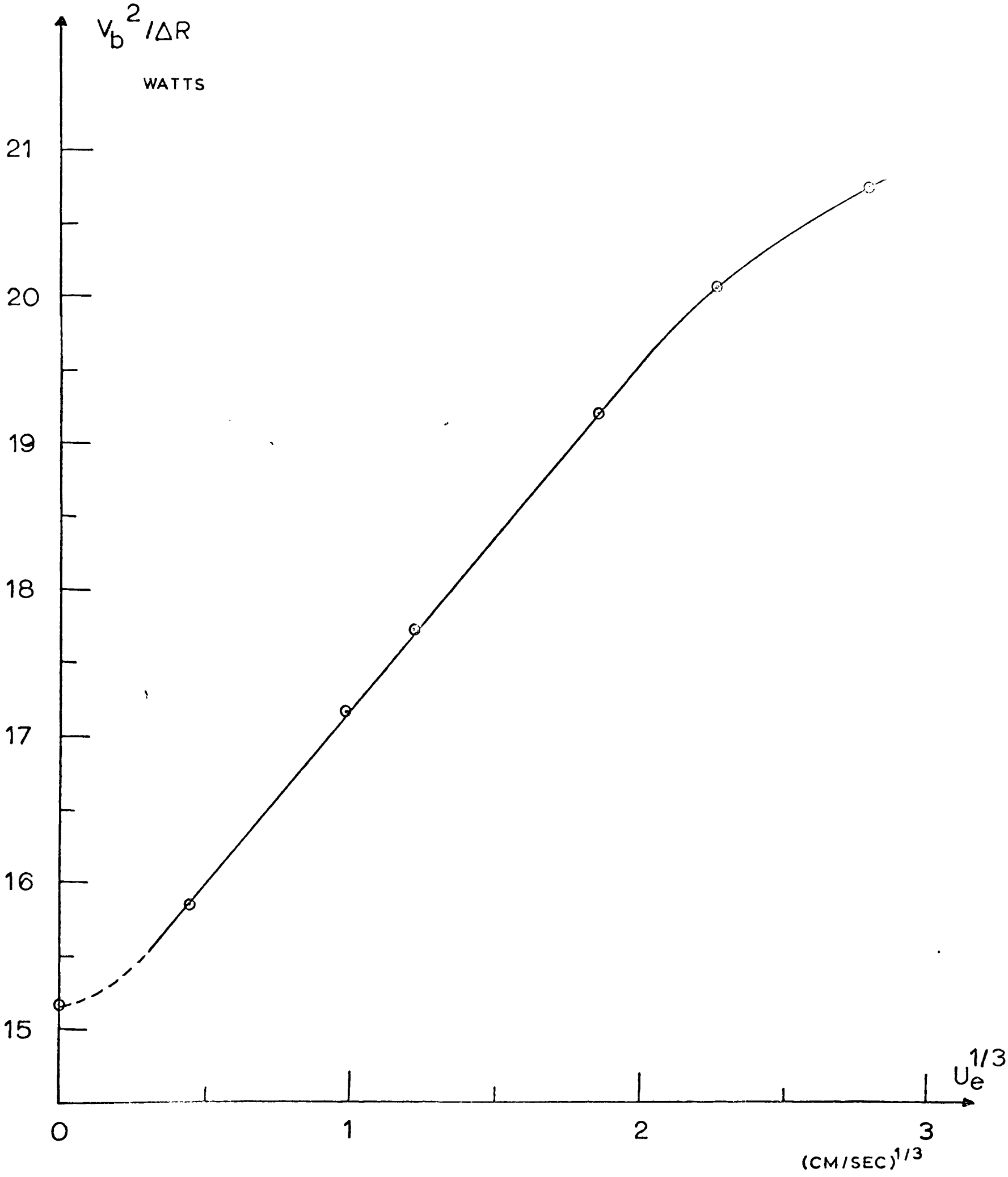
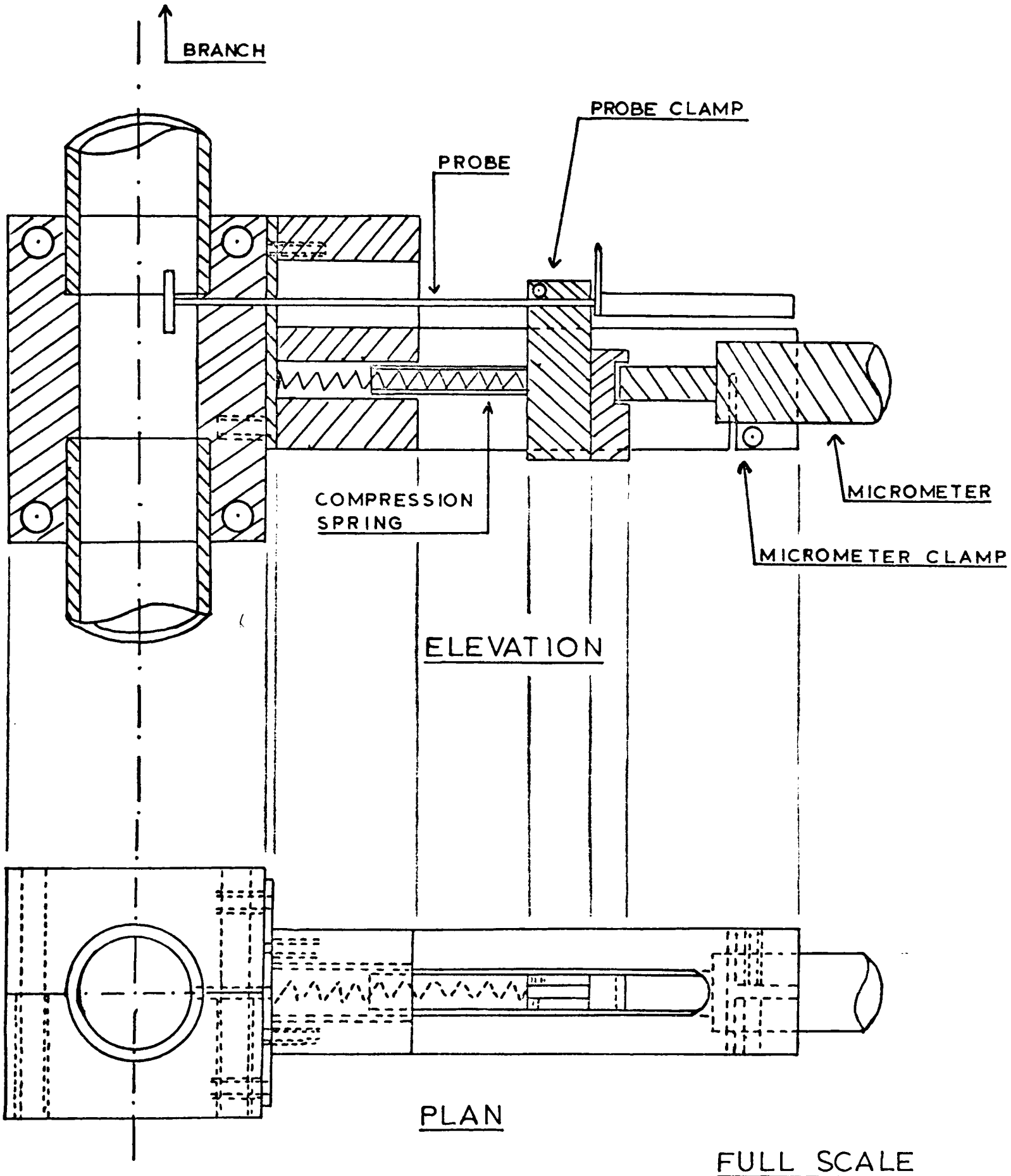


FIGURE 5.8

CALIBRATION OF PROBE AGAINST PROBE TUBE VELOCITY

PROBE TRAVERSE MECHANISM

1.



2.

FULL SCALE

1. SECTION THROUGH CENTRE. PROBE SHOWN UNSECTIONED
2. MECHANISM WITHOUT PROBE IN POSITION.

FIGURE 6.1. PROBE TRAVERSE MECHANISM

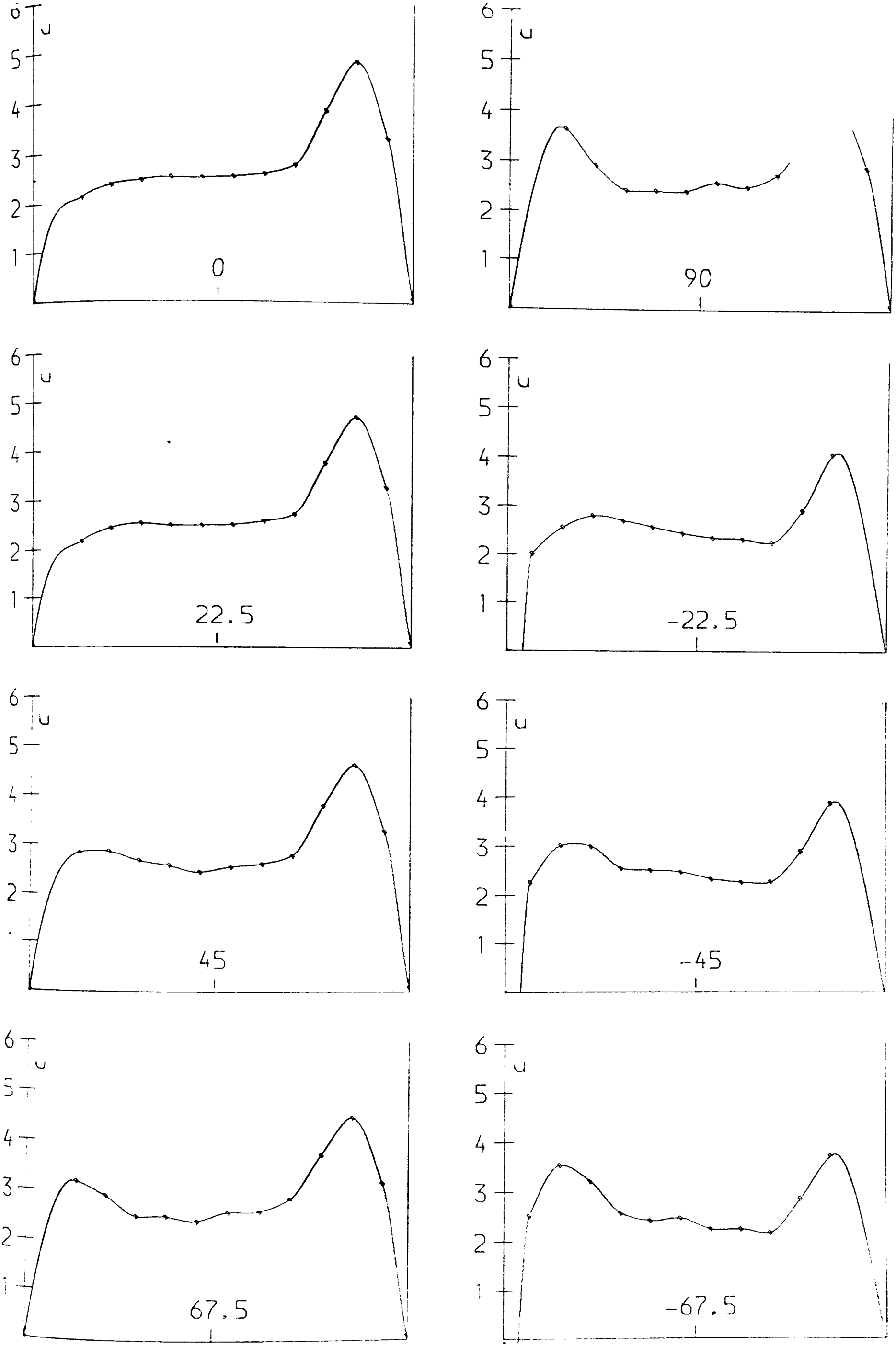
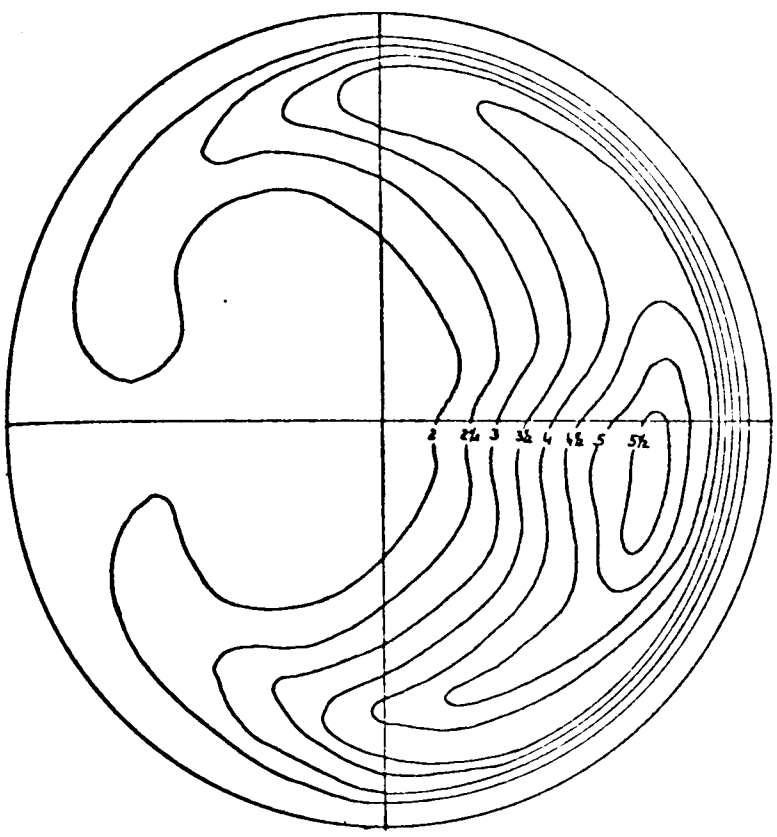


FIGURE 6.2

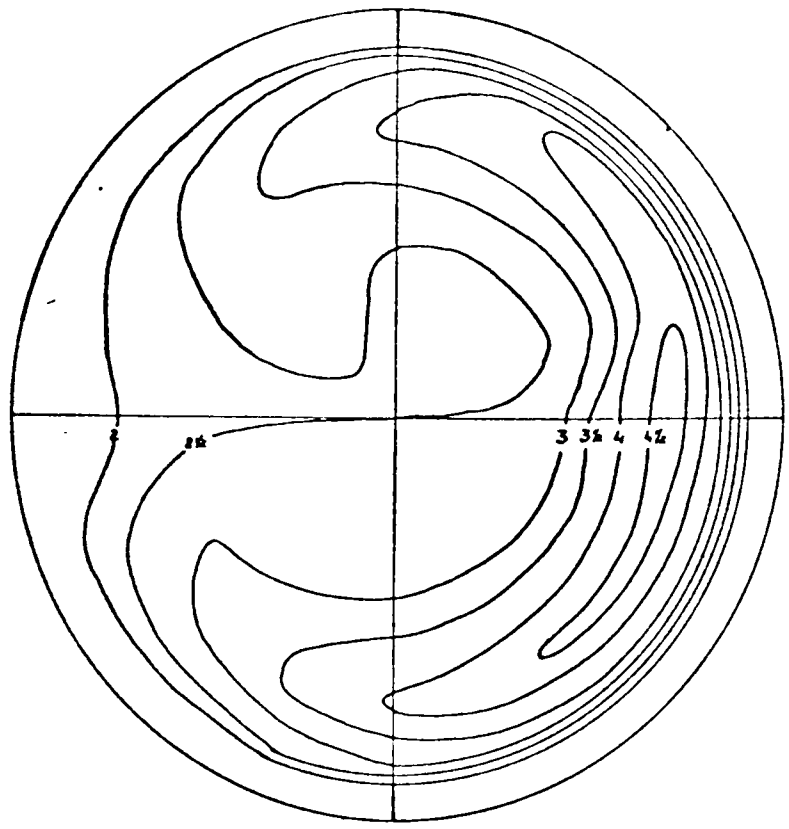
TYPICAL PLOT OF VELOCITY AGAINST POSITION IN EACH TRAVERSE

VELOCITY PLOTS

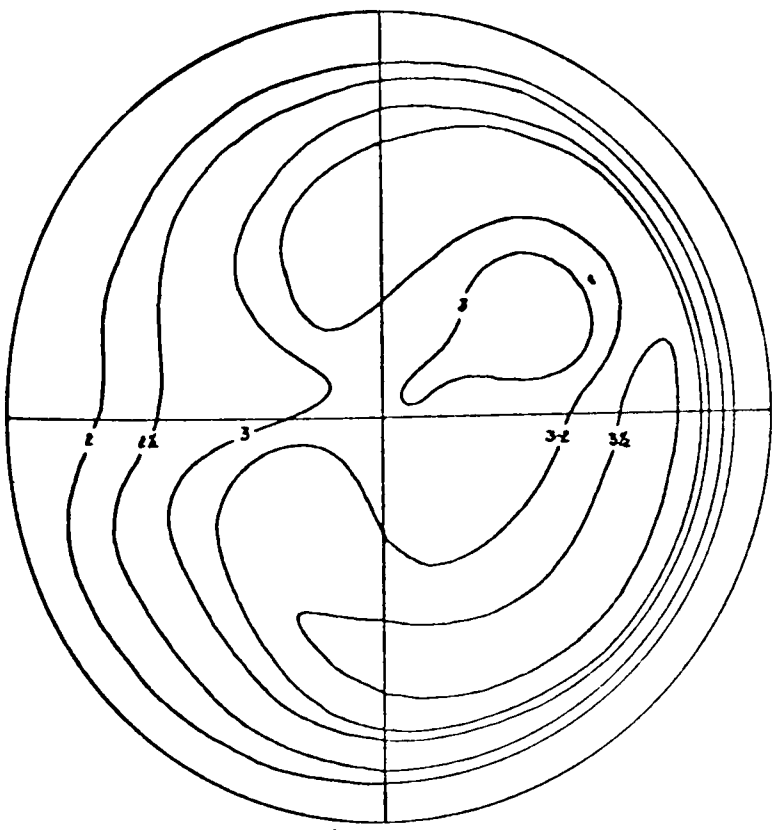
BRANCH 1 LOW FLOW



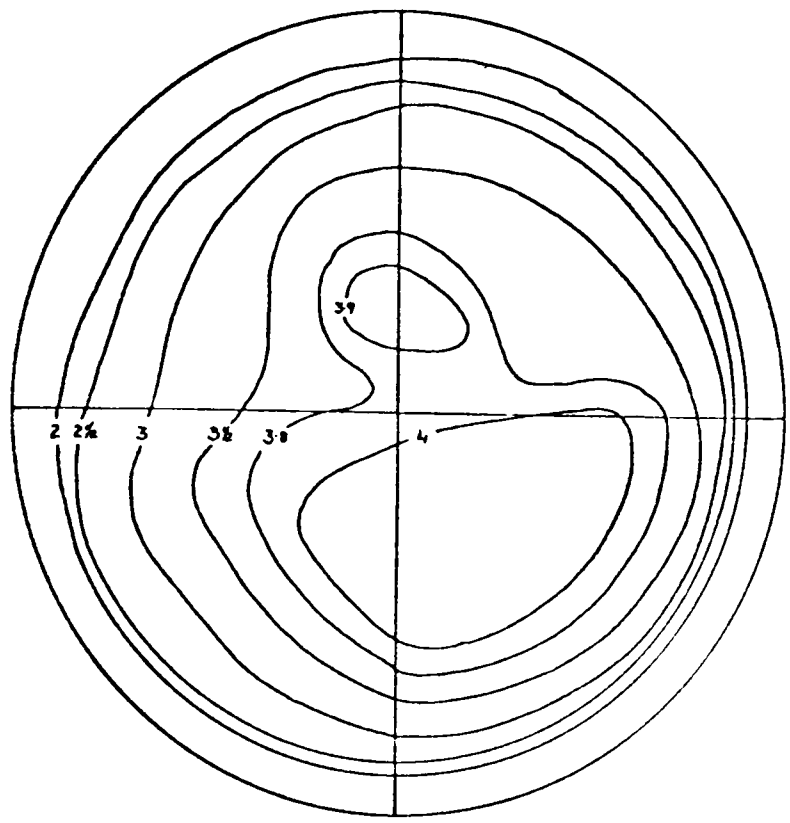
1 L 3



1 L 7



1 L 11

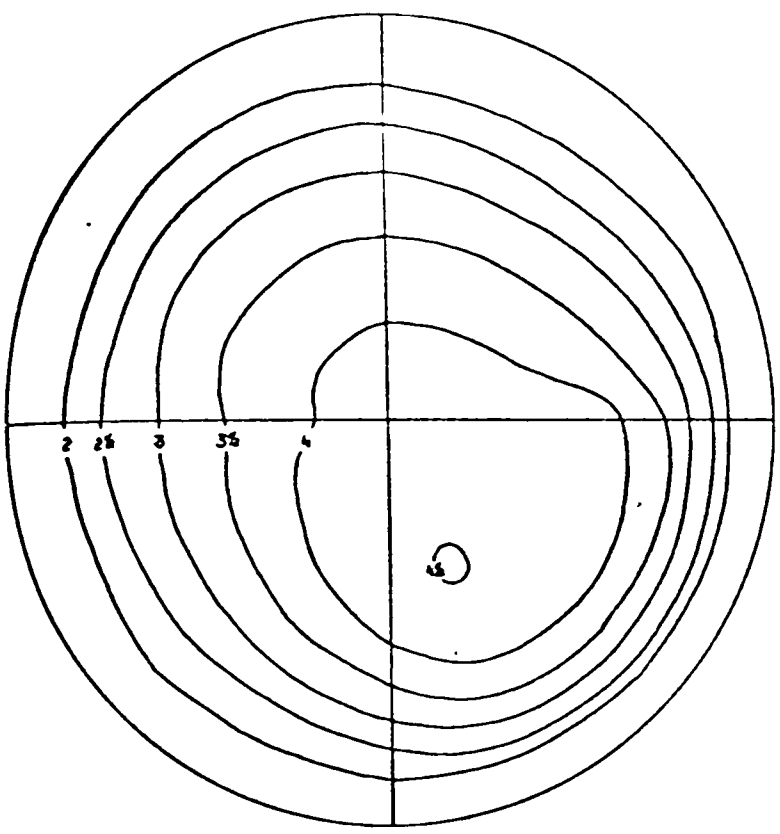


1 L 15

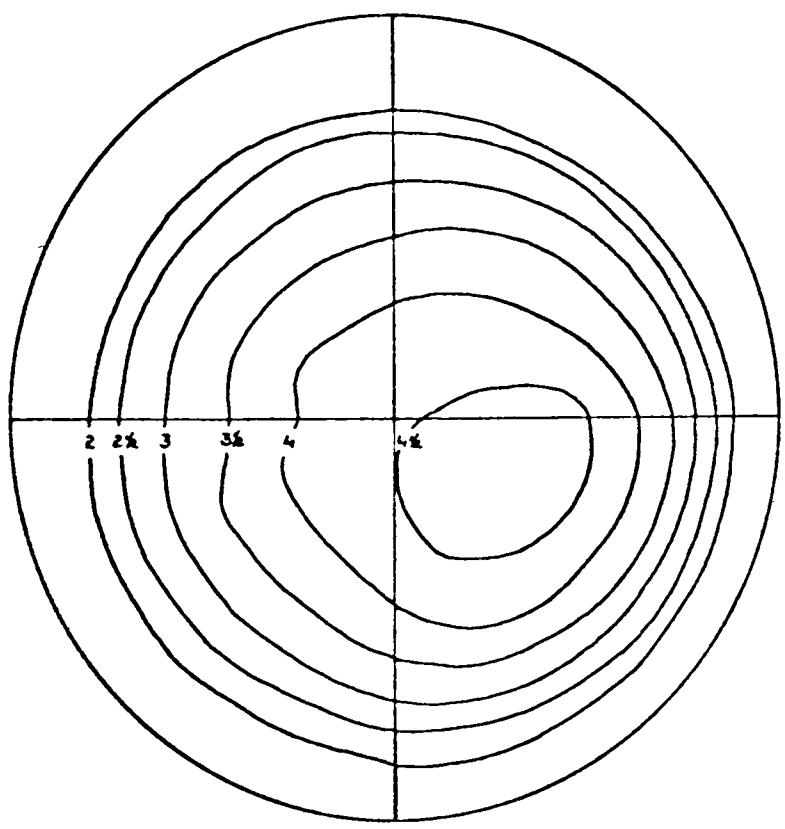
FIGURE 6.3

VELOCITY PLOTS

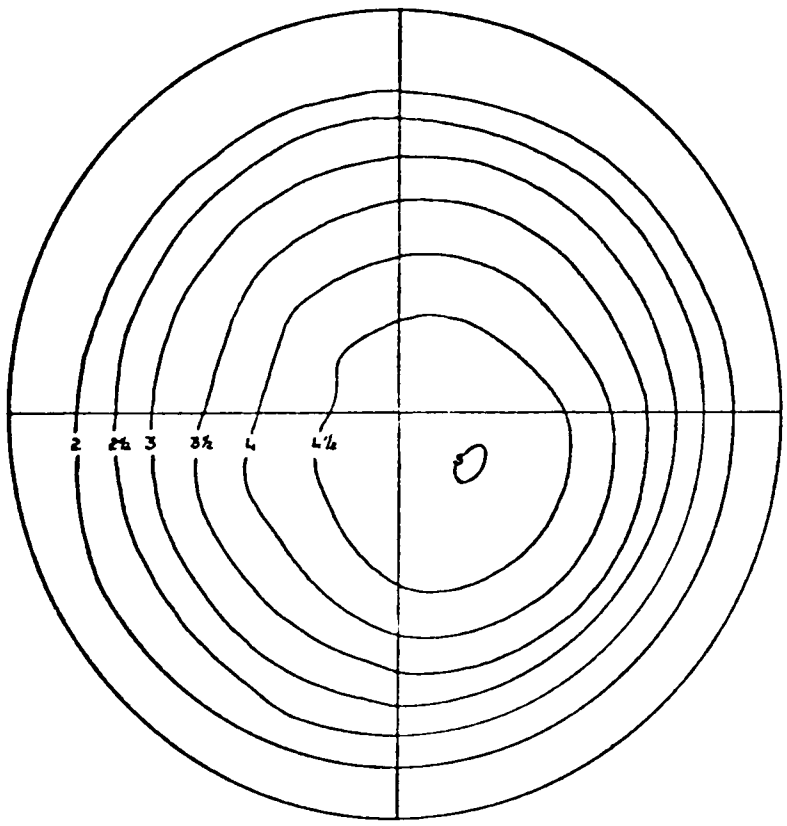
BRANCH 1 LOW FLOW



1 L 23



1 L 31

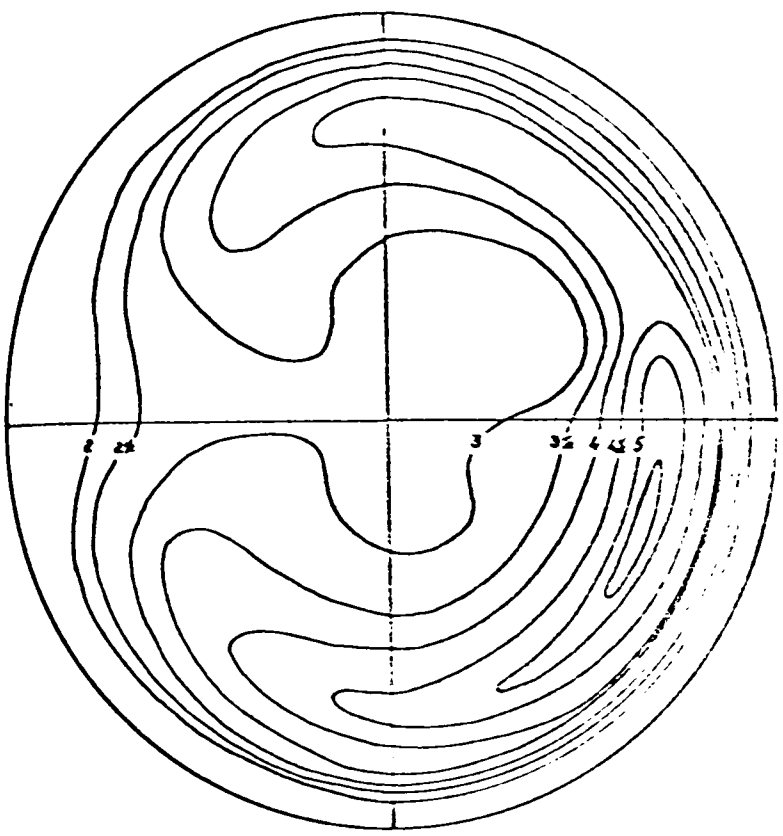


1 L 47

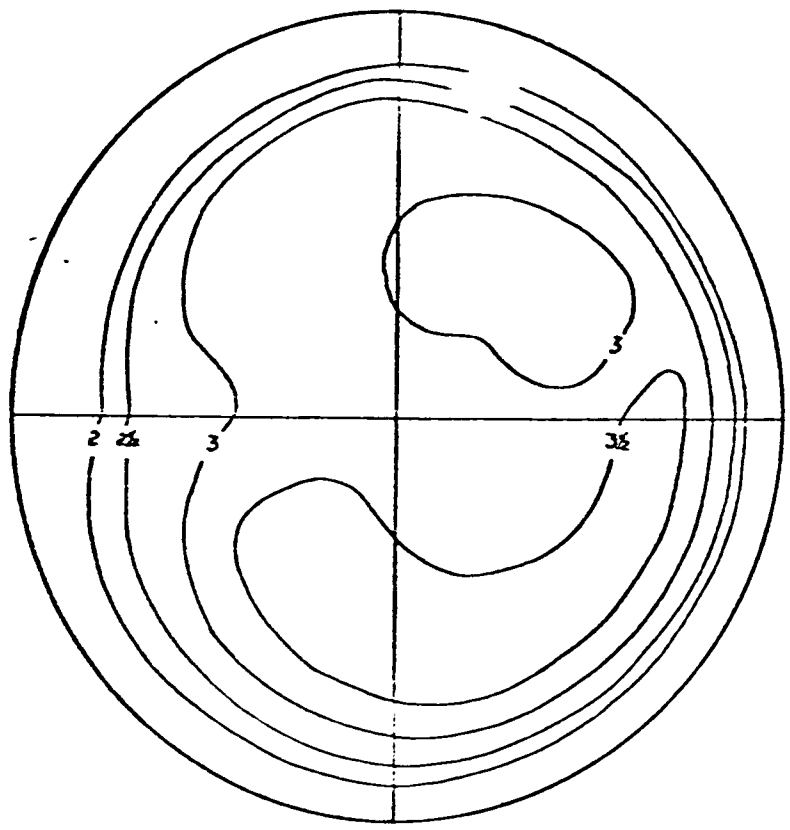
FIGURE 6.4

VELOCITY PLOTS

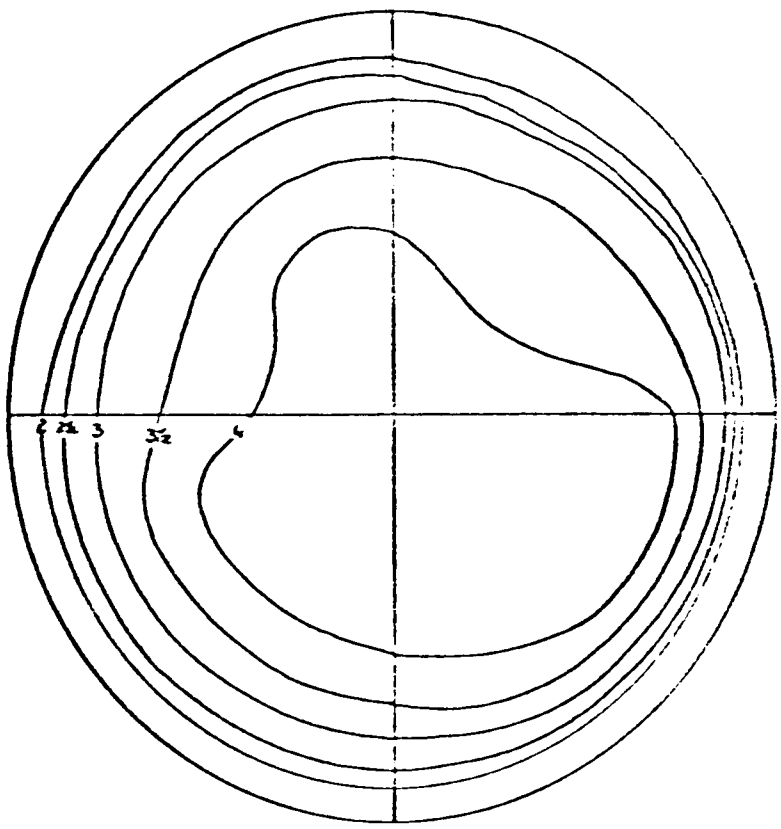
BRANCH 2 LOW FLOW



2 L 7



2 L 11

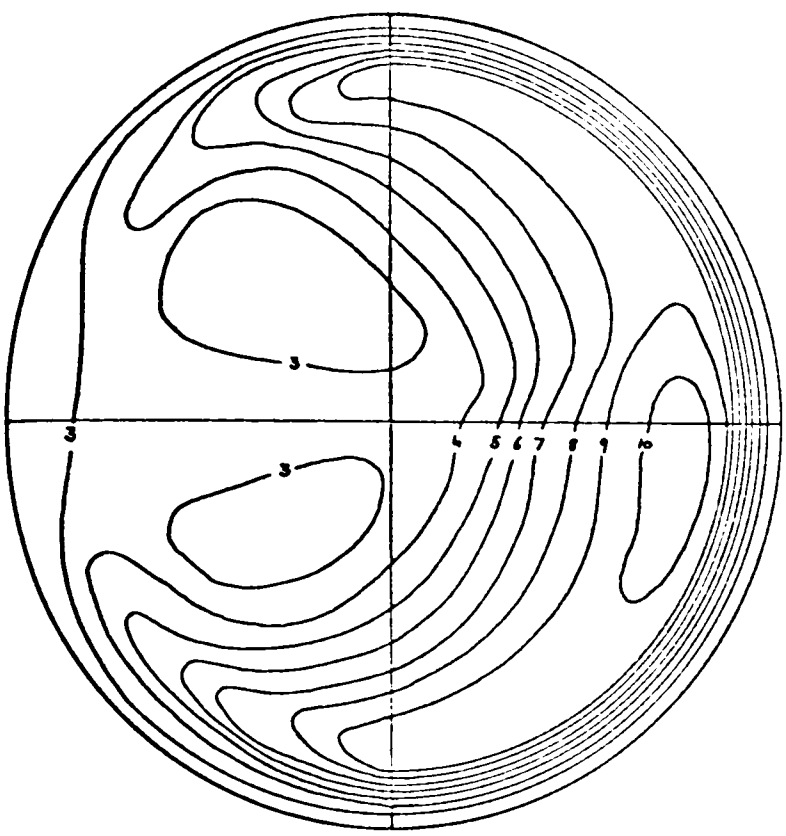


2 L 15

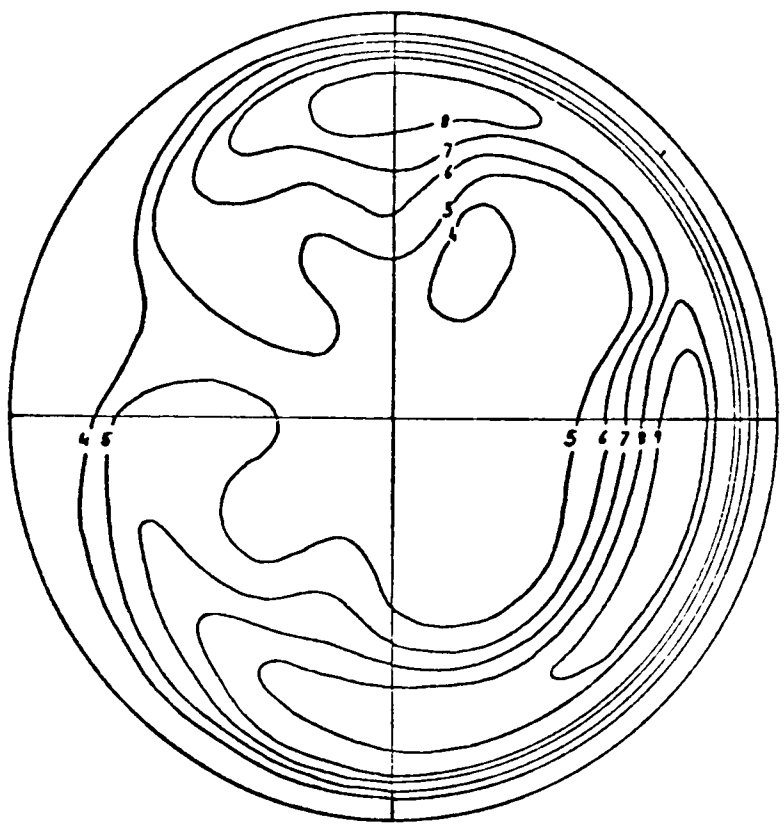
FIGURE 6.5

VELOCITY PLOTS

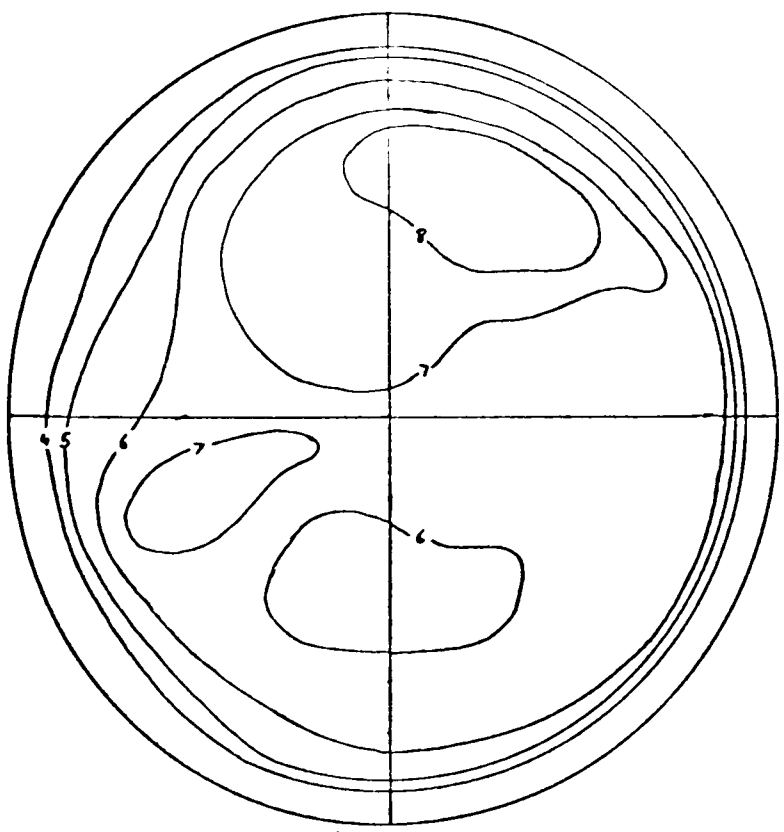
BRANCH 1 HIGH FLOW



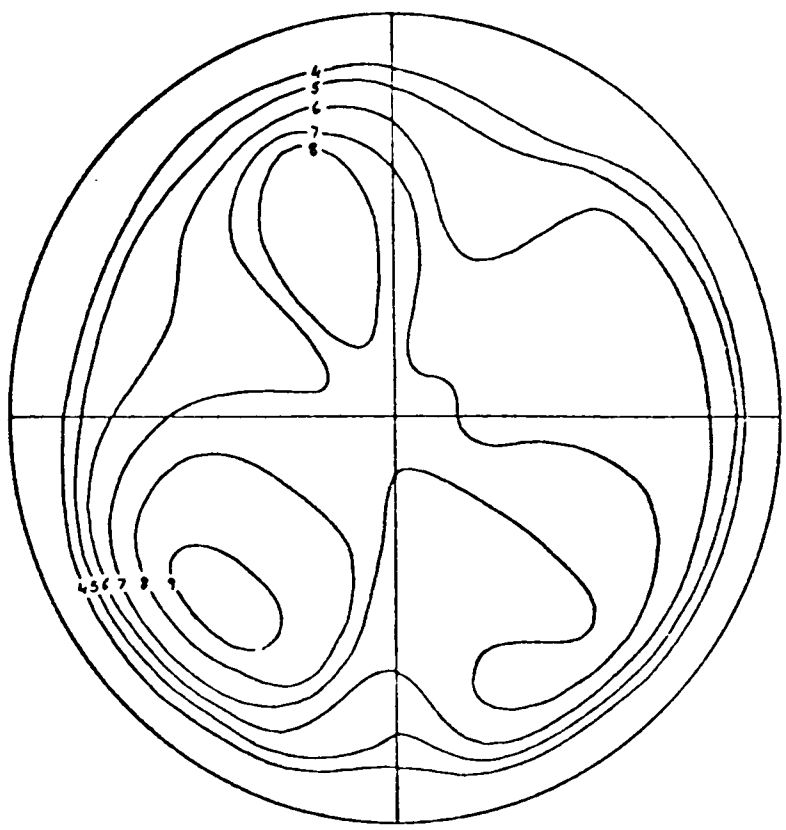
1 H 3



1 H 7



1 H 11

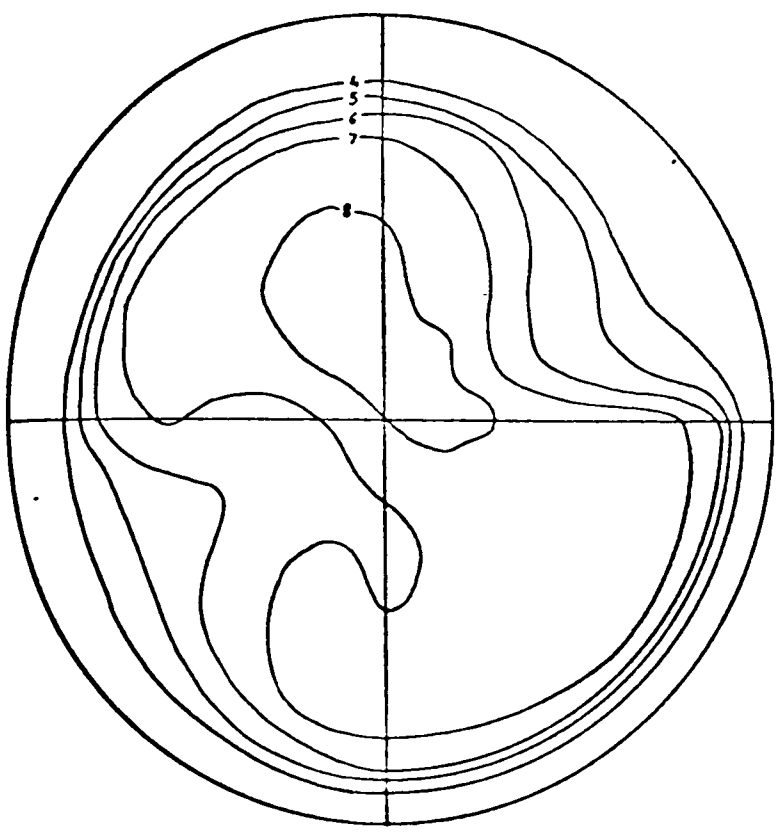


1 H 15

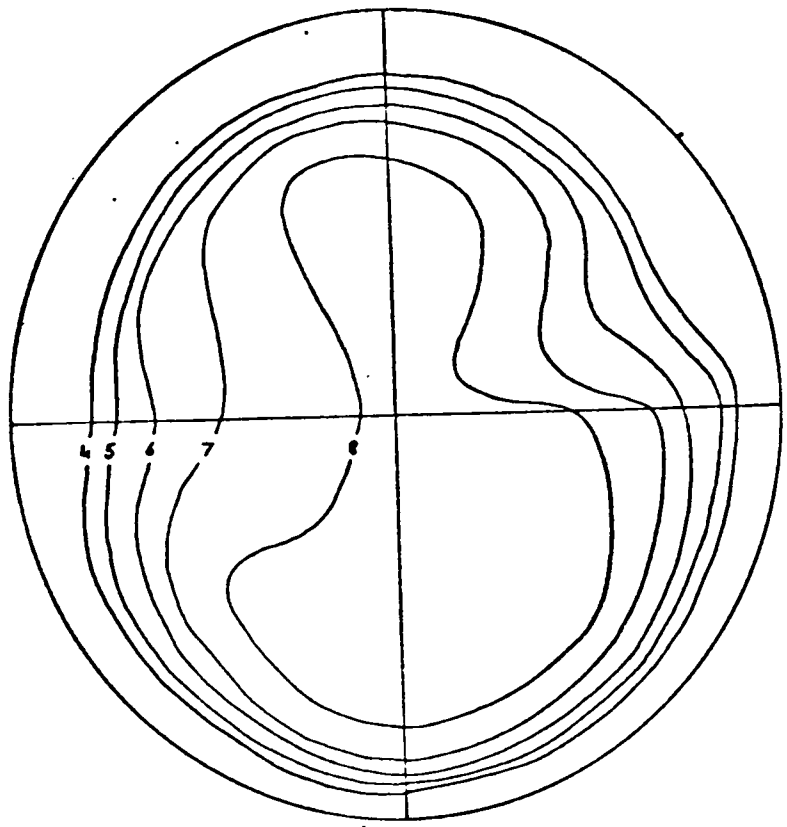
FIGURE 6.6

VELOCITY PLOTS

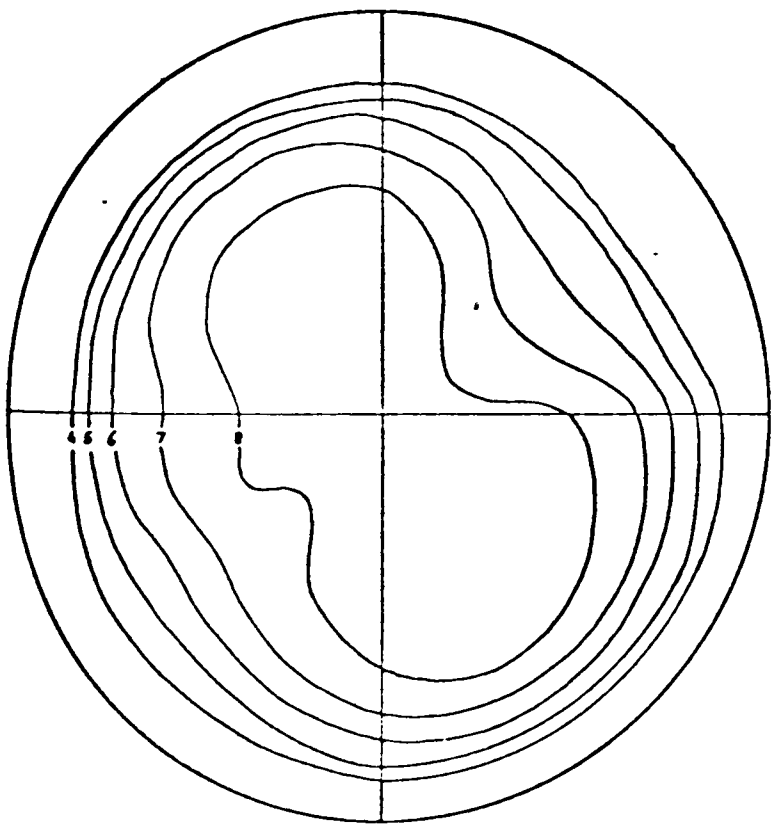
BRANCH 1 HIGH FLOW



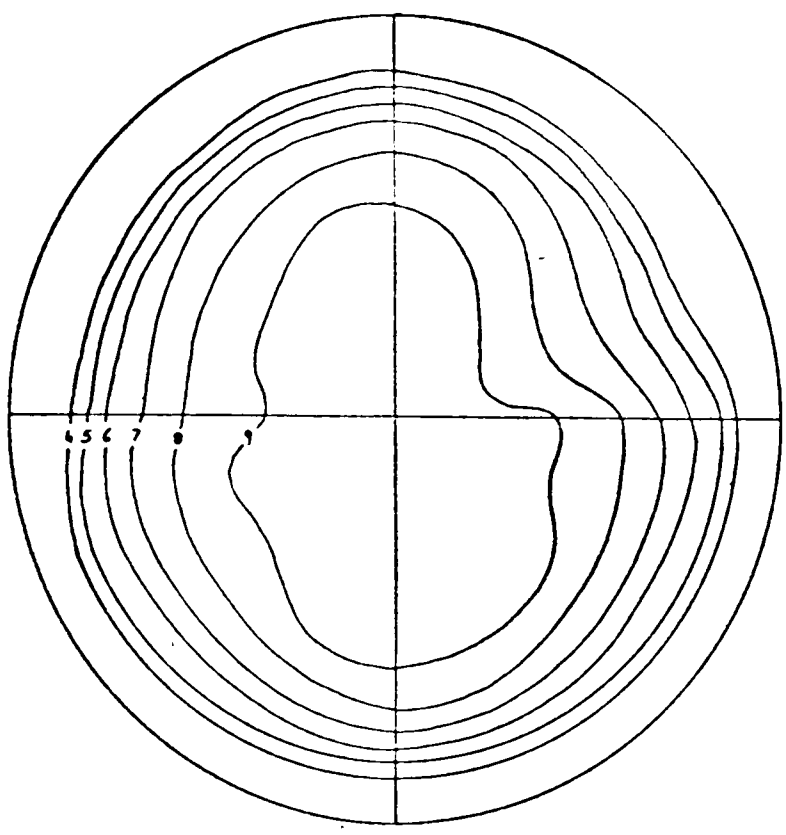
1 H 23



1 H 31



1 H 47

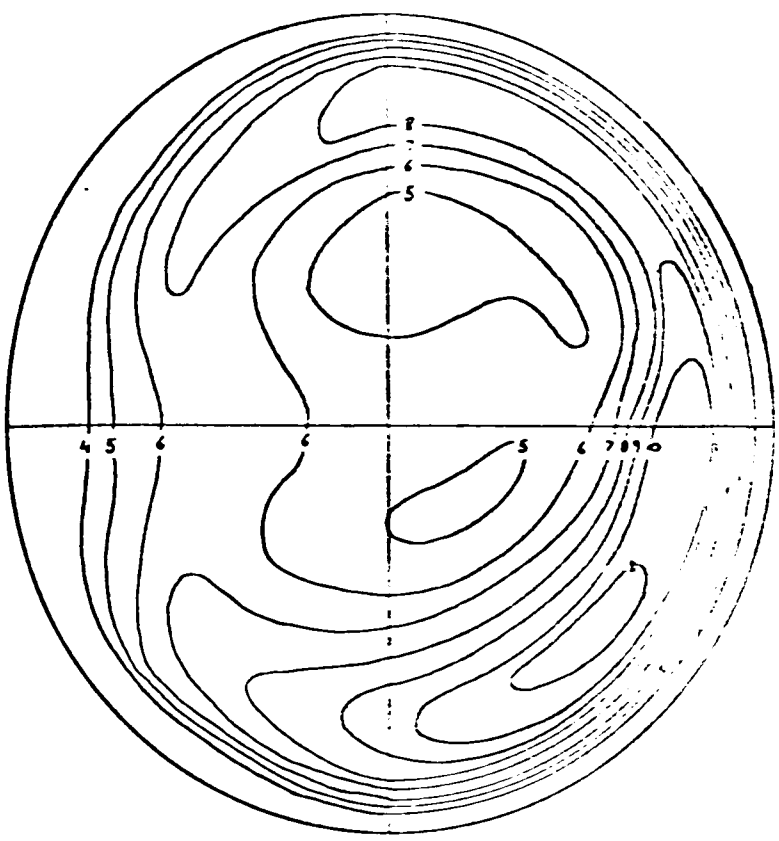


1 H 63

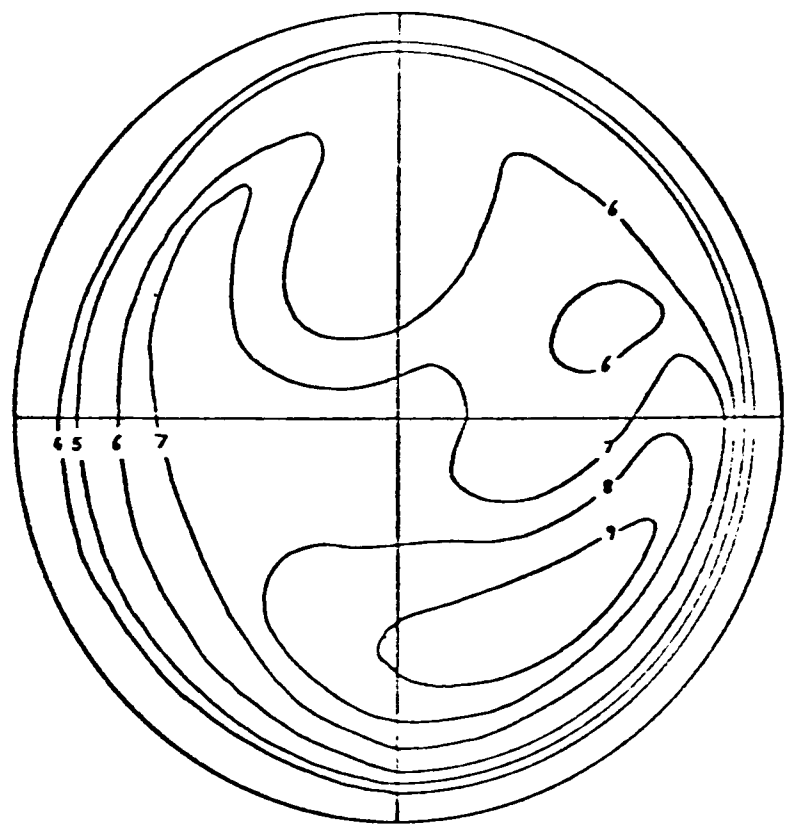
FIGURE 6.7

VELOCITY PLOTS

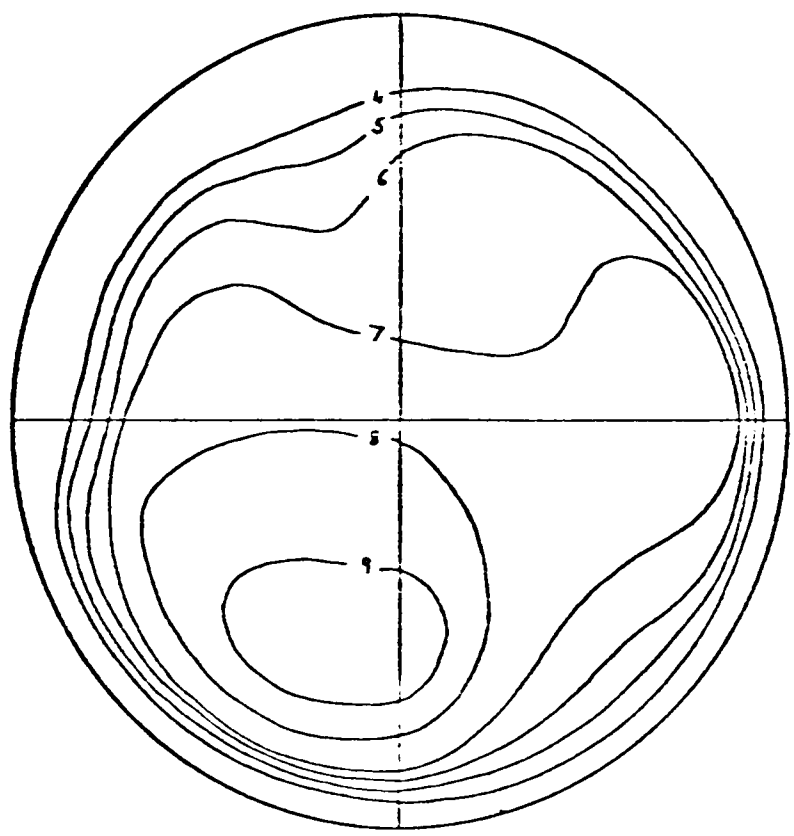
BRANCH 2 HIGH FLOW



2 H 7



2 H 11

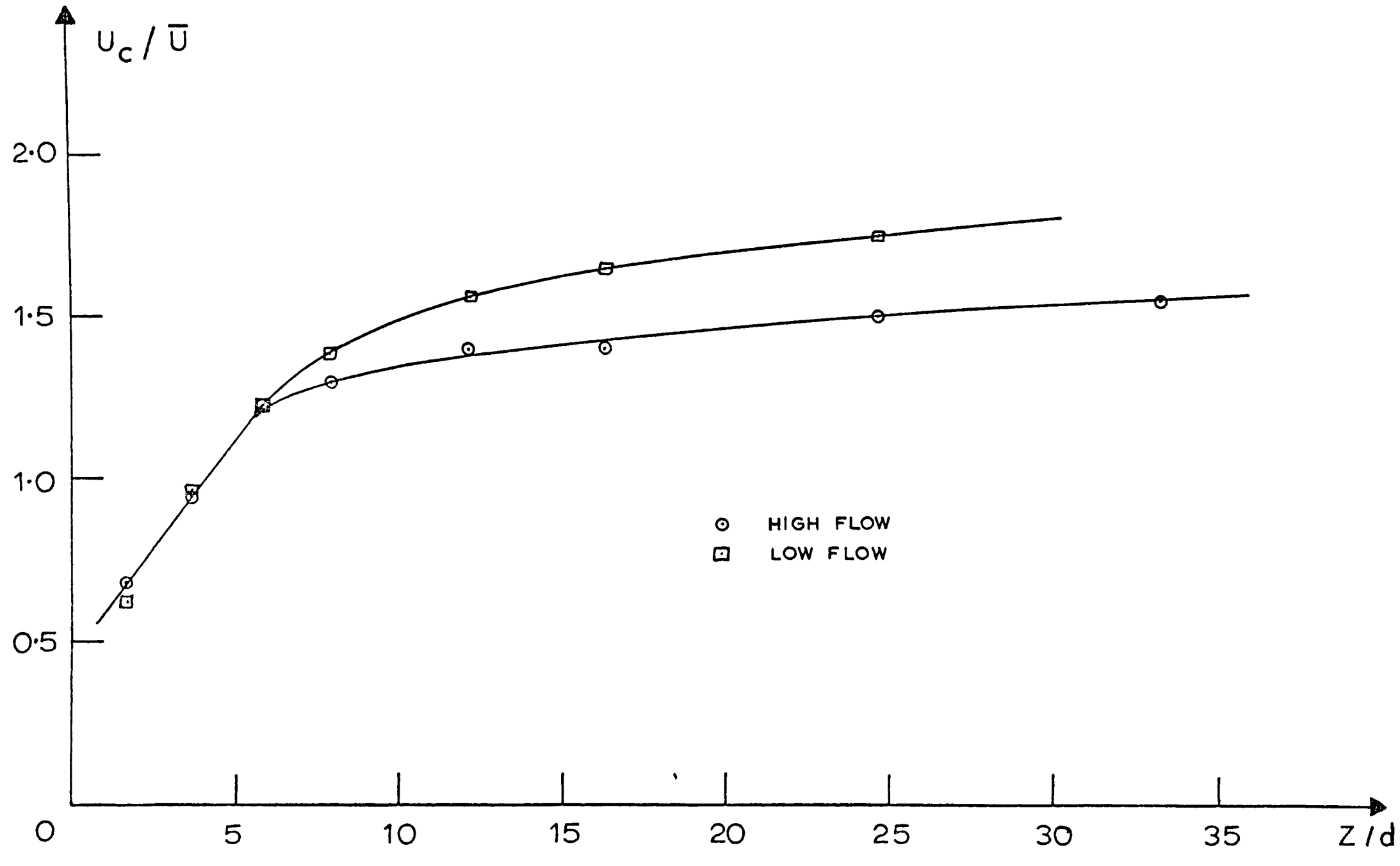


2 H 15

FIGURE 6.8

FIGURE 6.9

CENTRELINE VELOCITY V. DISTANCE DOWNSTREAM



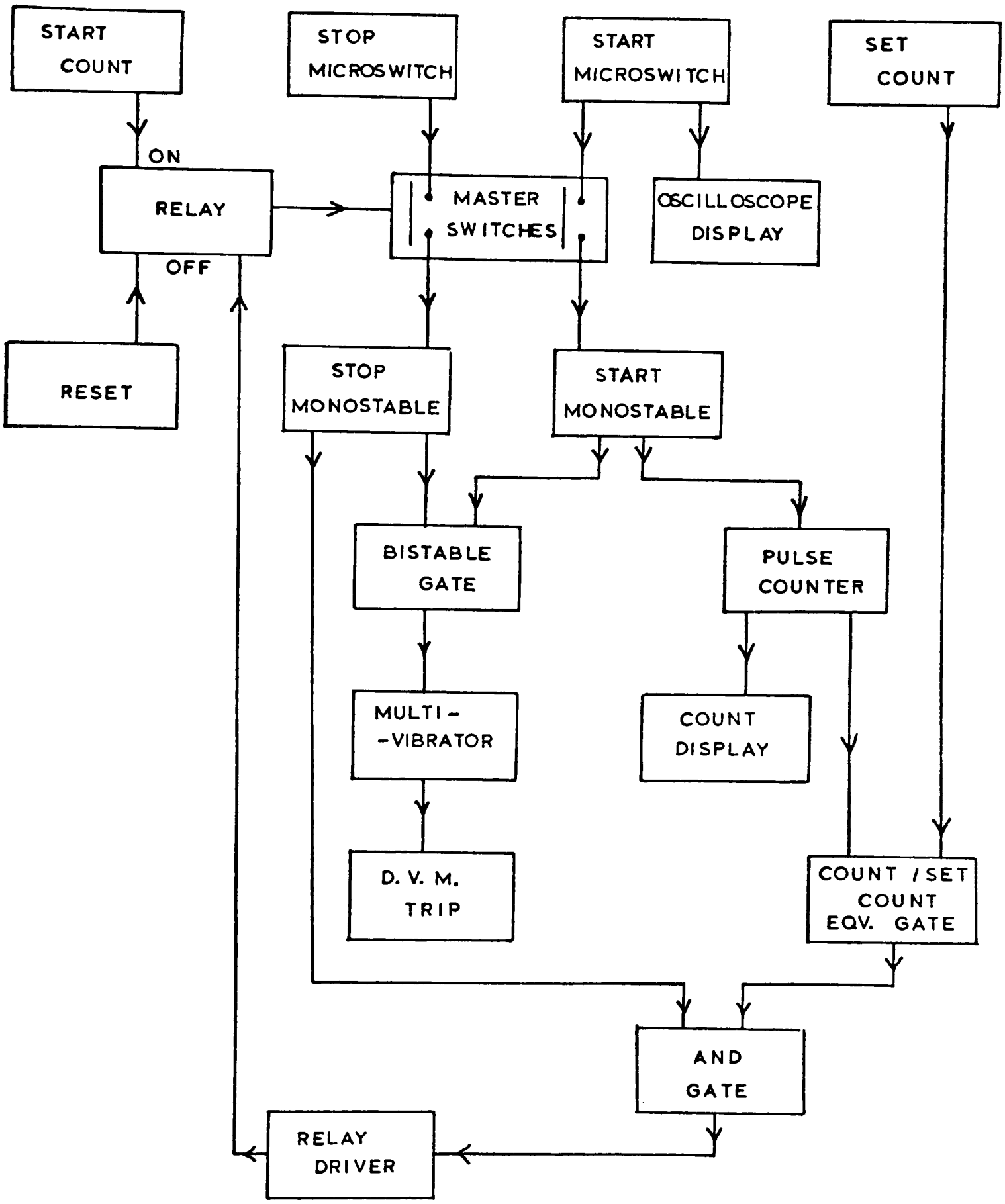


FIGURE 7.1

BLOCK DIAGRAM OF PULSE SAMPLER

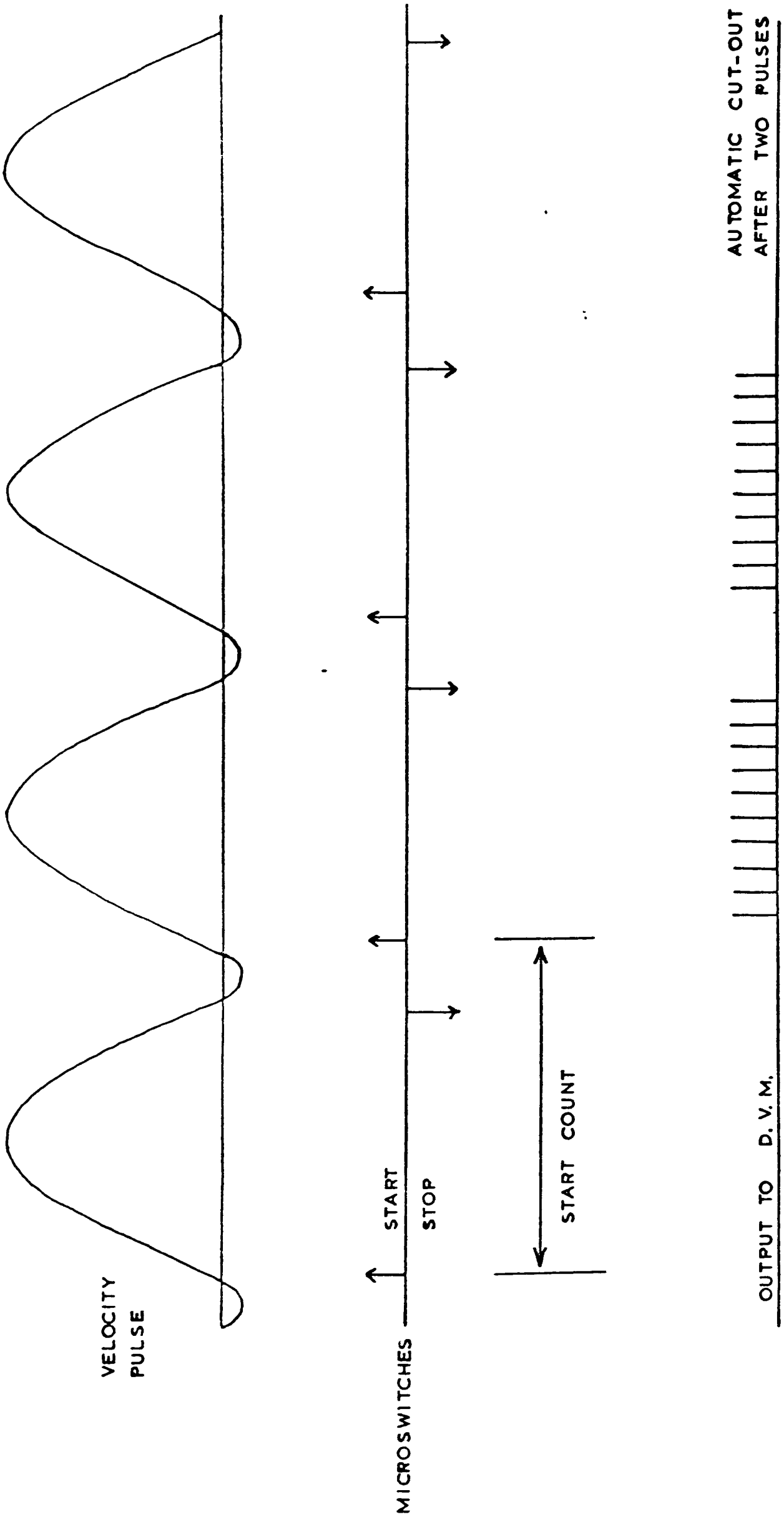


FIGURE 7.2

SAMPLING TWO PULSES AT TEN SAMPLES PER SECOND

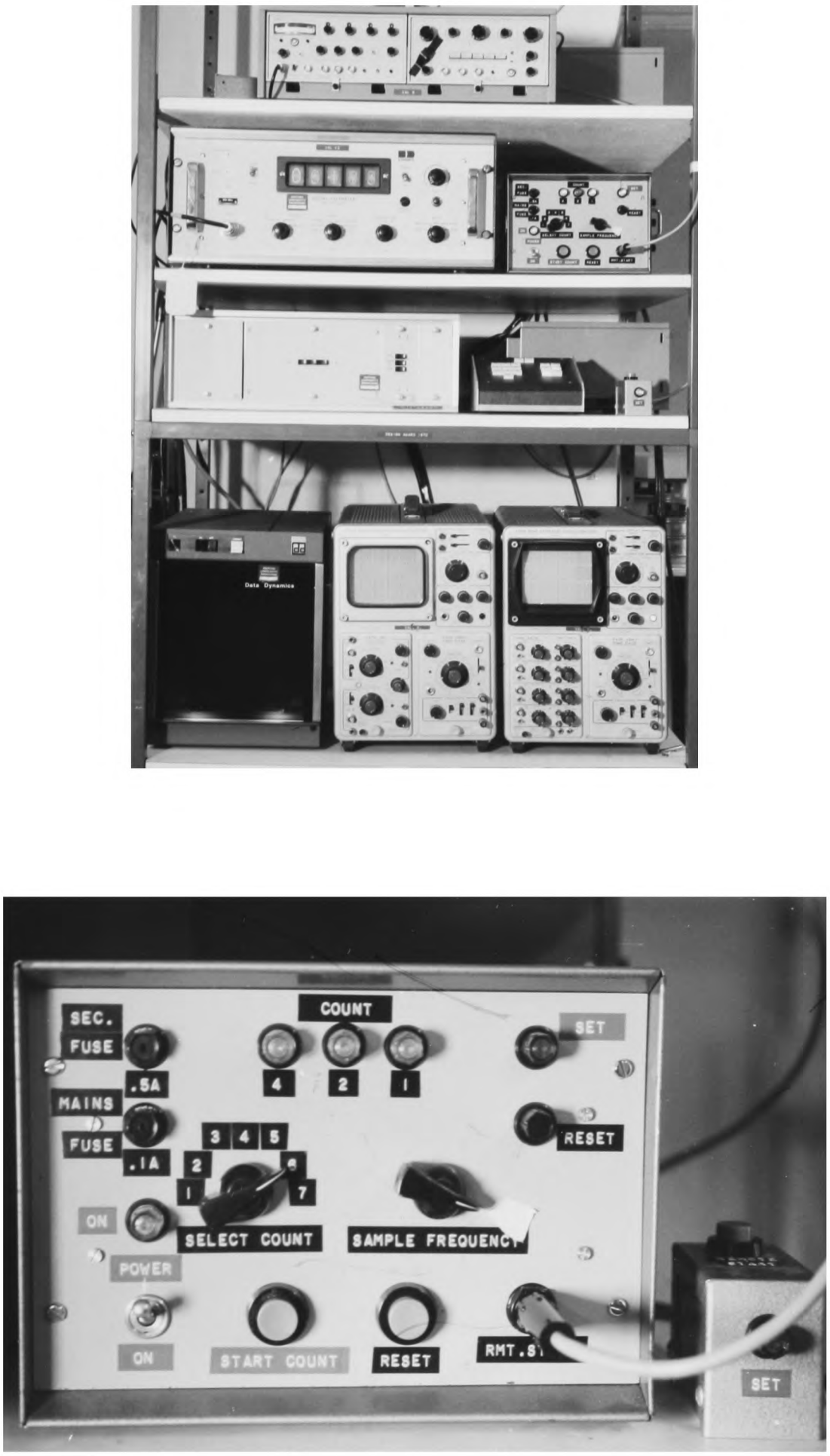


Figure 7.3. The data logging system.

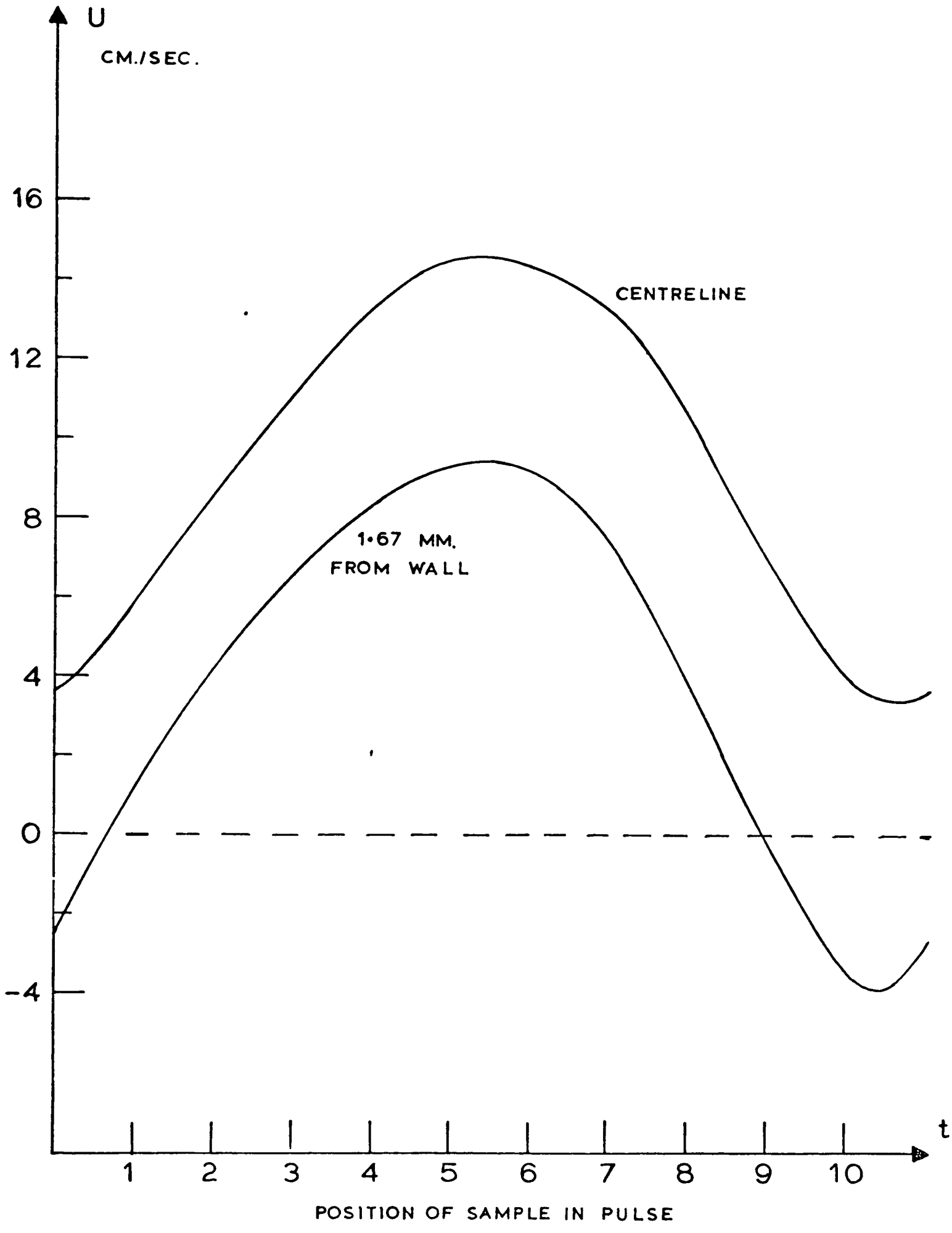


FIGURE 8.1

PULSATILE FLOW INPUT

PULSATILE FLOW VELOCITY PLOTS 3 CM. DOWNSTREAM OF BRANCH 1
LOW FLOW

1L3P

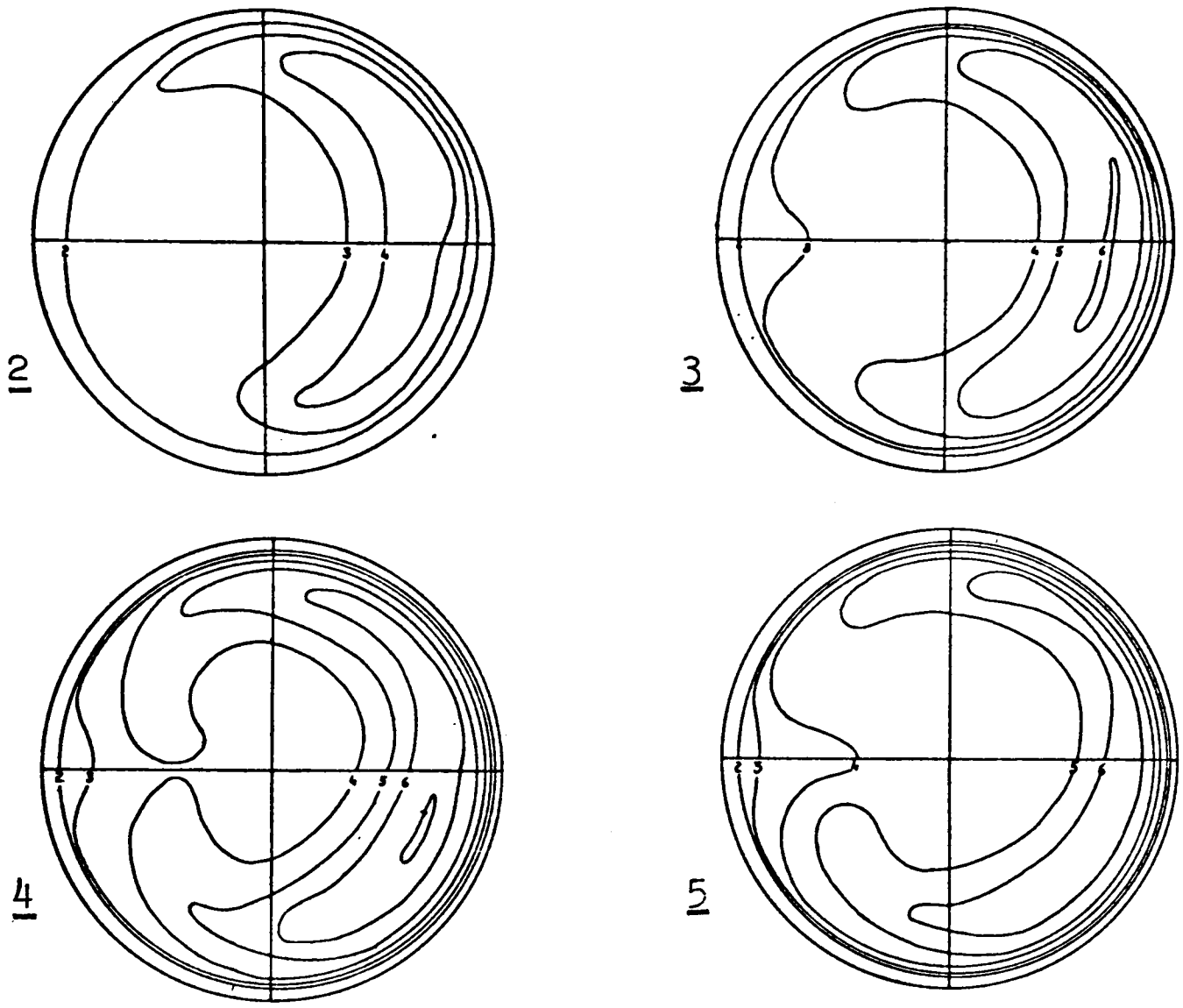


FIGURE 8.2

PULSATILE FLOW VELOCITY PLOTS 7 CM. DOWNSTREAM OF BRANCH 1
LOW FLOW

1L7P

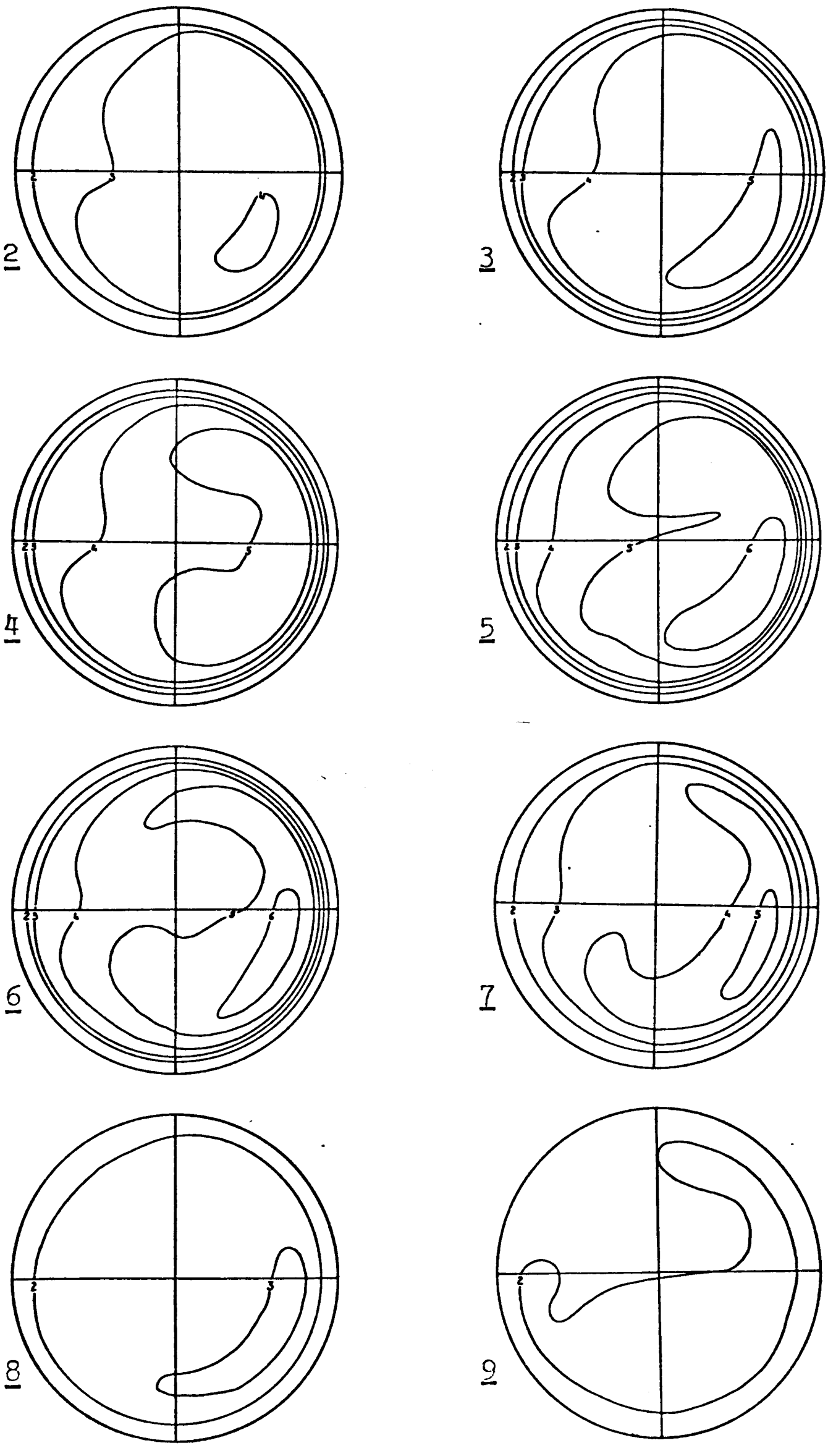
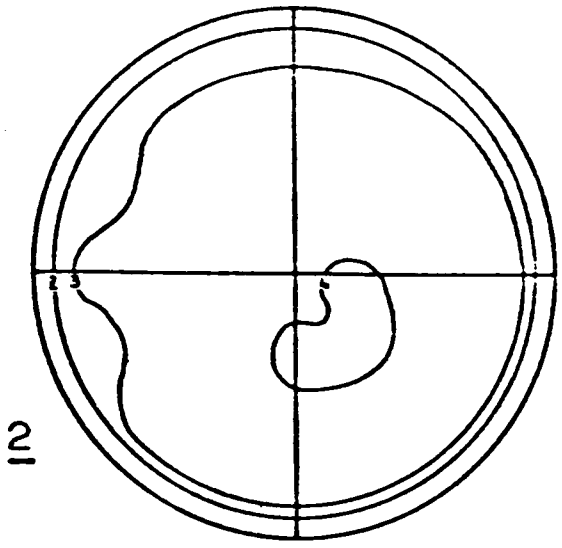


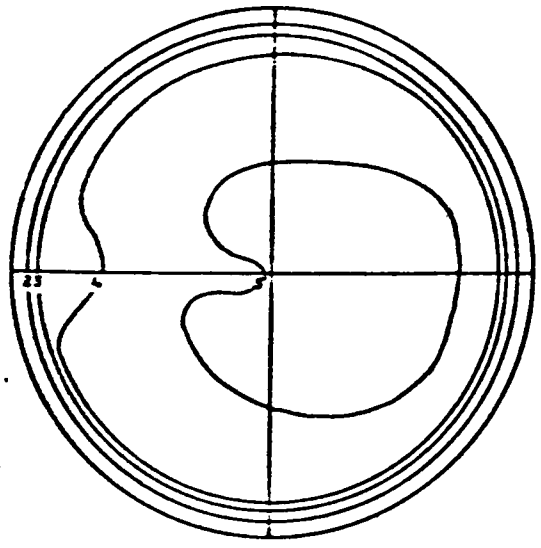
FIGURE 8.3

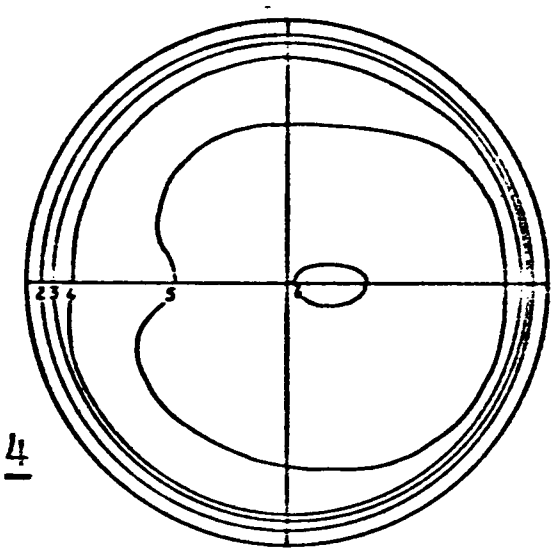
PULSATILE FLOW VELOCITY PLOTS 11 CM. DOWNSTREAM OF BRANCH 1

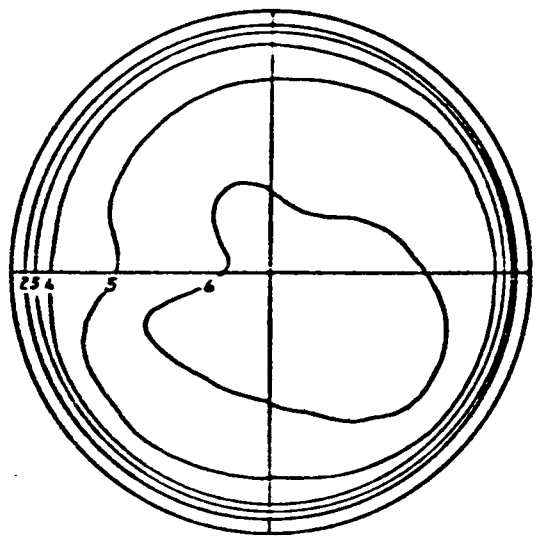
LOW FLOW

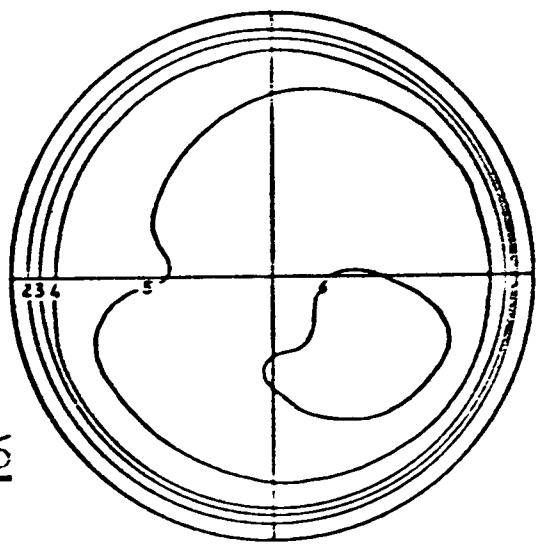
1L11P

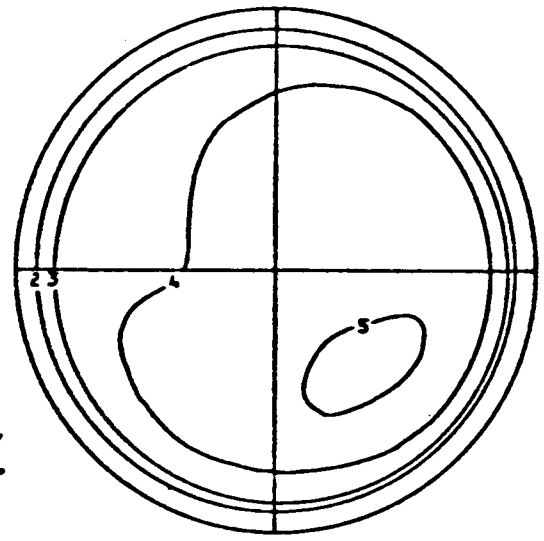


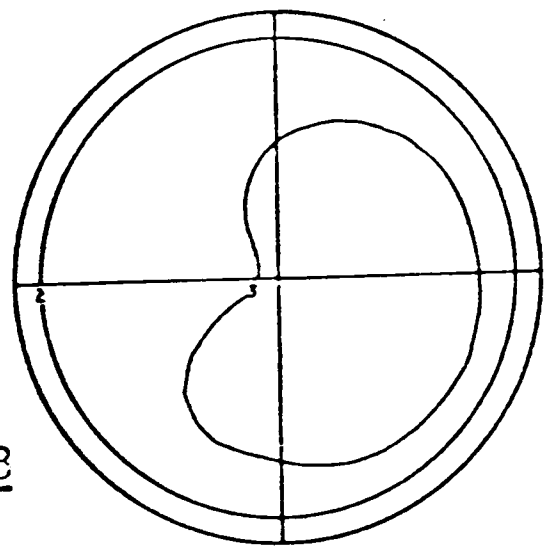












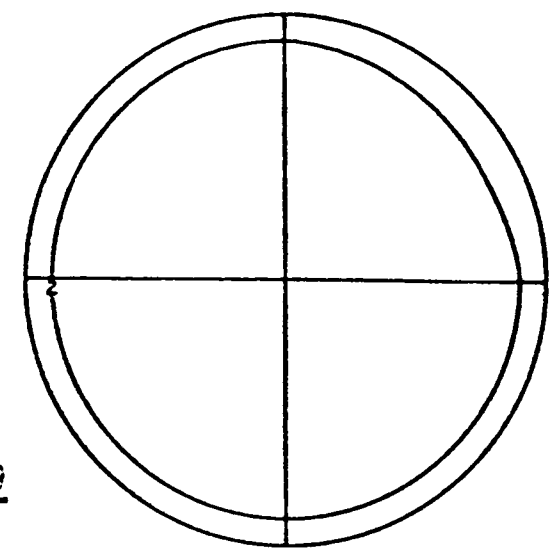


FIGURE 8.4

PULSATILE FLOW VELOCITY PLOTS 15 CM. DOWNSTREAM OF BRANCH 1
LOW FLOW

1L15P

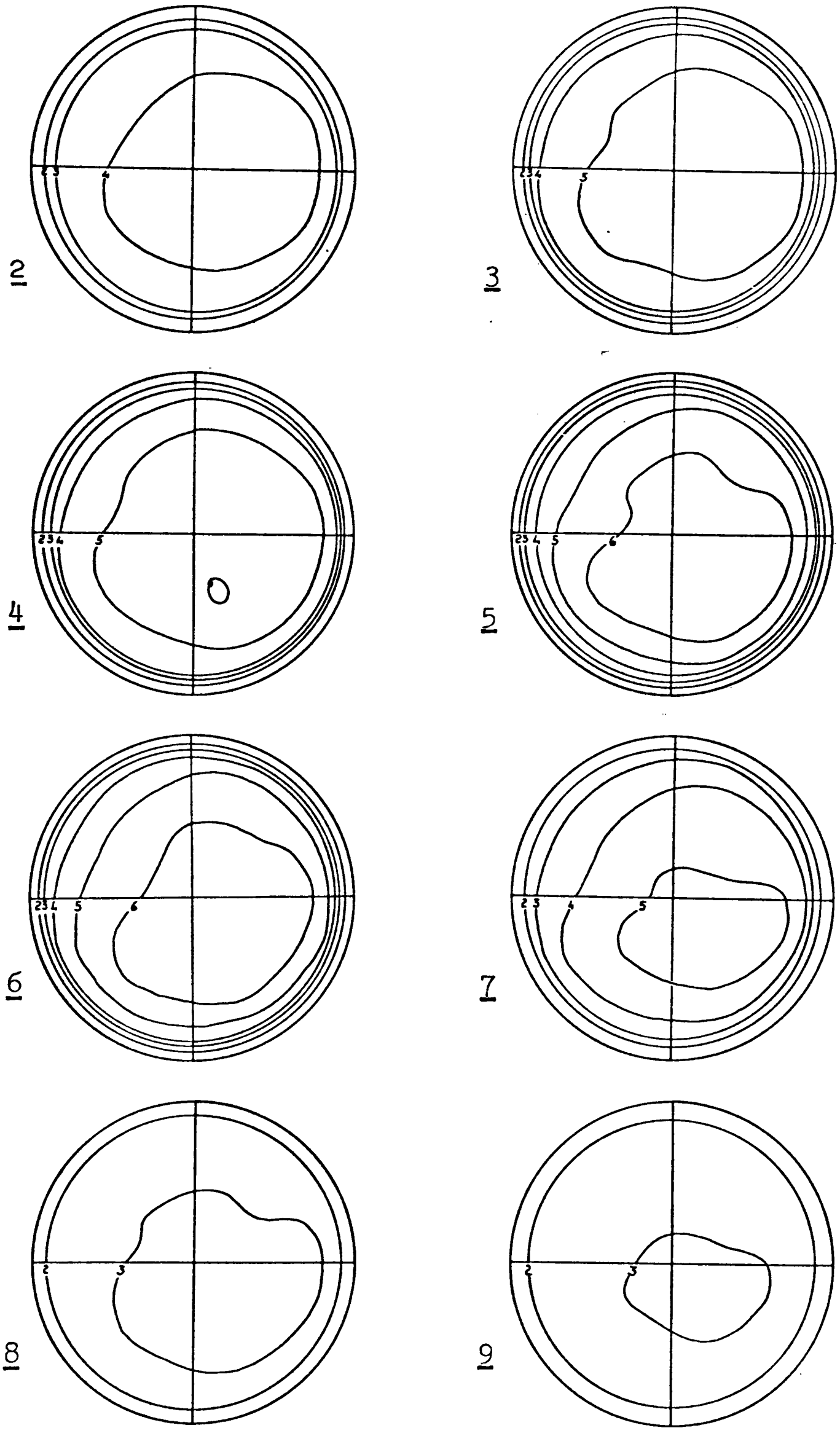


FIGURE 8.5

PULSATILE FLOW VELOCITY PLOTS 3 CM. DOWNSTREAM OF BRANCH 1
HIGH FLOW

1H3P

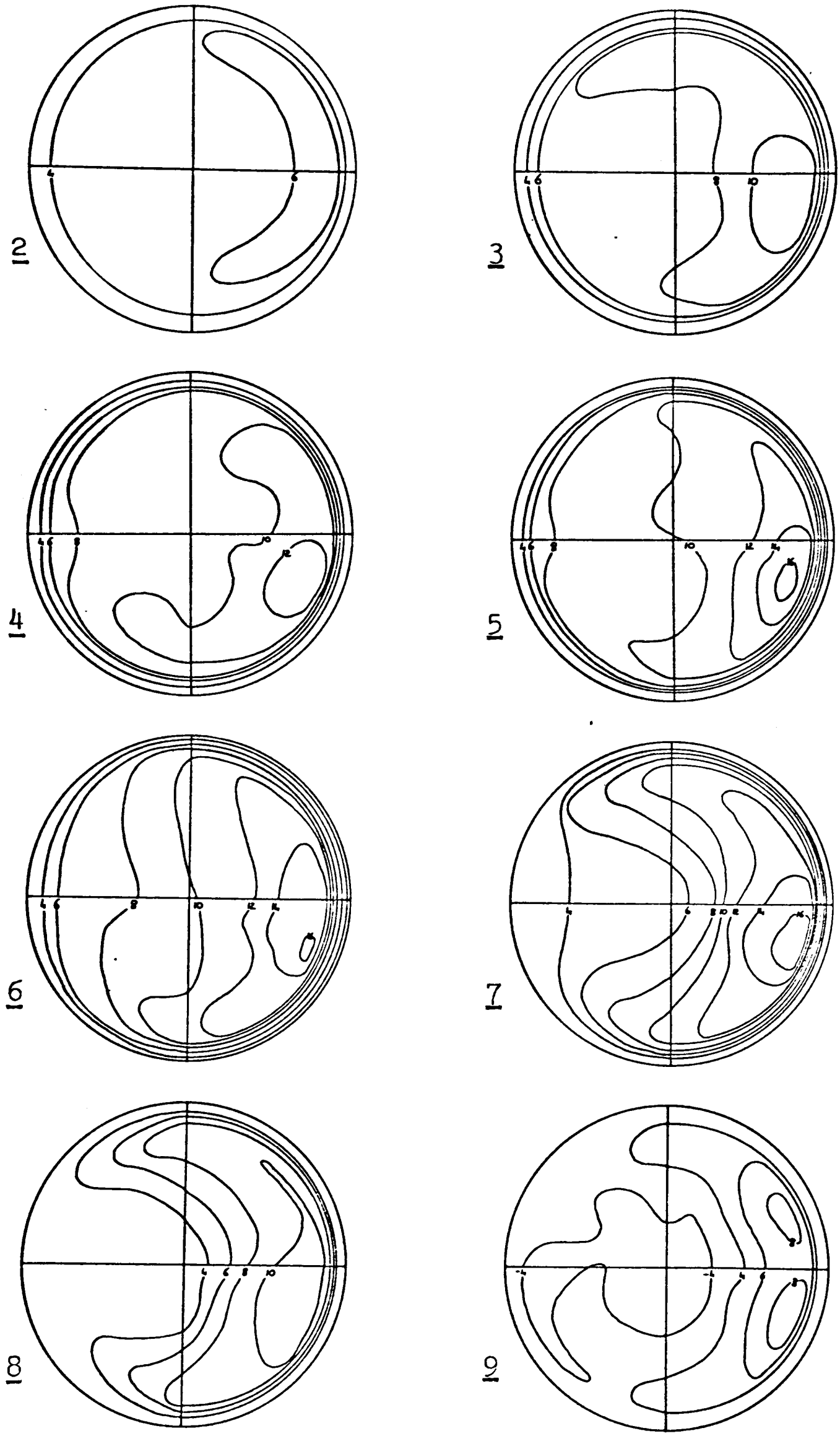


FIGURE 8.6

PULSATILE FLOW VELOCITY PLOTS 7 CM. DOWNSTREAM OF BRANCH 1
HIGH FLOW

1H7P

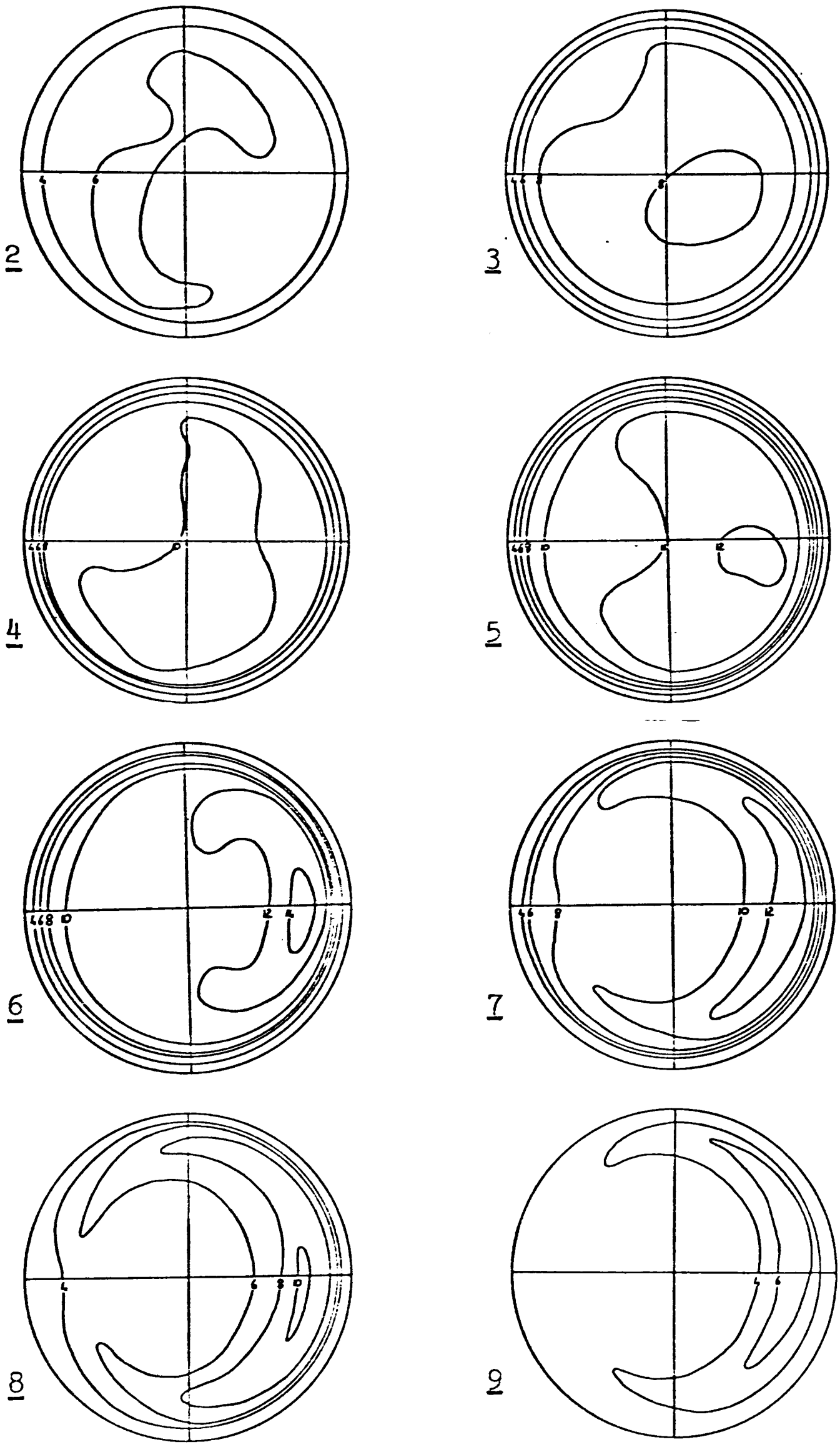
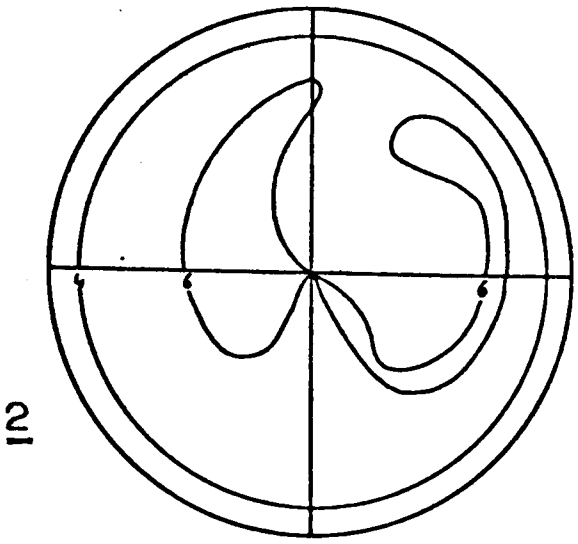


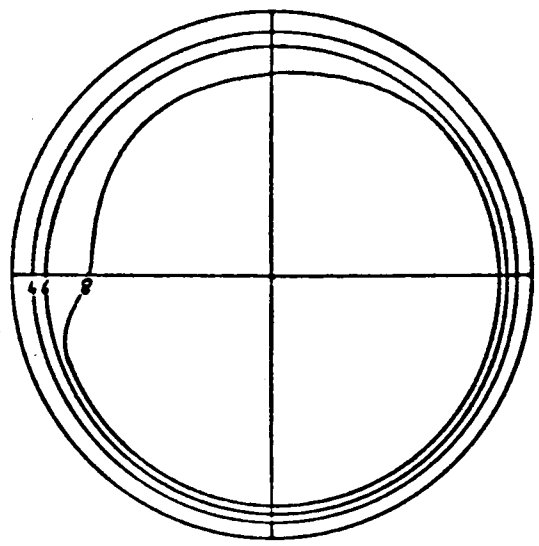
FIGURE 8.7

PULSATILE FLOW VELOCITY PLOTS 11 CM. DOWNSTREAM OF BRANCH 1
HIGH FLOW

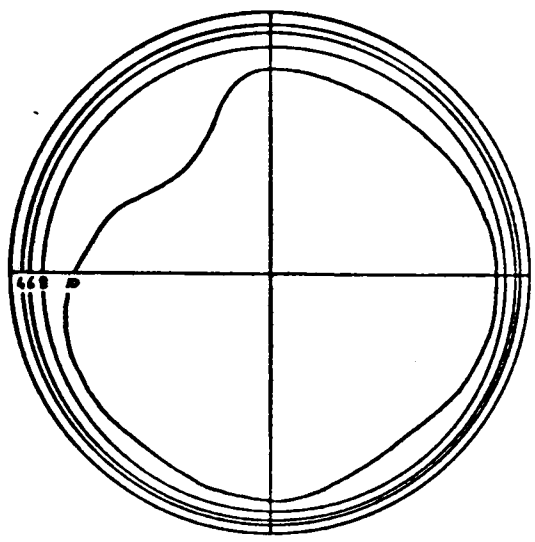
1H11P



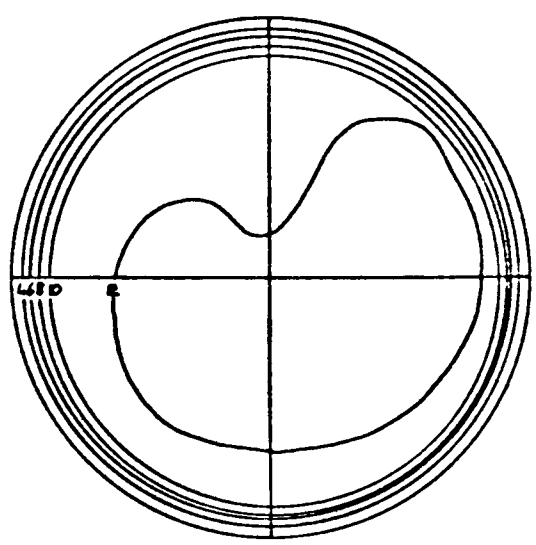
2



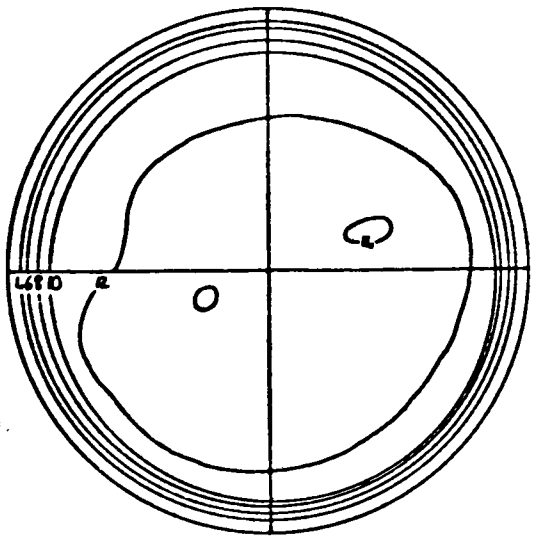
3



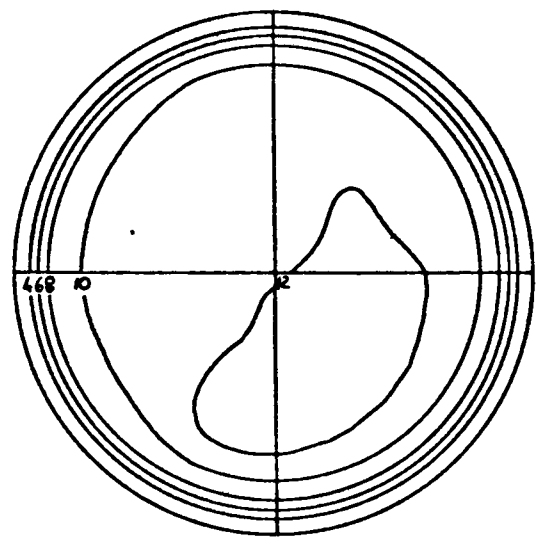
4



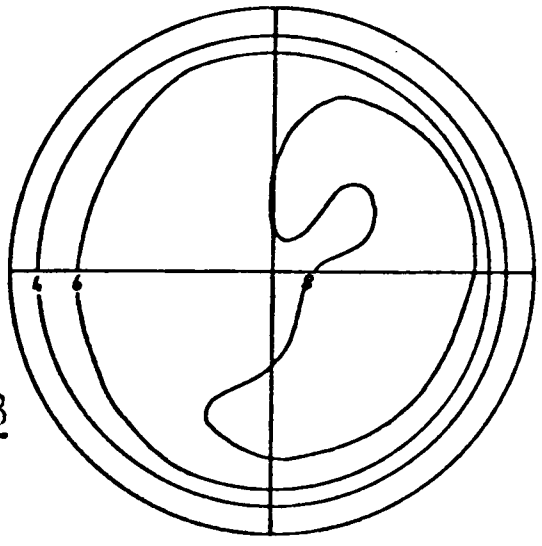
5



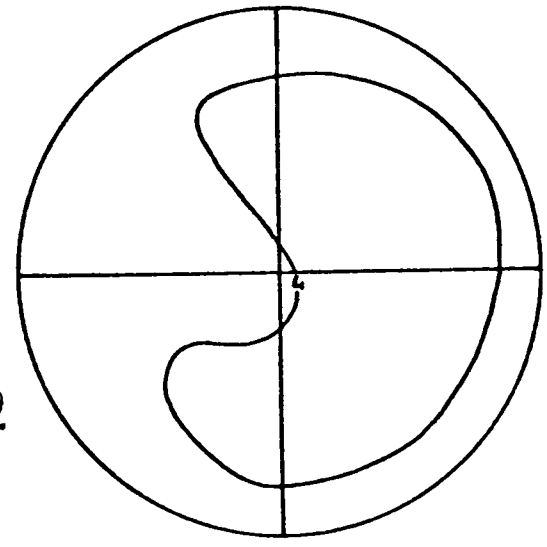
6



7



8



9

FIGURE 8.8

PULSATILE FLOW VELOCITY PLOTS 15 CM. DOWNSTREAM OF BRANCH 1

HIGH FLOW

1H15P

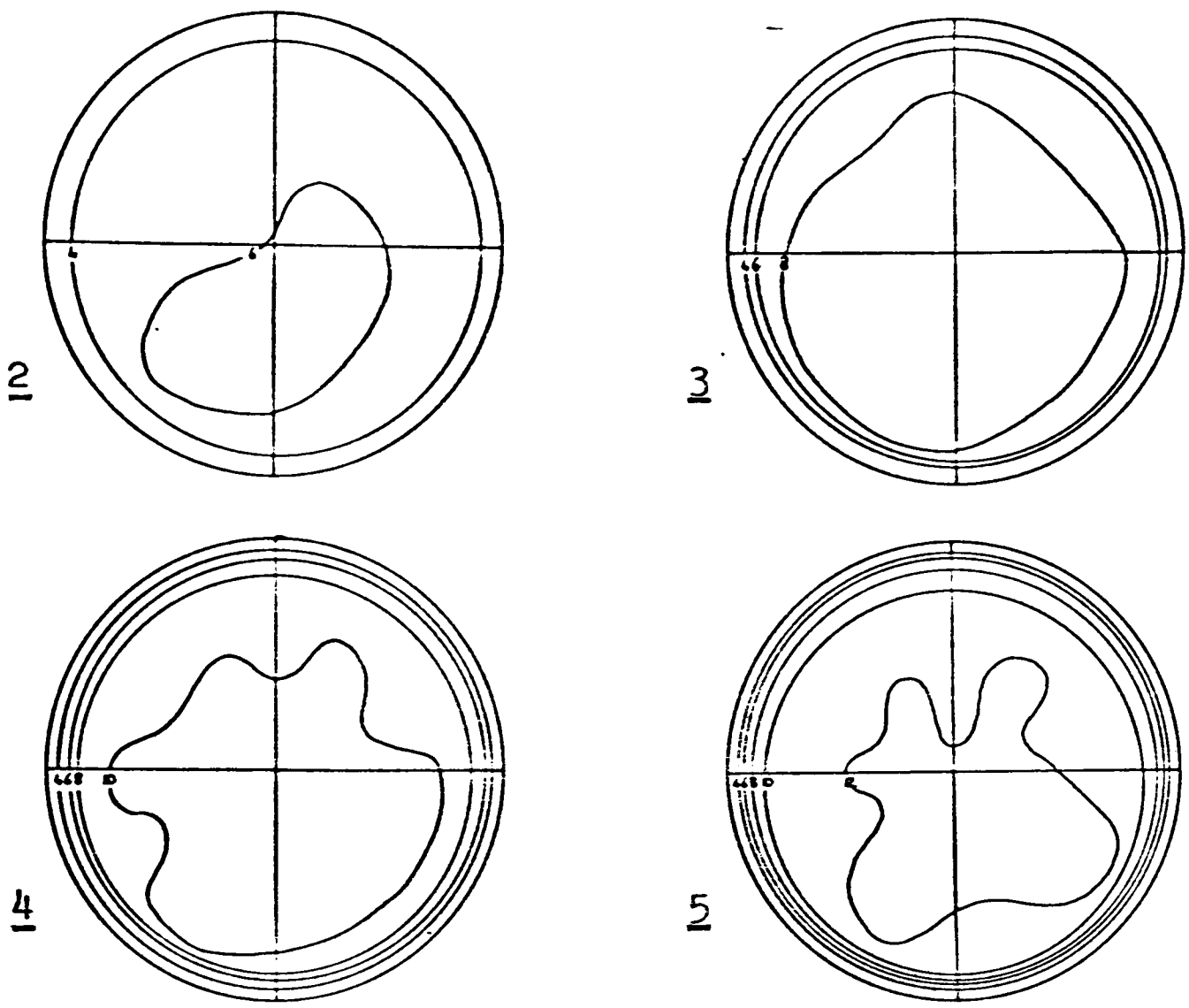


FIGURE 8.9

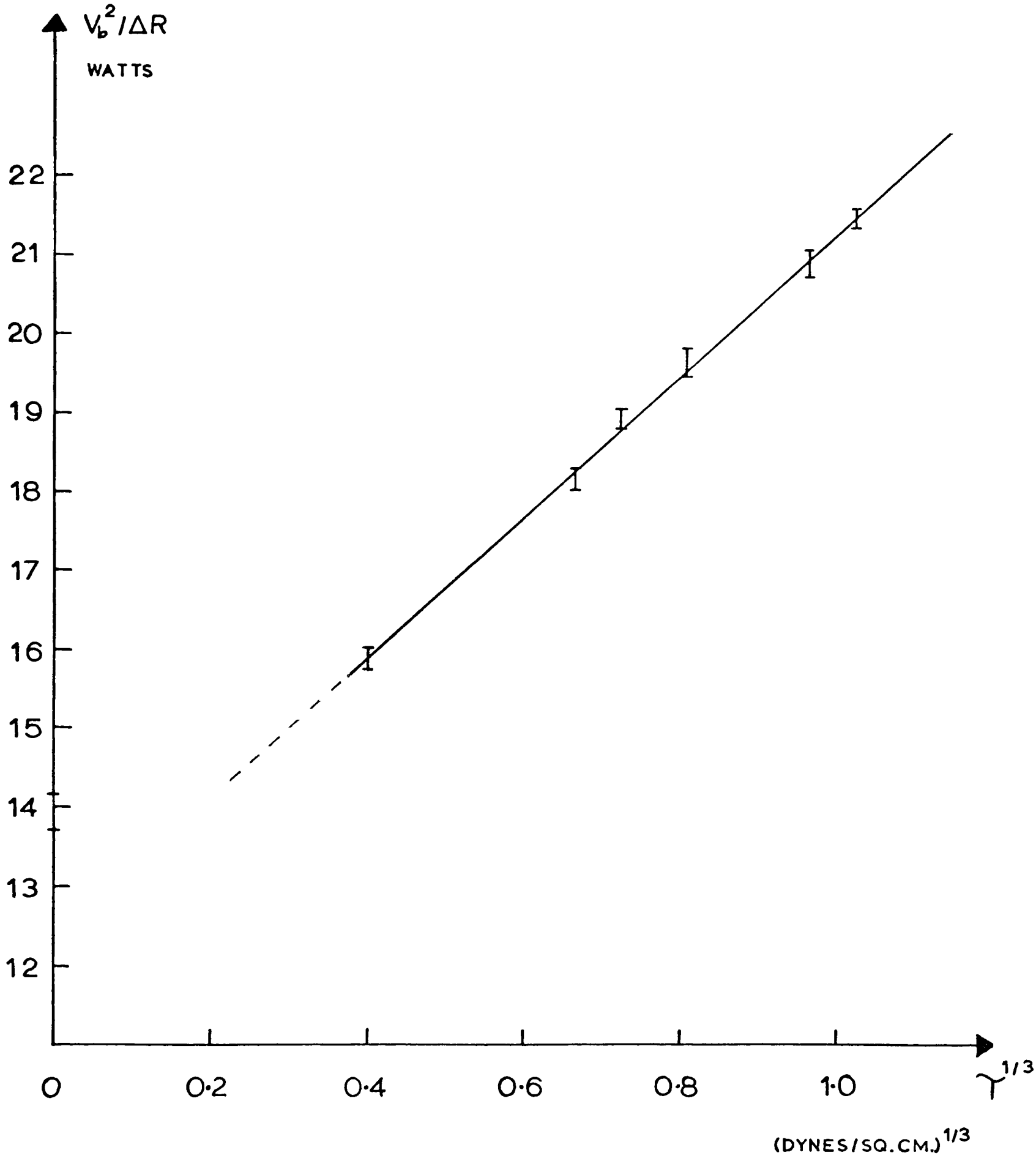


FIGURE 9.1

CALIBRATION CURVE

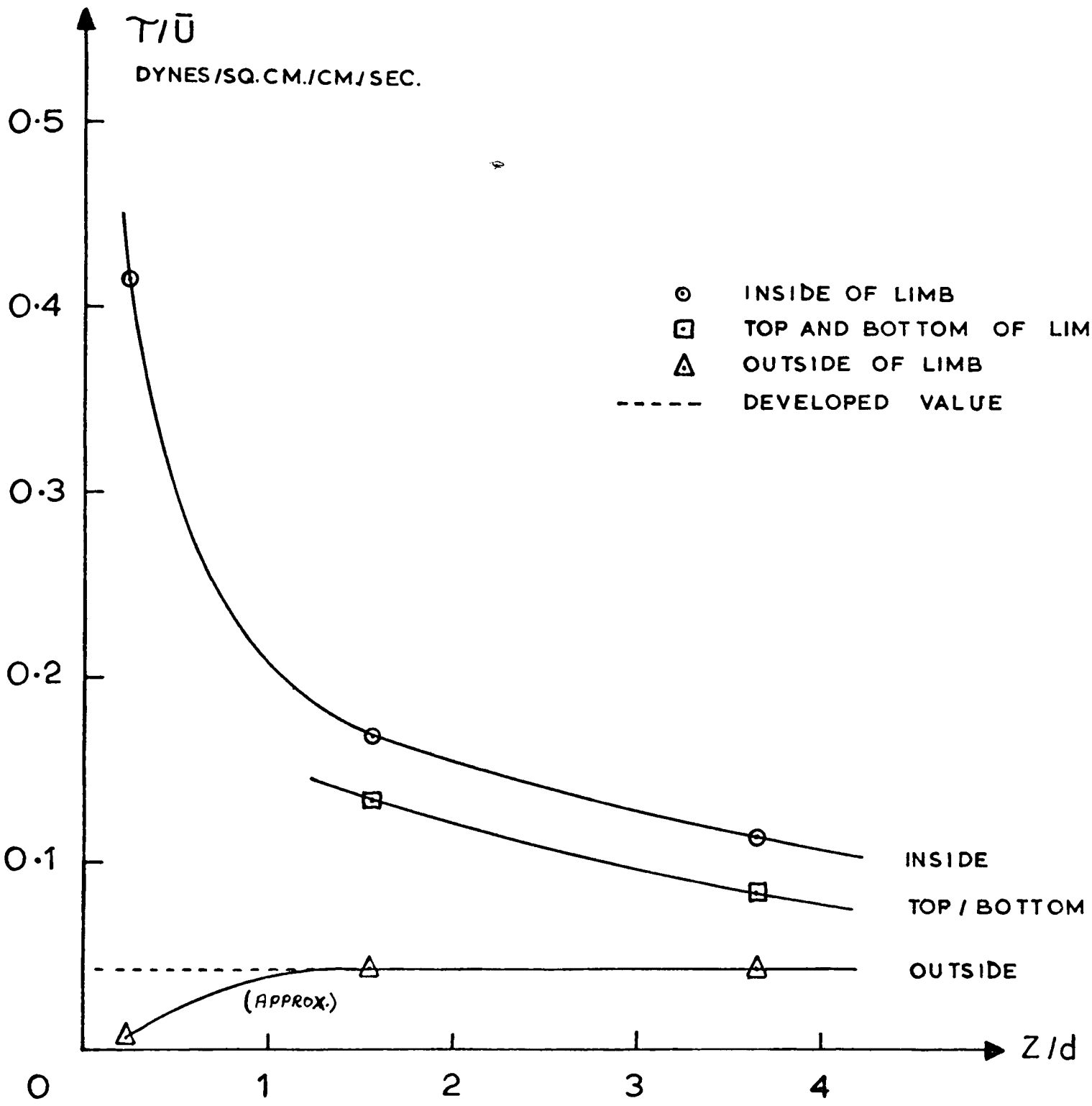


FIGURE 9·2

SHEAR STRESS DISTRIBUTION DOWNSTREAM.

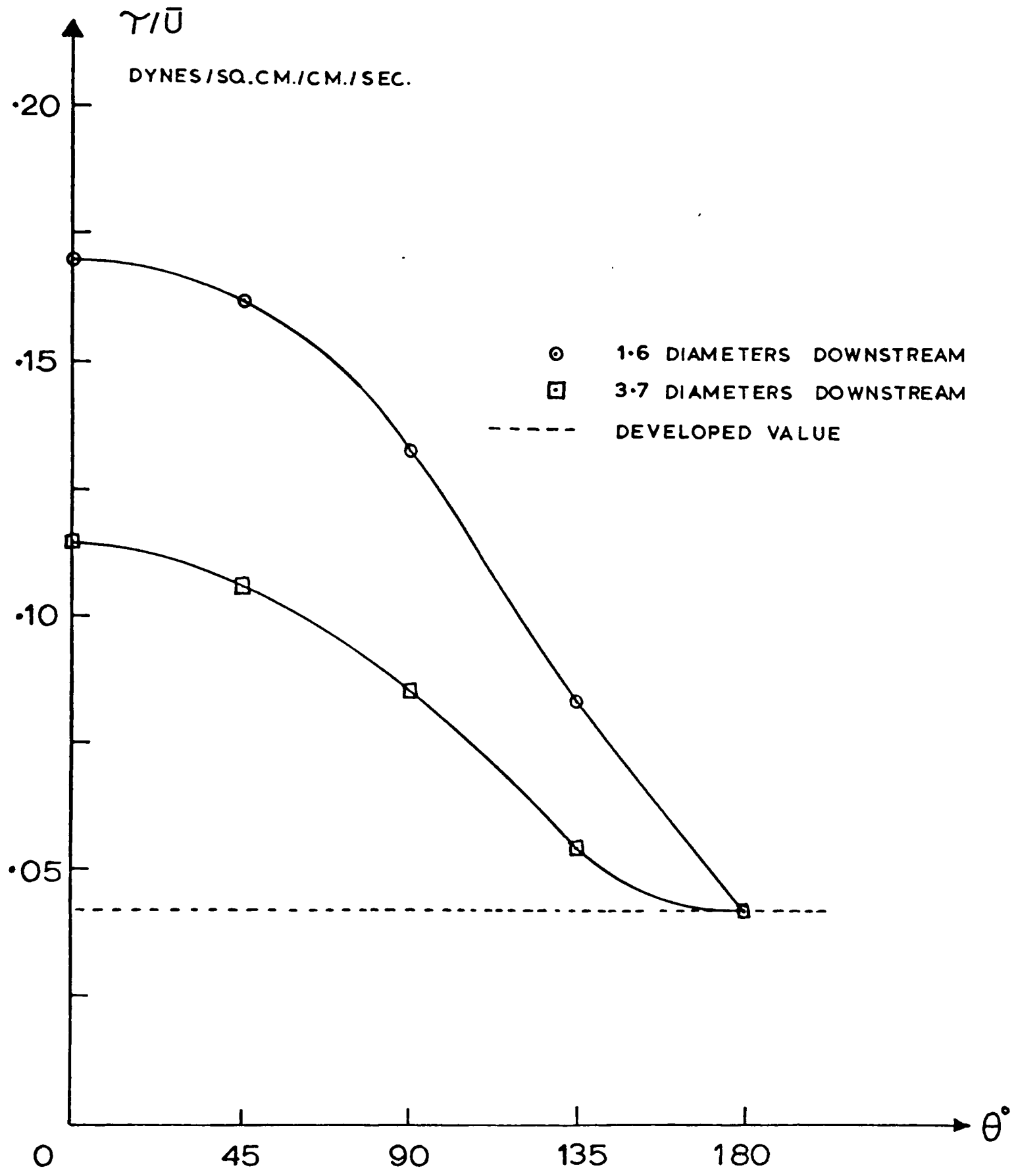


FIGURE 9·3

SHEAR STRESS DISTRIBUTION AROUND TUBE

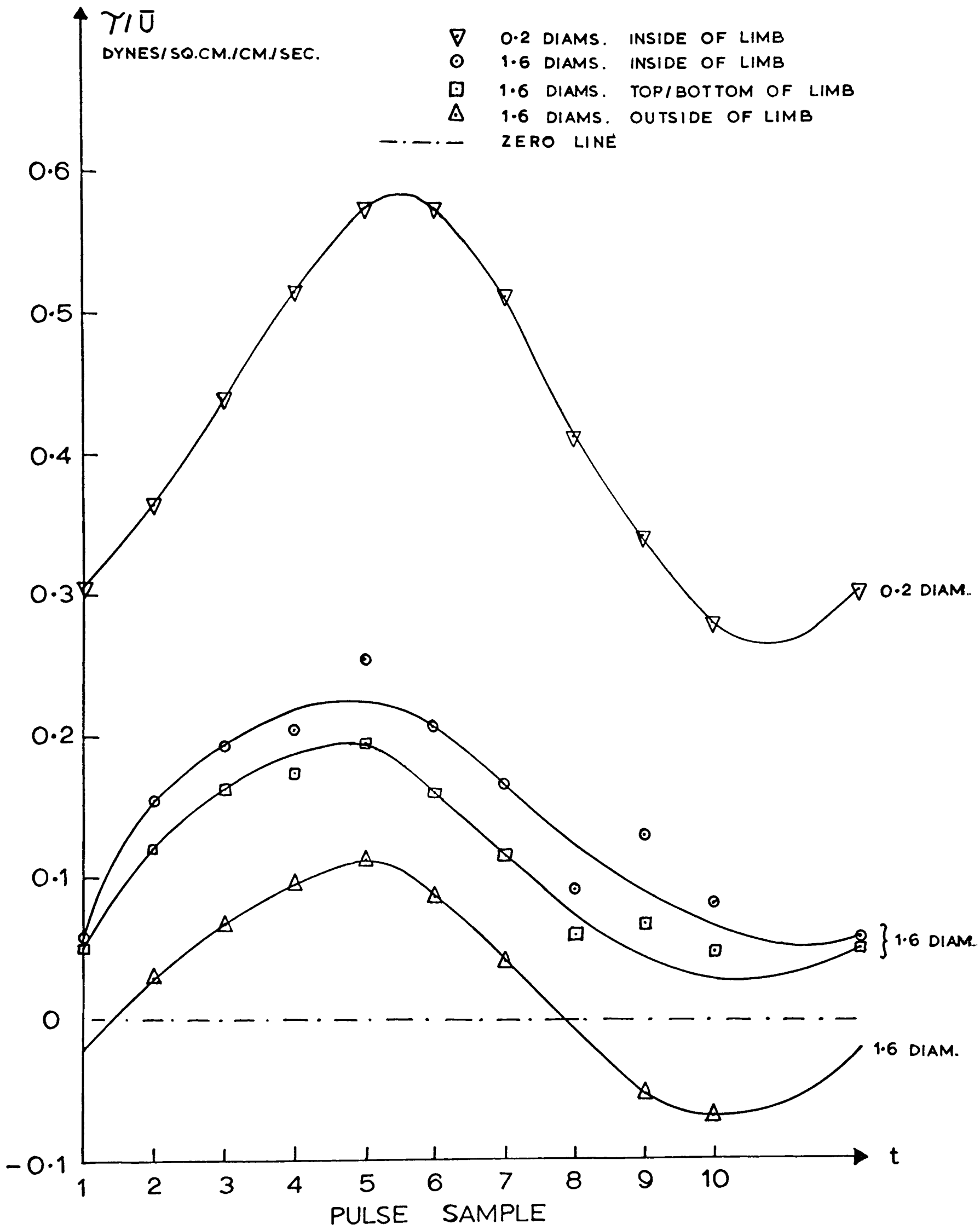


FIGURE 9·5

SHEAR STRESS VARIATION WITH TIME

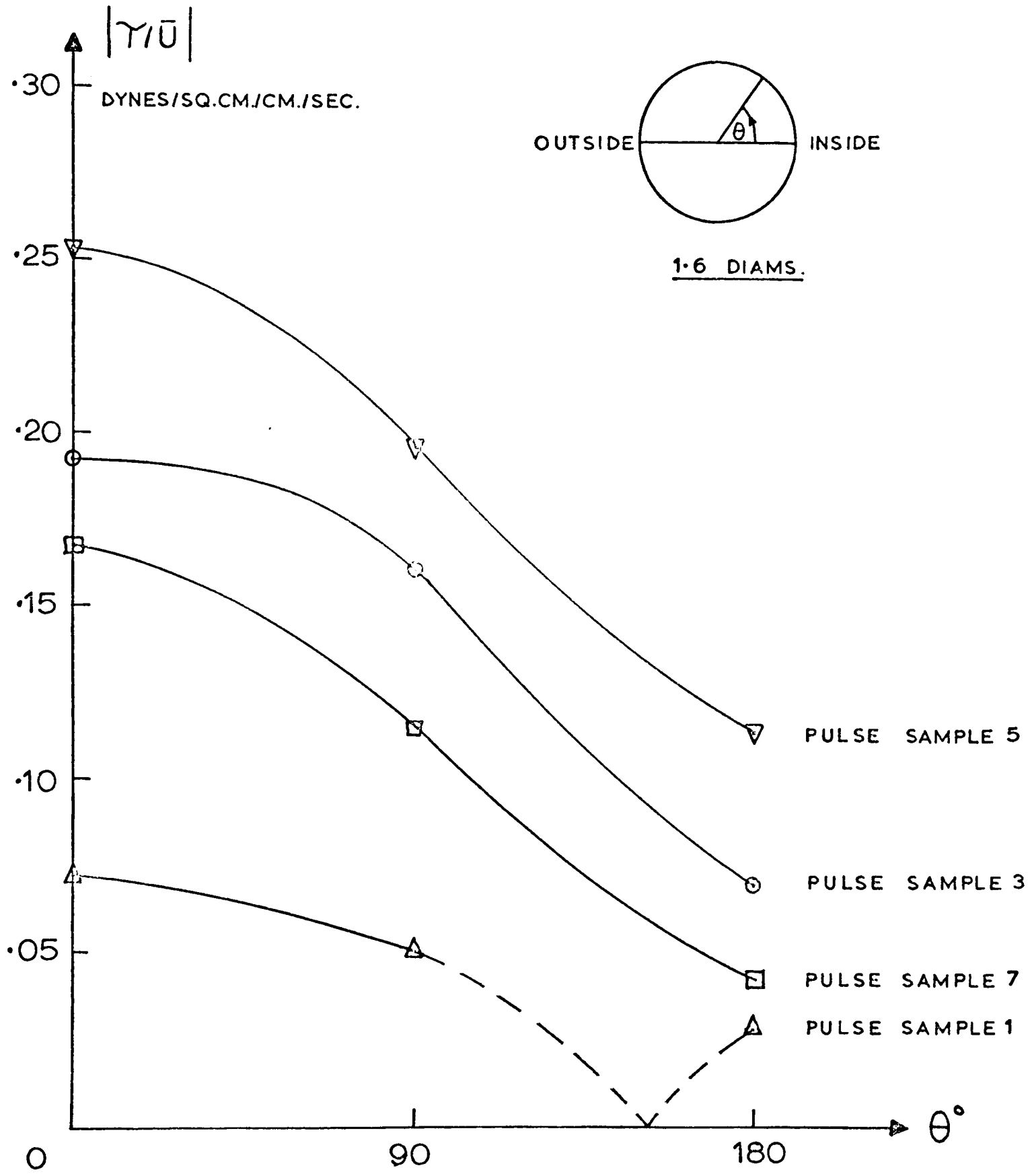


FIGURE 9·6

SHEAR STRESS DISTRIBUTION AROUND TUBE IN PULSATILE FLOW AT 1·6 DIAMETERS DOWNSTREAM

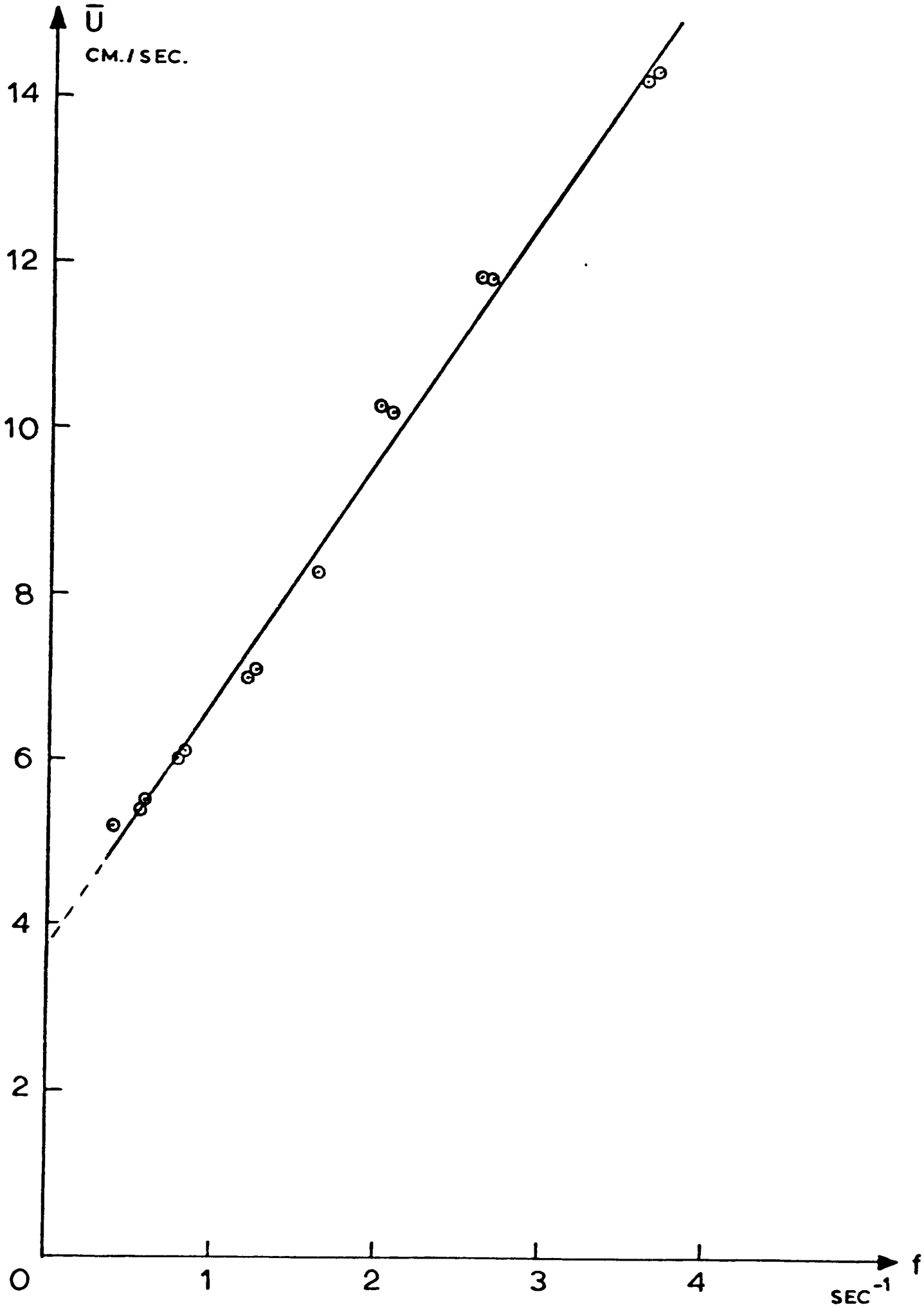


FIGURE 9·7

VORTEX SHEDDING FREQUENCY

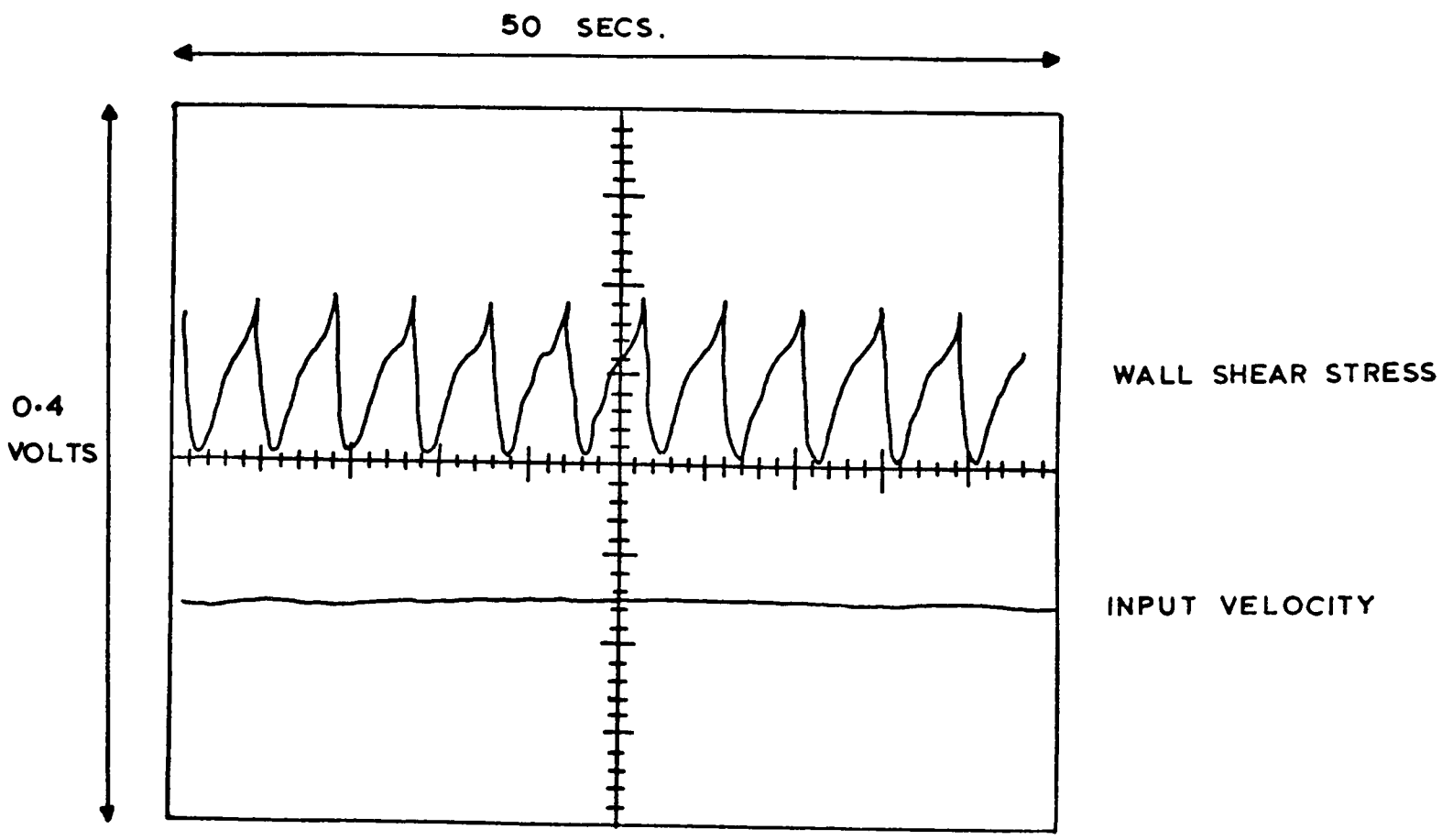


FIGURE 9.8

MEASUREMENTS IN A CONFLUENCE

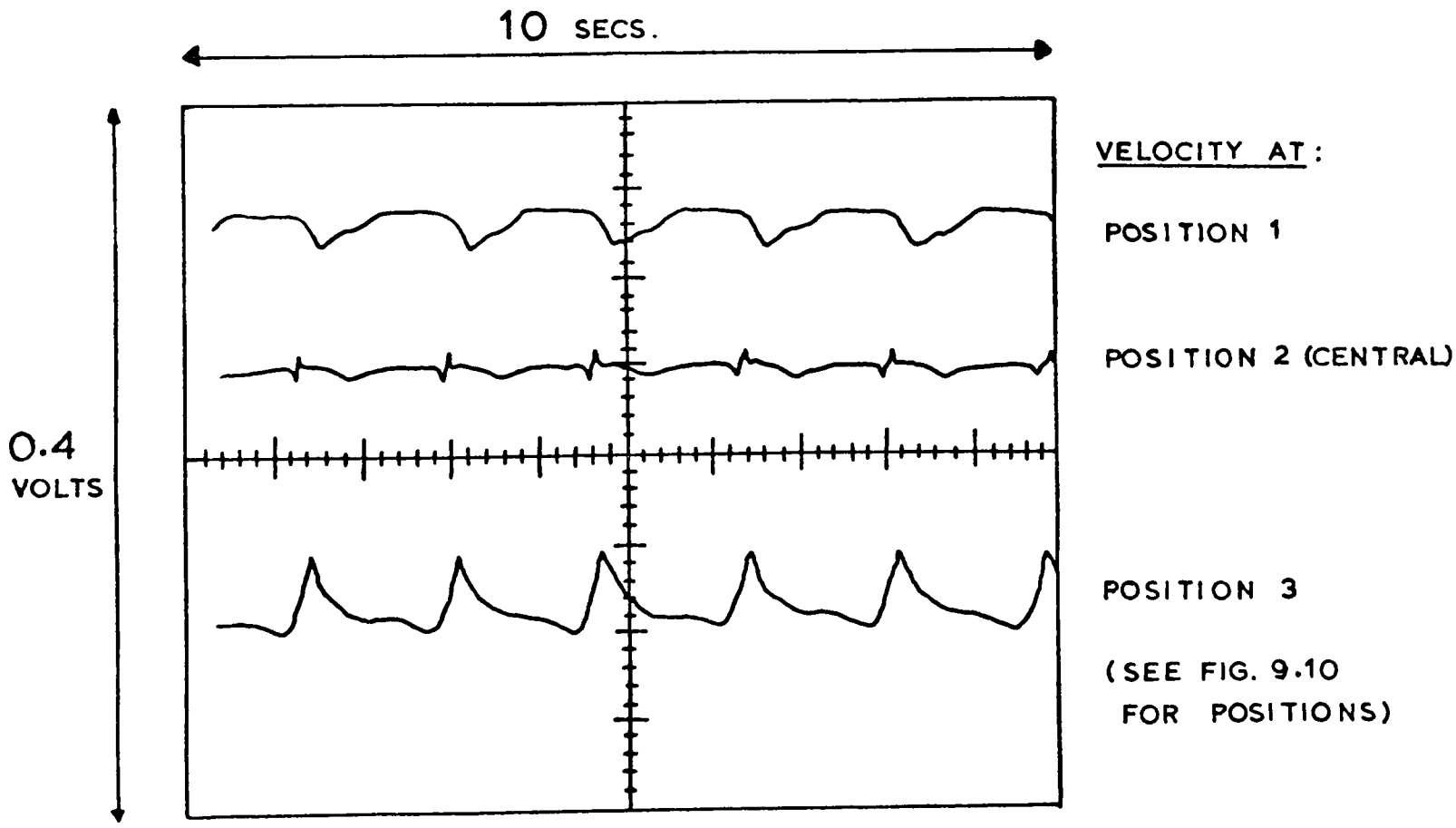


FIGURE 9.9

MEASUREMENTS IN A CONFLUENCE